

The Hebrew University of Jerusalem
Faculty of Mathematics and Natural Sciences
Racah Institute of Physics

**MULTIMODE QUANTUM OPTICS IN
NONLINEAR SUPERCONDUCTING
CIRCUITS**

Thesis for the Degree of "Doctor of Philosophy"

by

Samuel Naftali Goldstein

Submitted to the Senate of The Hebrew University of Jerusalem

September 2021

This work was carried out under the supervision of Prof. Nadav Katz

Acknowledgments

Ben Zoma said: Who is wise? He who learns from every man, as it is said: "From all who taught me have I gained understanding".

Pirkei Avot 4,1

During the course of my Ph.D. at The Hebrew University, I enjoyed the support, council, and help from a large number of people.

First and foremost, I thank my supervisor, Nadav Katz, for his endless patience for my best and worst ideas, for his phone being on even when his door was locked, and most importantly, for always relating to me as a partner in the research, and never simply as his extended hands in the daily work.

I spent around a third of my research in the Nano-Center, mostly in the clean-room on fabrication, where Shimon Eliav, Maurice Saidian, Itsik Shwekey, Galina Chechelinsky, and Rami Gabai were always welcoming and assisted me in any possible way. Also at the characterization unit I enjoyed the support of Avi Ben-Hur, Inna Popov, and Atzmon Vahaki. And it was always a pleasure to visit the machine shop, chatting and consulting with Avner Shatili and Rowe Akerman.

In our lab, my partners in crime were the other students, in particular Naftali Kirsh, Elisha Svetitsky, Guy Pardo, and Yuval Zamir, who worked closely with me and taught me a lot.

In certain projects not described in this thesis (due to the loose or complete lack of connection to its title) I also conferred with Michael Ben-Or (from the computer science department) and Baruch Meirson. I valued their time and help, even though our cooperation did not lead to publications.

At a few occasions, we cooperated with groups outside The Hebrew University. I thank Michael Stern and Tikai Chang from The Bar Ilan University, Serge Rosenblum and Fabien Lamont from The Weizmann Institute, and Jonas Bylander and Amr Osman from Chalmers in Sweden for their hospitality and help. I also appreciated the companionship of Ciprian Padurariu, Bjoern Kubala, and Joachim Ankerhold from the University of Ulm.

But most of all, I dedicate this work to my wife, Orian. Being a Ph.D. student herself (in chemistry), Orian was never merely an emotional supporter. Rather, she would relate to my problems, understand, and sometimes even provide scientific advice when needed. Thank you for helping me believe.

Abstract

One of the most promising candidates as a platform for future quantum computers is superconducting circuitry. The qubits of these circuits are anharmonic oscillators, and their design, control, and operation are possible with well-established protocols for fabrication and measurement.

Superconducting quantum circuits offer more than simply qubit excitation and readout. The far-reaching opportunities of a low-loss wave mechanics system include both fundamental research of optical phenomena such as interference and quantum walks on one hand; and commercial applications, e.g. amplification and sensing devices, on the other.

In this thesis we explore the multimode dynamics of superconducting circuits, first from a theoretical perspective with simulations of a specific proposed system, and then by cryogenic experiments with nano-metric devices tailor-made for this purpose.

Initially, we review the infrastructure of superconducting quantum circuits, the most essential properties of waveguides, couplings, and qubits. Based on these components, we propose and analyze the performance of a superconducting microwave boson sampling device. In such a linear network of capacitively coupled spatial modes, multiple bosons undergo a coherent evolution. The simplest example of a two-particle interference in this framework is the celebrated Hong-Ou-Mandel interference [1]. When scaling to larger numbers of bosons, classically computing the exact distribution of bosons has been shown, under reasonable assumptions, to be exponentially hard [2]. By our simulations, we prove the feasibility of the proposed system considering decoherence effects. We furthermore estimate its sensitivity to perturbations (comparing to coherent input states) and thus introduce the novel concept of quantum sensing by a boson sampling device.

Next, we present the travelling wave parametric amplifier based on a high-kinetic inductance microstrip. Superconducting microwave amplifiers are vital for reliable readout of low-power measurements as are often necessary in quantum experiments. This kind of amplifier is expected to be quiet (low noise temperature), and to have large bandwidths and high dynamic range. While existing implementations partly meet these criteria, they suffer from certain limitations, such as rippled transmission spectra or limited dynamic range, some of which are caused by the lack of proper impedance matching [3–5]. Our device overcomes the central challenges of the existing amplifiers, as it exploits the nonlinear kinetic inductance of tungsten-silicide (WSi) for wave-mixing of the signal and a pump. In this process, known as degenerate four-wave mixing, also an idler tone arises, bearing witness to the multimode dynamics. We present the coupled-mode equa-

tions governing the wave propagation in our amplifier, creating the theoretical framework. By careful design of the geometry, we engineer the impedance to 50Ω , while decreasing the phase velocity in our transmission line. This step is found by simulations to benefit the amplification and to allow reduction of the amplifier's length by approximately an order of magnitude.

Despite the many advantages, our amplifier does suffer from dielectric losses, which we characterize and include in our simulations by the two-level-system defect model [6], but these effects are limited due to the short length and a judicious choice of amorphous Silicon as our dielectric. Pumping on our device amplifies the signal by 15 dB over a 2 GHz bandwidth.

We then introduce compact itinerant microwave photonics in superconducting circuits as an extension of the travelling wave parametric amplifier. In this project we take advantage of the microstrips two central properties: The nonlinearity of the kinetic inductance of tungsten-silicide, and the slow phase velocity, approximately two orders of magnitude lower than the common value in prevailing superconducting aluminum waveguides. These two extraordinary features pave the way for the implementation of microwave photonics.

In general, photonics is a remarkably powerful system for quantum simulation and technologies [7, 8], but its integration in superconducting circuits has so far been constrained by the long wavelengths and impedance mismatches in these circuits. Attempts to solve this problem include e.g. compressed footprints by deforming the traces to spirals or meanders [9, 10]. With our microstrips, we introduce a solution to these difficulties via compact networks of impedance-matched waveguides and inductive coupling wires. Broadband capabilities are also demonstrated for superconducting microwave photonics in terms of routing, emulation and generalized linear and nonlinear networks.

Our devices are fabricated in a cleanroom facility using state-of-the-art techniques for deposition, patterning, and etching of multiple aligned thin films of various materials chosen for their electrical properties. Cryogenic measurements are conducted in a dilution refrigerator at 20 mK, and signals are transmitted through cascades of carefully chosen attenuators, circulators, and amplifiers to ensure correct power generation at the entrance of the devices, and optimal readout back at room temperature with network and signal analyzers.

To enhance the mounting and wiring of our devices, we also develop a simple recipe for packaging, including printed circuit boards and designated boxes. This recipe, including only in-house fabrication (with equipment available at most universities), enables fast re-modelling of the packaging infrastructure, when new variants of devices are incompatible with old boxes.

As a whole, we expand the toolbox of superconducting circuits, enabling the realization of linear and nonlinear optics in compact devices, preparing the ground

for both additional research and technological applications.

Letter of Contribution

Experimental results presented in this thesis were conducted with devices which I in general planned, designed, and fabricated myself. I wrote all CAD-scripts for layout of devices produced in the clean room, which I processed myself, except for one wafer made by Amr Osman at Chalmers according to my instructions. I also prepared all sketches for machine shop components included in our research (manufactured by Rowe Akerman and Avner Shatili). Codes for simulating the behaviour of the physical devices, prior to fabrication and measurement, were authored by me, with the exception of those in Sec. 5.3, where Guy Pardo assisted me. Post-experimental analysis and numerical comparison between theory and empirical data was also done by me..

In the numerical analysis of boson sampling, Simcha Korenblit and Ydan Bendor wrote parts of the simulation, and Michael Geller and Hao You provided theoretical insights in this project. I continued the work of Simchah, corrected results and figures, and came to different conclusions than him, which were eventually published.

Ori Hachmo and Yotam Federman did some pioneering work in tungsten-silicide processing (e.g. how to deposite and pattern). Also Yuval Zamir contributed to this project with simulations.

Elisha Svetitsky developed certain clean-room recipes, and Naftali Kirsh assisted the cryogenic measurements. Shimon Eliav suggested the process for evaporation of amorphous silicon.

Some of the theoretical framework presented in Appendix C was prepared by Ciprian Padurariu, Bjoern Kubala, and Niklas Glaesner (University of Ulm).

Publications

Goldstein, S., Korenblit, S., Bendor, Y., You, H., Geller, M.R., and Katz, N.: Decoherence and interferometric sensitivity of boson sampling in superconducting resonator networks. *Physical Review B*, 95(2), 2017.

Goldstein, S., Kirsh, N., Svetitsky, E., Zamir, Y., Hachmo, O., de Oliveira, C.E.M., and Katz, N.: Four wave-mixing in a microstrip kinetic inductance travelling wave parametric amplifier. *Applied Physics Letters*, 116(15), 2020.

Goldstein, S., Pardo, G., Kirsh, N., Gaiser, N., Padurariu, C., Kubala, B., Ankerhold, J., and Katz, N.: Compact Itinerant Microwave Photonics with Superconducting High-Kinetic Inductance Microstrips. Accepted for publication in *New Journal of Physics*, 2021.

Kirsh, N., Svetitsky, E., **Goldstein, S.**, Pardo, G., Hachmo, O., and Katz, N.: Linear and nonlinear properties of a compact high-kinetic-inductance WSi multimode resonator. *Physical Review Applied* 16(4), 2021.

Patent

While the paper on four wave-mixing in the kinetic inductance amplifier was in review, the student and author of this thesis wrote a provisional patent with the supervisor on the microstrip amplifier in cooperation with *Yissum*:

Goldstein, S., Katz, N., et al.: MIKITA - US Provisional Patent Application - Reference no. 63/112,230

Contents

1	Introduction	1
1.1	Superconducting Supremacy in Quantum Information	2
1.2	Motivation	4
1.3	Thesis Composition	5
2	From Microwave Engineering to Quantum Optics	6
2.1	Classical Electrodynamics	7
2.2	Quantizing the LC-resonator	11
2.3	Superconducting Qubits	12
2.4	Quantum Electrodynamics	19
2.5	Boson Sampling	24
3	Kinetic Inductance & Parametric Amplification	29
3.1	Kinetic Inductance	30
3.2	Tungsten-Silicide Micro-strips	31
3.3	Wave-Mixing and Amplification	35
4	Methodology	38
4.1	Simulation Techniques	39
4.2	Nano-fabrication	44
4.3	Microwave Packaging Environment	49
4.4	The Dilution Refrigerator	51
4.5	Wiring	52
4.6	Electronics	53
5	Results	55
5.1	Analyzing the Superconducting Boson Sampler	56
5.2	The Kinetic Inductance Travelling Wave Amplifier	61
5.3	Networks of Microstrip Waveguides	67
6	Discussion and Outlook	75
6.1	Discussion of Results	76

6.2 On-going Experiments	81
6.3 Thesis Summary	85
6.4 Closing Remarks	86
Bibliography	88
Appendices	93
A. Mathematical Derivations	93
B. Fabrication	97
C. Theory of the Two Coupled Travelling Waveguides	100
D. Hong-Ou-Mandel & The Birthday Paradox	104

CHAPTER 1

Introduction

The beginning of the 21st century is an exciting era to study experimental quantum physics. Ties between academia and high-tech companies are stronger than ever. Research labs continuously expand (and publish) their understanding of experimental systems and methods to control them, and new quantum technologies and related products are frequently commercialised. Some of the world's leading enterprises even join the universities in quantum research e.g. in establishing quantum computers with superconducting (SC) qubits.

This introduction gives a very short, general account of the research climate in the field of quantum computation at the time of writing. SC qubits are briefly described, followed by a motivation for this thesis and an overview of its composition.

1.1 Superconducting Supremacy in Quantum Information

Over the course of 40 years since Richard Feynman suggested to employ quantum computers to simulate physics [11], the field has developed from the question of simple simulation to include a variety of applications such as cryptography [12], synchronization [13], and quantum sensing [14, 15]. Amongst several other sub-fields of quantum technologies, the universal quantum computer stands out as a tool superior to the strongest classical computers¹ for particular problems of interest [18].

Quantum computation requires quantum bits (qubits) and quantum gates, just as classical computers are based on classical logic gates and classical bits. In principle, these bits could be multi-level-systems (and the gates would need some generalization), but for simplicity it is convenient to limit the number of states of the system.

In the quest to realize quantum computers, we are faced with the challenge of finding reliable qubits, and as will be described further in Section 2.4.4, this is not a property granted to every quantum system. In fact, though quantum mechanics governs our physical world, humanity is accustomed to classical physics, because the many degrees of freedom of open quantum systems destroy the quantum behaviour rather quickly (many orders of magnitudes below human experience). Thus, reliability relies largely on isolating the qubit, a property not easily provided, when candidates for qubits must also be controllable - for the operation of gates².

An additional feature of qubits, necessary for quantum computation, is the ability to perform fast readout of their state. We will return to this point later.

1.1.1 Qubit Candidates

Qubits can in principle be any two-level-system, TLS, demonstrating quantum-mechanical behaviour, e.g. superposition of states, entanglement with other qubits etc. But some candidates stand out due to certain advantages.

TRAPPED IONS An atom can be applied as a qubit, relating to its electronic orbital levels as the states of the qubit, by virtue of the anharmonicity of these levels [20]. Such systems enjoy long life times, but suffer certain limitations, such as their small size making the operation difficult. When ionized, gaseous atoms can be controlled by high-power lasers, but this must be done in ultra-high vacuum to avoid scattering with the air, and the coupling to trapped ions is challenging [21].

¹Despite the success of Google's Sycamore-chip [16], apparently proving this statement, some dispute still exists [17].

²An important topic, lying outside the scope of the thesis, is the research in quantum error correction attempting to extend the time during which the qubits are available for logic operations [19].

NITROGEN-VACANCY CENTERS When a carbon-atom in a diamond is replaced with a nitrogen-atom and a nearby site is depleted of its C-atom, the N-atoms valence electrons' spin functions as a TLS. NV-centers can be operated at room temperatures, but an outstanding disadvantage is the limited couplings available. The NV-center couples to the surrounding C-atoms, i.e. in a network determined by nature.

SUPERCONDUCTING QUBITS In the next chapter we will study SC qubits, which are essentially anharmonic *LC*-resonators. The anharmonicity's source is the nonlinear inductance (L) of the Josephson Junctions. The multiple benefits of this platform include the controllable design and operation, long life times, and the capability of isolating the systems. The most essential disadvantage of SC qubits that does not seem to be solved in the near future, is the cryogenic temperatures necessary for operation, not easily maintainable in labs that are not specialized for the operation and equipped with dilution refrigerators and surrounding electronics.

1.1.2 Employed Superconducting Qubits

For close to two decades, the physics of SC qubits has been scrutinized, and new versions have been developed, enabling enhanced control, tunability, limited noise, and longer coherence times³.

Full-scale universal quantum computers are still not available, but SC qubits are already in use or the subject of intensive research in various frameworks by commercial enterprises such as Google, IBM, etc., and as of this writing, any user can run simple algorithms online free-of-charge with a few SC qubits.

This situation also answers the rhetorical question of the temperature challenge: SC quantum computers will not need installation in personal homes or even at research institutions, where scientists wish to perform hard computational tasks; at the international (or at least national) level, the SC qubits can be concentrated at a common institute and allow remote operation.

1.1.3 The Environment of Superconducting Qubits

In addition to the qubit's value as a quantum bit, a unit for quantum information storage and manipulation, it also serves for single-photon generation [22]. And the operation and control of SC qubits (e.g. excitation and measurement) also require supporting structures and equipment, either incorporated on the SC chip (i.e. other SC devices, like readout resonators or flux bias lines) or at the macroscopic level (i.e. electronic equipment or packaging for the physical mounting in the refrigerator). In short, the strength of the SC qubits is only expressed when considered together with a number of other assets.

³Special attention will be given to this important property throughout this thesis.

1.2 Motivation

This thesis investigates multimode dynamics in SC circuits. The larger the Hilbert space we can produce, the more information a system can carry, and managing networks of multiple modes are thus of importance for future quantum information processing, both at the research level and for commercial applications.

Multimode theory is an integrated part of the study of quantum optics [23–25]. In this work, we address certain experimental aspects of the field from various angles. First, we adopt the so-called Boson Sampling paradigm, explain its claim concerning quantum computation and consider its limitations. This part, based on the simulations in Ref. [26] was published in 2017. In light of the experimental implementation in Ref. [16] (by Google’s team of quantum engineers), certain conclusions in that Letter, in particular in terms of the network size, are outdated, but others, in particular on the interferometric sensitivity of Fock states, remain relevant for future quantum technologies and their development.

Implementing theoretical work is not only a question of the SC circuitry itself, but also the experimental setup. Proper microwave engineering is the key to successful transmission measurements, but in academic research labs the specific requirements (e.g. in terms of geometry, number of connectors, etc.) often change per individual experiment. Therefore, we engage in developing quick, easy methods to produce and change the packaging of the SC circuits, and a separate chapter is dedicated to the macroscopic surroundings of the SC devices together with some general perspectives on the fabrication of SC circuits⁴.

In this context, it will be clear that in order to measure the minuscule energies in SC circuits and conserve the systems’ state, reliable microwave amplifiers are required. Such amplifiers must have a high dynamic range, wide bandwidth (covering the frequencies of the experiment), and low noise. This trio of properties is not always present for commercially available microwave amplifiers, making it subject to research and development [27–29]. For this reason, we develop an amplifier based on a high-kinetic inductance (HKI) SC microstrip transmission line, a less common structure than the coplanar architecture in SC circuits.

One of the benefits of merging HKI materials with microstrip SC transmission lines is that the phase velocity reduces significantly, allowing phase accumulation and routing between coupled wave-guides over relatively short distances compared to coplanar wave-guides. This is also possible in optical wave-guides, but such systems lack the convenient single-photon generation easily achieved with SC circuits [30]. On these grounds we explore the capabilities of the HKI microstrips as a platform for quantum simulation.

⁴Technical recipes with details of materials and processes appear in the appendices.

1.3 Thesis Composition

This is a monograph thesis and not a collection of articles. However, its content is mainly based on the three first publications as listed in the preface, appearing on page vii, namely the three projects: 1) The numerical analysis of boson sampling with SC qubits, 2) the invention of a microstrip HKI amplifier, and 3) compact microwave photonics with HKI microstrip. The chapters of the thesis relate to these topics as follows:

In Chap. 2 we begin with the basic theoretical and practical concepts of SC circuitry to support the discussions throughout the later chapters. This chapter introduces quantum optics, emphasizing its implementation in SC circuits and the paradigm of boson sampling.

Chap. 3 reviews the remarkable topic of kinetic inductance, the microstrip geometry, and explains how wave-mixing is achieved, when merging the former two in SC circuits.

Chap. 4 covers the methodology of the research, from the theory and design of devices to the experimental setup. Initially, it roughly goes through the simulations employed in the research (*results* from simulations are kept for the next chapter). Then, this chapter proceeds by describing the fabrication of devices and the novel packaging environment we developed for mounting to the dilution refrigerator, finishing with some general notes of the measurement setup.

The thesis' most important part, Chap. 5, presents results from numerical simulations as well as experimental data achieved at room temperatures and in cryogenic measurements with the dilution refrigerator.

Finally, Chap. 6 discusses the results and summarizes additional projects, to which the student contributed significantly and work that, at the writing of this thesis, is still not mature for publication. This chapter concludes the thesis with perspectives for future work in the field.

CHAPTER 2

Background I: From Microwave Engineering to Quantum Optics

As already stated in the introduction, superconductivity has taken a leading role amongst the various platforms for quantum information [31]. Even without qubits, superconductivity is an exciting *macroscopic* quantum phenomenon itself whose theoretical roots go deep into solid state physics.

In this chapter, we review central aspects of classical electrodynamics, SC circuitry, and then move on to SC qubits and quantum electrodynamics. And finally, we introduce the boson sampling paradigm.

The modest description of the topics appearing in this chapter is mostly limited to whatever is relevant and necessary for further use throughout the thesis. We thus avoid deeper analyses of e.g. the different SC qubits, the complicated nature of SQUIDs, and the world of quantum information. More information is available in Refs. [32–34]. Where no other references are cited, the derivations follow those three.

2.1 Classical Electrodynamics

Before entering the quantum regime of single-photon states, we review a few aspects of classical electrodynamics. Superconductivity is indeed a quantum phenomenon, but in its operation, we do apply classical elements.

2.1.1 Elements of Transmission Line Theory

Based on the Kirchoff laws, we can describe the propagation of current I and voltage V in transmission lines with the Telegrapher's equations. The most important parameters are the inductance L_l and capacitance C_l per unit length, and in addition to these: the resistance R and conductance G , which may be frequency dependent. The equations

$$\frac{\partial V(x, t)}{\partial x} = -L_l \frac{\partial I(x, t)}{\partial t} - RI(x, t) \quad (2.1a)$$

$$\frac{\partial I(x, t)}{\partial x} = -C_l \frac{\partial V(x, t)}{\partial t} - GV(x, t) \quad (2.1b)$$

can, when loss is neglected, be reduced to the quite simple:

$$\partial_x V(x, t) = -L_l \partial_t I(x, t)$$

$$\partial_x I(x, t) = -C_l \partial_t V(x, t)$$

This formulation leads to a wave equation with the phase velocity $v_{ph} = (L_l C_l)^{-1/2}$. With the phasor ansatz $V = V e^{-i\omega t}$, we find the solutions to Eq. (2.1):

$$V(z) = V_0^+ e^{ikx} + V_0^- e^{-ikx} \quad (2.3a)$$

$$I(z) = \frac{V_0^+}{Z_0} e^{ikx} - \frac{V_0^-}{Z_0} e^{-ikx} \quad (2.3b)$$

where $k = \omega/v_{ph}$ is the wave number, and ω is the frequency in units of Hz.

Together, L_l and C_l define the so-called characteristic impedance $Z_0 = \sqrt{L_l/C_l}$, determining how electromagnetic waves propagates in a medium. We will return to this parameter later. When Z_0 changes through the transmission line and differs from the *load impedance* $Z_L = V(0)/I(0)$, reflections will arise. This effect is described by the reflection coefficient [34]:

$$\mathcal{R} = \frac{Z_L - Z_0}{Z_L + Z_0} \quad (2.4)$$

Generally, and especially in quantum circuits, it is highly desirable to avoid reflections, and for this reason the impedance is usually matched to 50Ω , the standard of commercial electronics, in order to keep the reflection coefficient zero.

It is worth noting that the impedance can be function of position. Over long distances (relevant in particular for long transmission lines), V and I oscillates, and only the power P is conserved⁵.

In certain cases the impedance is varied periodically (so-called dispersion engineering) in the context of wave-mixing dynamics [35]. This has the purpose of compressing higher order harmonics of the pump, enhancing the amplifier's efficiency. Early generations of our amplifier presented in Chap. 5, included broadenings of the transmission every few hundred μm for this purpose, leading to band gaps in the transmission spectra. However, we did not exploit this feature in the measurements and abandoned it in later fabrication processes.

2.1.2 Coplanar Waveguides and Resonators

Coplanar waveguides (CPW) can be considered two-dimensional (flat) co-axial cables, where the center strip corresponds to the center pin of the cable, and the ground is the surrounding plates (marked in green and blue respectively in Fig. 2.1(a)). Obviously this analogy is not complete; in the CPW geometry the 2D ground plates are only semi-infinite, and to ensure a common global ground, one can add dielectric cross-overs (Fig. 2.1(b) shows an example), or alternatively airbridges (see Appendix B) [36].

Without employing lumped elements, LC -resonators can be implemented by CPW due to the electromagnetic fields spanning the gaps between the ground and the center-strip. The exact values of L and C (*not* per unit length, but in total) are determined by the geometry of the waveguides (see also Sec. 4.2). We relate to transmission line resonators that are open in one end and closed in the other (i.e. shortened to ground) as $\lambda/4$ resonators, referring to the line's spatial extension $l = \lambda/4$. The input impedance Z_{in} at distance $-l$ from the load is then [34]:

$$Z_{in} = \frac{V(x = -l)}{I(x = -l)} = Z_0 \frac{Z_L + jZ_0 \tan(\gamma l)}{Z_0 + jZ_L \tan(\gamma l)} \quad (2.5)$$

where $j = -1i = -\sqrt{-1}$, and where we have generalized k of Eqs. (2.3) to be the complex propagation constant γ , that may include loss. But without loss $\gamma = k = \omega\sqrt{L_l C_l}$, and the fundamental angular frequency ω becomes

$$\omega = \frac{2\pi}{4l\sqrt{LC}} \quad (2.6)$$

because for this frequency $Z_{in} = Z_L$.

⁵This is true only when dealing with lossless transmission lines.

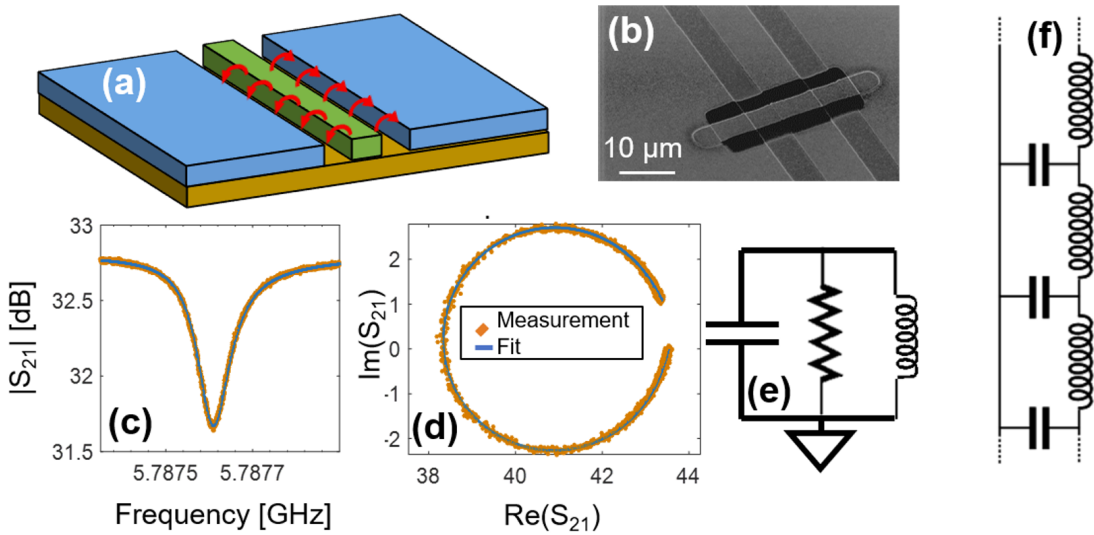


Figure 2.1: CPW and transmission lines. (a) The electromagnetic fields (marked in red) span the gap from the center strip (green) to the grounds (blue). This assumed the substrate (yellow) is not conducting. (b) SEM image of CPW, where grounds are shortened by a metal band-aid on top of a piece of insulating dielectric. (c) S_{21} of transmission line coupled to resonator. (d) Polar (parametric) representation of transmission around the fundamental frequency. (e) Equivalent circuit of the resonator. (f) Model of the infinite transmission line [37].

Transmission lines that are open (in the electrical sense) in both ends are referred to as $\lambda/2$ resonators, and their fundamental frequency is $\omega = \frac{2\pi}{2l\sqrt{LC}}$.

The measurement of a $\lambda/4$ -resonator is exemplified in Figs. 2.1(c)-(d) and fitted, using the response function of a harmonic oscillator. The measurement involves not only the transmission line resonator itself, but also a readout line, terminated in either end by macroscopic (~ 0.3 mm) launchers, allowing injection and collection of microwaves (i.e. measuring S_{21}). When the resonator is coupled sufficiently strong to this line, constant wave (CW) signals are absorbed around the fundamental frequency, resulting in a decrease of S_{21} , and a "flip" of the phase. Sec. 2.1.3 discusses couplings in details.

2.1.3 Circuits Couplings

Most academic freshman courses on electromagnetism includes the topic of mutual inductance. The alternation of current in one conductor changes the magnetic field in the vicinity, and when the other conductor is close enough, the electromotive force generates a current by Faraday's law. Likewise, the accumulation of charges in two-dimensional geometries such as the coplanar superconducting circuitry leads to a mutual coupling capacitance between the charged electrodes, which can be approximated by [38]:

$$C_c = \frac{\epsilon}{\pi} \int \int \frac{dA_1 dA_2}{|r_1 - r_2|^3} \quad (2.7)$$

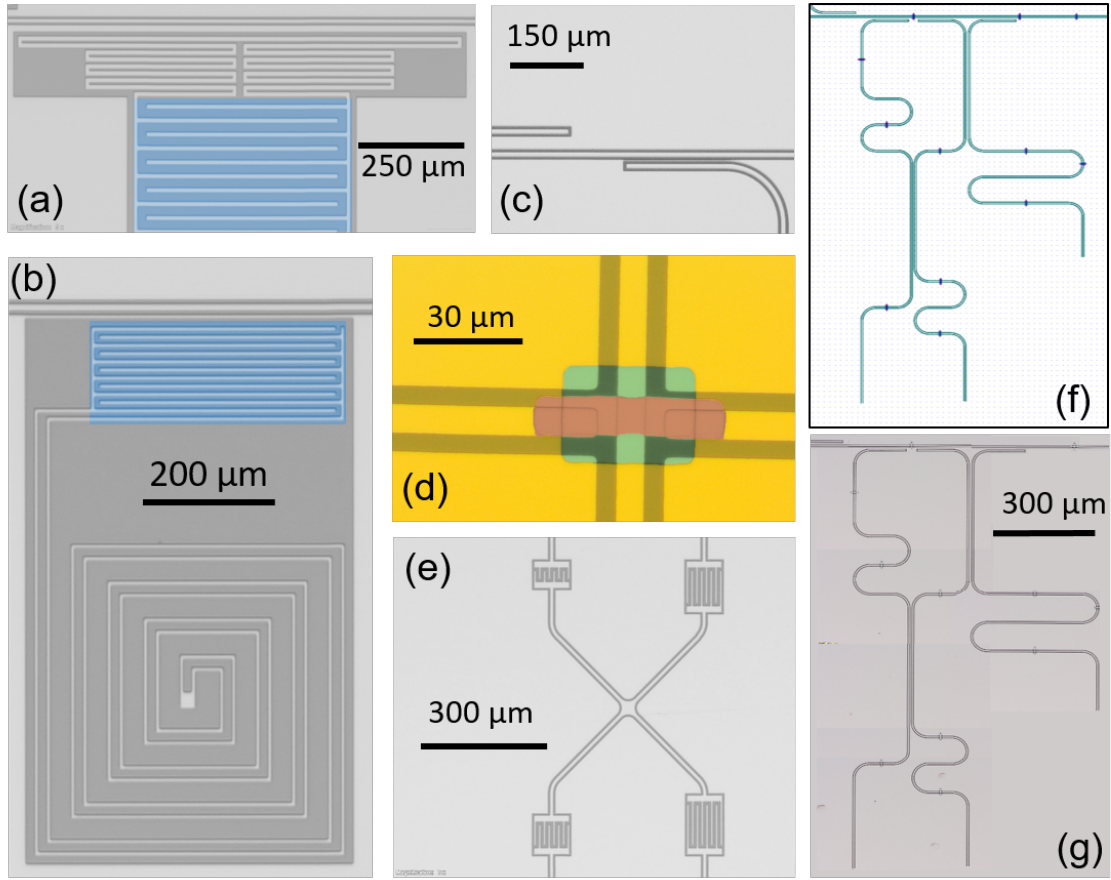


Figure 2.2: Capacitors and couplings in circuitry. (a) False-colored optical microscope (OM) image of a floating lumped element resonator, with the inductor coupled to a readout line and the capacitor marked in blue. (b) The same as (a), but with alternative inductor-geometry and with the capacitor coupled to the readout line. (c) OM image of the coupling region between two $\lambda/4$ -resonators and a transmission line. The upper resonator coupled much weaker than the lower (due to larger gap). (d) False-colored SEM image of parallel-plate coupling between two resonators. Yellow: Base layer sputtered Al. Green: SiO₂ insulator. Red: Evaporated Al connecting the "broken" trace. (e) OM of coupling island, to which four resonators are coupled. (f) CAD file for the fabrication of three coupled resonators. Note the occasional dielectric cross-overs. (g) OM of the fabricated device in (f). This illustration is a collage of numerous images (the entire device did not fit into one frame).

where ϵ is the dielectric constant of the material spanning the gap between the electrodes⁶. The integrals in Eq. (2.7) run over the areas A_1 , A_2 , and r_1 and r_2 denote their coordinates. This equation also gives a good approximation in many cases with electrodes whose thickness is much smaller (typically 100 nm) than the characteristic dimensions of the areas (often a few μm). Examples include the coupling between adjacent transmission lines with or without screening grounds between them (e.g. between $\lambda/4$ resonators coupled to a readout line in Fig. 2.2(c) or mutually coupled resonators in Fig. 2.2(g)). But it fails when the width of one of these lines is significantly larger than the other.

An alternative approach to create large capacitance is the so-called interdigitated electrodes, used in lumped element *LC*-resonators in Fig. 2.2(a) and 2.2(b), and for the coupling of four resonators to a common "coupling island" in Fig. 2.2(e). Parallel plates (Fig. 2.2(d)) is a third option.

⁶If the gap is defined by etching away a metal surface, an effective value for ϵ can be taken as the average of the dielectric constants of the vacuum and the substrate.

Given the capacitive coupling between electrodes and each of the self-capacitance (i.e. capacitance to ground) of each of them C_1 and C_2 , the coupling strength is:

$$g_c = \frac{1}{2} \frac{C_c}{\sqrt{(C_1 + C_c)(C_2 + C_c)}} \sqrt{f_1 f_2} \quad (2.8)$$

This expression is somewhat reduced, under the (most often justified) approximation that $C_1, C_2 \gg C_c$. The Hamiltonian of a system of two coupled capacitors, indexed 1 and 2 is

$$\hat{\mathcal{H}} = \left(\frac{q_1^2}{2C_1} + \frac{\phi_1^2}{2L_1} \right) + \left(\frac{q_2^2}{2C_2} + \frac{\phi_2^2}{2L_2} \right) + \frac{C_c}{C_1 C_2} q_1 q_2 \quad (2.9)$$

where the last (blue) term is the coupling. The corresponding coupling energy is then $E_c^C = C_c V_1 V_2$.

The overlap of magnetic fields from two inductors results in a *inductive* coupling. Mutual inductance is, as already stated, a topic familiar to more physicists than mutual capacitance, perhaps because of its applications in electrical engineering. When connecting two waveguides through lumped-element inductors, the coupling can effectively be modelled as inductive, with a coupling strength analogous to Eq. (2.8), but the energy in the inductor is now $E_c^L = L_c I_1 I_2$.

2.2 Quantizing the LC-resonator

To find the Hamiltonian of an *LC* resonator as described in the former section, we start with the energies of the capacitor and an inductor, $E_C = \frac{CV^2}{2}$ and $E_L = \frac{LI^2}{2}$. Our canonical variable will be the branch flux

$$\phi = \int_{\infty}^t V dt$$

Using that the time derivative of the charge is $\dot{q} = I$, and that the voltage on an inductor is $V = LI$, the Langrangian can be expressed as:

$$\hat{\mathcal{L}} = \frac{C\dot{\phi}^2}{2} - \frac{L\dot{q}^2}{2} = \frac{C\dot{\phi}^2}{2} - \frac{\phi^2}{2L} \quad (2.10)$$

We now note that $\frac{\partial \hat{\mathcal{L}}}{\partial \dot{\phi}} = C\dot{\phi} = q$, so we can write the Hamiltonian:

$$\hat{\mathcal{H}} = \frac{q^2}{2C} + \frac{\phi^2}{2L} \quad (2.11)$$

In analogy with oscillating mechanical systems such as springs, C represents mass, ϕ position of the center of mass, and $1/L$ the spring constant.

When quantizing the electrical circuit, variables becomes operators [37]. When q and ϕ turn into \hat{q} and $\hat{\phi}$, we require their commutator to be $[\hat{q}, \hat{\phi}] = i\hbar$, similar to

the case of mechanical quantum oscillators, where the position and momentum \hat{x} and \hat{p} have the same commutation relation. And just as \hat{x} and \hat{p} , also \hat{q} and $\hat{\phi}$ can be defined in terms of the ladder operators, [21, 37]:

$$\hat{\phi} = \sqrt{\frac{\hbar Z}{2}}(\hat{a} + \hat{a}^\dagger) \quad (2.12a)$$

$$\hat{q} = -i\sqrt{\frac{\hbar}{2Z}}(\hat{a} - \hat{a}^\dagger) \quad (2.12b)$$

This leads to the definition of $\hat{\mathcal{H}}$ in the number basis:

$$\hat{\mathcal{H}} = \hbar\omega\left(\hat{a}^\dagger\hat{a} + \frac{1}{2}\right) \quad (2.13)$$

well-known as the mechanical quantum oscillator. The operator product $\hat{a}^\dagger\hat{a}$ is simply the number of excitations, i.e. the population.

2.3 Superconducting Qubits

At this stage it would be natural to extend our discussion to SC qubits. But a central feature of these is the nonlinearity arising from the special properties of the Josephson Junctions, a special constellation of SC materials. Therefore, prior to the section on qubits we make the detour through some general aspects of superconductivity.

2.3.1 Superconductivity from Kamerlingh Onnes to Ginzburg-Landau

Throughout the last few centuries, theoretical predictions of new physics has often preceded the empiric evidence. Examples of this order of events include the discovery of planetary bodies or the existence of elementary particles, e.g. the neutrino.

Superconductivity, on the other hand, had no genuine explanation by physicists and was not expected theoretically, when Heike Kamerlingh Onnes observed the disappearance of the electrical resistance in mercury below a critical temperature T_c (for this material, 4.19 K) in 1901. The no less surprising perfect diamagnetism of superconductors⁷ (bench-marked by Walther Meissner's demonstration in 1933 of the expulsion of magnetic fields in superconductors), was described by the London brothers in 1935 in a classical model, that included the important *penetration depth*

$$\lambda_L = \sqrt{\frac{m}{\mu_0 n(T) \cdot q^2}} \quad (2.14)$$

⁷The discussion of different magnetic behaviour between so-called "soft" and "hard" superconductors lies outside the scope of this work. We will also refrain from the distinction between superconductors of type I and type II.

where m , n , and q are the charge carriers' mass, their temperature dependent density, and their charge respectively, and μ_0 is the vacuum permeability.

The magnetic field in the superconductor decays exponentially with the constant λ_L :

$$B(x) = B_0 e^{-x/\lambda_L} \quad (2.15)$$

where x is the distance from the sample's surface. The value of λ_L depends on temperature and material, and in most superconductors it is between 10^{-9} m and 10^{-6} m. Since Kamerlingh Onnes' initial discovery, superconductivity has been demonstrated for countless materials, including elements as well as alloys. For obvious reasons the research community is especially interested in identifying high- T_c superconductors, a goal that has been achieved by applying e.g. extremely high pressures or infrared pulses to deform the lattice [39].

A major advance in the understanding of superconductivity was the formulation of the Bardeen-Cooper-Schrieffer (BCS) theory of 1956, describing the mutual attraction between two electrons in the superconductor by virtual phonons⁸ together constituting a so-called "Cooper pairs", effective particles who obey Bose-Einstein statistics.

It is quite counter-intuitive that such an interaction can exist, because (theoretically at least) it implies that the *best* superconductors (or, more quantitatively, the superconductors with the highest T_c) are those with strongest interaction between lattice and charge carrier; a property that in normal conductors is responsible for resistance.

Formally, we can express the interaction with the BCS Hamiltonian. The electrons in a Cooper-pair carry opposite spin σ and orbital momentum k , and this leads to the definition:

$$\mathcal{H}_{BCS} = \sum_{\mathbf{k}\sigma} \xi_k c_{\mathbf{k}\sigma}^\dagger c_{\mathbf{k}\sigma} + \frac{1}{N} \sum_{\mathbf{kk}'} V_{\mathbf{kk}'} c_{\mathbf{k}\uparrow}^\dagger c_{-\mathbf{k}\downarrow}^\dagger c_{-\mathbf{k}'\downarrow} c_{\mathbf{k}'\uparrow} \quad (2.16)$$

In Eq. (2.16) c and c^\dagger represent the fermionic annihilation and creation operators with k and σ as indicated by the subscripts; $\xi(\mathbf{k}) = \epsilon(\mathbf{k}) - \mu(\mathbf{k})$ is the total k -dependent energy of a Cooper pair, a function of ϵ , the Fermi energy and μ , the chemical potential, and $V_{\mathbf{kk}'}$ the interaction element of the scattering matrix.

The BCS theory includes various extensions covering aspects of different superconductors, but we limit the present discussion to include only what is necessary the purpose of the rest of the thesis. One central property of superconductors is the energy gap Δ_g that sets the temperature dependent energy necessary to break a Cooper pair:

$$\Delta_g(T = 0) \simeq 1.76 k_b T_c \quad (2.17)$$

⁸By definition, the mutual charge carrier attraction does not generate a phonon in the classic sense. This would imply interaction with the lattice, i.e. conventional resistance.

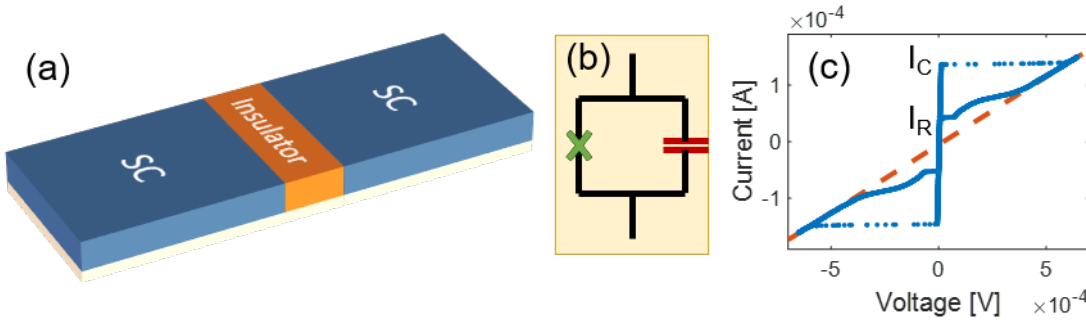


Figure 2.3: Josephson Junction. (a) Graphical illustration of the S-I-S junction. (b) Equivalent circuit. The physical tunnel junction is a pure Josephson (nonlinear) inductive element (green) shunted by a capacitor (red). (c) Hysteretic IV characteristic of an underdamped JJ.

where k_b is the Boltzman constant. In most text books, Δ_g is defined as the difference in energy between an unbound electron in the superconducting state, and an electron bound in a pair. It therefore takes $2\Delta_g$ to break a pair.

Where the London brothers introduced the important constant λ_L , the *penetration depth* (not to be confused with the wavelength λ to be introduced later), describing how the magnetic fields decay on the surface film and into the bulk of superconductors, the BCS theory presented another length parameter, the *Cooper pair coherence length*, ξ_0 . This material-dependent number represents the average distance between the electrons in a pair, typically between 10^2 and 10^3 nm.

But superconductivity is, as earlier indicated, a *macroscopic* quantum phenomenon. As it turns out, all Cooper pairs, no longer governed by Fermi-Dirac statistics as the unpaired electrons, can occupy one common energetic state together as a condensate. Ginzburg and Landau described this in their phenomenological theory using a single wave function ψ , where $|\psi|^2 = n_s$ is the spatial density of pairs⁹. For superconducting qubits, the phase of ψ , denoted φ , is essential for the nonlinear oscillators, as we shall see below.

2.3.2 Josephson Junctions

In addition to the capacitor and the inductor, two classical electrical circuit components, the superconducting circuits benefit from the so-called Josephson Junction (JJ) [40]. This element consists of two SC electrodes separated by an insulator¹⁰ as shown in Fig. 2.3(a). In this section, we will see that the inductance of the JJ is nonlinear and that this is of vital importance for SC qubits¹¹.

Consider the Josephson equations describing the current and voltage through a

⁹The Ginzburg-Landau theory was presented for the first time in 1950, prior to the BCS, but was further developed in the following years.

¹⁰There are in fact many possible "weak links" consisting of superconducting electrodes demonstrating nonlinearity, e.g. S-N-S (superconductor-normal material-superconductor) junctions, S-I-S (superconductor-insulator-superconductor) junctions, and S-C-S (superconductor-constriction-superconductor) junctions [41].

¹¹As all other components of electrical circuits, real JJs have finite capacitance C_J and inductance L_J - see Fig. 2.3(b). In certain superconducting qubits a much larger capacitance is added in parallel, and C_J becomes negligible.

JJ:

$$I(t) = I_c \sin(\varphi(t)) \quad (2.18a)$$

$$V = \frac{\Phi_0}{2\pi} \frac{\partial \varphi}{\partial t} \quad (2.18b)$$

where $\Phi_0 = \hbar/2e$ is the magnetic flux quantum. I_c is the critical current¹²; for $|I| > |I_c|$ the junction becomes resistive. This dramatic phenomenon is displayed in Fig. 2.3(c), where we monitor the voltage over a JJ, while the current is scanned. At I_c the voltage suddenly becomes nonzero, and disappears again only after the current decreases to $I < I_r$, the retrapping current¹³.

At currents $|I| \gg |I_c|$, the JJ behaves like an ordinary resistor. The orange broken line in Fig. 2.3(c) marks the linear IV -characteristic, and the Ambegaokar-Baratoff formula links the slope, i.e. the normal resistance R_n to the critical current:

$$R_n I_c = \frac{\pi \Delta_g}{2e} \quad (2.19)$$

Eq. (2.19) is especially useful for the experimental physicist, who wants an estimate of I_c without cooling down devices to sub-Kelvin temperatures. The room temperature resistance, usually close to R_n at cryogenic temperatures (at least for certain materials) provides a prediction of I_c , even far from the SC state.

Returning to Eqs. (2.18), we reveal the nonlinearity by differentiating the current equation and substituting into the voltage equation:

$$\frac{\partial I}{\partial t} = I_c \cos(\varphi(t)) \frac{\partial \varphi}{\partial t} \Rightarrow V = \frac{\Phi_0}{2\pi} \frac{\partial I / \partial t}{I_c \cos(\varphi(t))} \quad (2.20)$$

By definition of inductance the Josephson inductance is:

$$L_J = \frac{\Phi_0}{2\pi I_c \cos(\varphi(t))} \quad (2.21)$$

In analogy with linear inductors, the Josephson energy (of a JJ) can be found using Eqs. (2.18):

$$E_J = \int dt IV = I_c \frac{\Phi_0}{2\pi} \int \sin(\varphi(t)) \frac{\partial \varphi}{\partial t} = -\frac{I_c \Phi_0}{2\pi} \cos(\varphi(t)) \equiv -E_{0,J} \cos(\varphi(t)) \quad (2.22)$$

According to this definition, $E_J = L_J I_c^2$, parallel to the definition of the energy stored in linear inductor with inductance L .

¹²In the original paper by Josephson (Ref. [40]), the pre-factor of sine was simply denoted I_0 . Only later it was proven that $I_0 = I_c$, the critical current of the JJ.

¹³In many cases, $I_r \lesssim I_c$, but not necessarily $I_r \ll I_c$. Fig. 2.3(c) displays the case of an underdamped JJ, with $Q = \omega_p RC > 1$, where $\omega_p = \sqrt{(2eI_c/\hbar C)}$ is the JJ's plasma frequency [33]

2.3.3 Qubits based on Josephson Junctions

Qubits, whether SC or not, are TLSs or at least nonlinear systems, where two levels can be addressed and distinguished from the others. Practically, their states $|0\rangle$ and $|1\rangle$ has to be defined by some measurable physical quantum parameters, allowing superposition of states, entanglement, etc. Electrons, for example, can serve as qubits, using their spin to define the state (i.e. $|0\rangle = |\uparrow\rangle, |1\rangle = |\downarrow\rangle$).

In Sec. 2.1.2 we treated the classical linear *LC*-resonator. Its linear quantum-sister, the harmonic oscillator is a basic problem for students in undergrad quantum mechanics courses. Solving the Schrödinger equation of a quadratic potential yields the harmonic energy levels, as shown in Fig. 2.4(a). When the linear inductor is replaced by a JJ, its nonlinear L changes the game, and the oscillator becomes anharmonic. The simplest method to realize a SC qubit is therefore to use the JJ only (exploiting the capacitance shunting the inductive element). This is, roughly speaking, the historical phase qubit¹⁴. Additional pioneering SC qubits are listed in Table 2.1.

Over the last two-three decades several SC qubits have been suggested and implemented. Besides the most basic devices, some of the significant implementations include the fluxonium [42], the quantronium [43], and as of this writing the quite popular transmon [44]. Shortage of space in this thesis limits the further description and comparison of the many types of SC qubits beyond what we list in Table 2.1¹⁵. Instead, we will turn the focus to the transmon and its grounded twin, the Xmon, shown in Fig. 2.4).

Two key figures of any SC qubit is its Josephson energy, E_J , already defined in Eq. (2.22), an its charging energy

$$E_C = \frac{e^2}{C_J + C} \quad (2.23)$$

where C_J is the capacitance of the JJ and C the shunting capacitance. E_C equals the anharmonicity [45]:

$$E_C/\hbar = \Delta\omega = \omega_{12} - \omega_{01} \quad (2.24)$$

where

$$\omega_{ab} = \omega_b - \omega_a = \frac{E_b - E_a}{\hbar}$$

and E_a and E_b are the energy of the a'th and b'th level¹⁶. Some SC qubits work in the regime of $E_J/E_C < 1$ [46], to ensure a strong distinction between the qubit's

¹⁴In practice, and to allow control, the phase qubit is operated with a bias current, leading to the so-called "tilted washboard" potential, $U(\varphi) \propto I_c \cos(\varphi) - I\varphi$. When a current in the appropriate range is applied, the energy levels are confined in local minima of $U(\varphi)$, and two adjacent wells can serve as qubit states.

¹⁵The interested reader is referred to Refs. [16, 45].

¹⁶The anharmonicity, $\Delta\omega$, is often denoted as α in the scientific literature. In this thesis, α is the kinetic inductance fraction to be introduced in Chap. 3.

Prototypes of SC qubits		
Name	Hamiltonian	Unit of info
Phase qubit	$\mathcal{H} = \frac{(2eq)^2}{2C_J} - I_c \frac{\Phi_0}{2\pi} \varphi - E_{0J} \cos(\varphi)$	Energy level
Flux qubit	$\mathcal{H} = \frac{q^2}{2C_\Sigma} - \left(\frac{\Phi_0^2}{2\pi} \right)^2 \frac{1}{2L} \varphi - E_{0J} \cos(\varphi - \frac{2\pi\Phi}{\Phi_0})$	Current flow
Charge qubit	$\mathcal{H} = 4E_C(N - N_g)^2 - E_{0J} \cos(\varphi)$	Occupation

Table 2.1: The phase qubit is current-biased JJ (and thus effectively an LC -circuit), where its energy level constitutes the qubit states. The flux qubit includes an independent loop of a JJ and an inductor, and the current flow direction (clockwise/anti-clockwise) defines the states $|0\rangle, |1\rangle = (\mathcal{O} \pm \mathcal{U})\sqrt{2}$. The charge qubit or "Cooper Pair Box" includes an "island" (between the JJ and an additional capacitor). Here the number operator, i.e. the number of Cooper pairs on the island, define the states: $|N\rangle, |N+1\rangle$. Symbols in the Hamiltonians: $C_J, L_J(C, J)$: Capacitance, inductance of JJ (of external capacitor/inductor). q, N : Charge and number operators. E_C is the charging energy defined in the main text, and N_g the charge noise. In this table we have omitted the "hat" notation of operators (e.g. \hat{A}) to ease the readability.

transitions, but the large E_C results in increased sensitivity to charge noise. For this reason many other qubits work in the transmon regime of $E_J/E_C \sim 10^1\text{-}10^2$ [47].

The equivalent circuit of the Xmon is shown in Fig. 2.4(b). It consists of a capacitor with four electrodes optimizing the possible connectivity and control probes, and one electrode is grounded through a loop with two JJ's. This is a so-called SQUID to be described in detail shortly.

The connectivity is the Achilles heel of all SC qubits. Obviously the best way to preserve the quantum state is by total isolation, but without connectivity we can neither manipulate nor measure the state. Fortunately, there are various techniques to get around this, as we will see in the following.

2.3.4 SQUIDs and Qubit Tunability

An exciting feature of the nonlinearity becomes clear, when we look back at Sec. 2.3.1. There we presented the phase φ of the wave function in Ginzburg-Landau theory. Based on the uniqueness of the solution, which we must require, one can show that in closed SC current loops,

$$\oint dl\varphi = 2\pi n, n \in \mathbb{N} \quad (2.25)$$

This requirement does not change, when the loop is interrupted by one or more JJs. If an external magnetic field is applied, the flux Φ through the loop must equal $\Phi_0 \cdot n$, due to the resulting vector potential¹⁷. Otherwise Eq. (2.25) does not hold. To ensure such a value of Φ , a current I_{ext} is induced, and it flows either clockwise or counter-clockwise¹⁸, whatever direction requires the least energy to reach an integer of Φ_0 [33].

For simplicity, we assume that the JJs are identical, each with the same critical current I_c , but the same principles will hold even when the critical currents differ. In any case they have to obey Eqs. (2.18) (see Fig. 2.4(d), where the directions are

¹⁷The flux quantization is a manifest of superconductivity being a macroscopic quantum phenomenon.

¹⁸A mathematical proof of the operational principle of SQUIDs can be found e.g. in Refs. [33, 48].

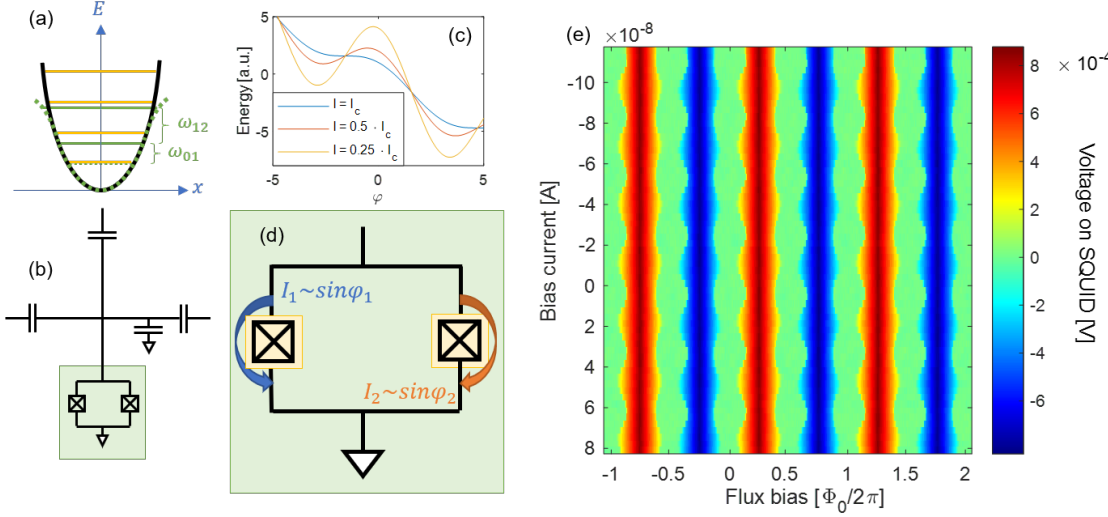


Figure 2.4: (a) The quantized energy levels of the harmonic oscillator (yellow) and of the anharmonic oscillator (green). The lowest level of the latter is marked with a broken line to make it distinguishable from its harmonic counterpart. (b) Equivalent circuit of the transmon qubit with the SQUID marked by green background. (c) Tilted washboard potential as described in main text (potential of the phase qubit). (d) Zoom on the SQUID (with the JJ marked by yellow background) and currents through the loop. (e) Voltage measurement, when scanning flux and current.

arrows indicating the *total* current through both JJs). If a bias current I_b is applied to the loop, the resulting current through the JJs is

$$I_{1,2} = I_b/2 \pm I_{ext}$$

and if $I_{1,2}$ exceeds I_c , the loop becomes resistive. This Superconducting QUantum Interference Device (SQUID) is therefore sensitive to magnetic fields. More exactly, the critical current of the loop is

$$I_c^S = 2I_c \left| \cos\left(\frac{\pi\Phi_{ext}}{\Phi_0}\right) \right| \quad (2.26)$$

The characterization so far is true for the "ideal" SQUID, where the Steward-McCumber number $\beta_L = 2LI_c \ll 1$ [49].

Eq. (2.26) makes the SQUID extremely useful as a magnetometer, capable of detecting weaker magnetic fields than any other physical system. But in the operation of qubits, the flux is not simply measured to determine magnetic field strengths but rather applied intentionally to control currents in the loop, in particular the phases, as they affect the JJs inductance cf. Eq. (2.22). The SQUID is thus practically a handle for tuning the nonlinear *LC*-resonator constituting a qubit, such as the transmon cf. Fig. 2.4(b). And changing L allows modulation of the qubit's frequency (see Eq. (2.6)). The SQUID, in other words, makes the SC qubit *tunable*. We will relate to the other three connections of the Xmon as shown in Fig. 2.4(b) in the next section.

2.4 Quantum Electrodynamics

Having reviewed the most elementary formulae of Josephson physics and its relations to the quantum circuit variables, we are now ready to review the operation of SC qubits.

2.4.1 Hamiltonian of the Xmon

In Sec. 2.2, we quantized an LC resonator and found its Hamiltonian in terms of \hat{q} and $\hat{\phi}$. SC qubits such as the transmon or an Xmon are, as previously indicated, both anharmonic oscillators. In principle the transmon is derived from the charge qubit, and its Hamiltonian is not very different. But it is convenient to express $\hat{\mathcal{H}}$ in terms of the energies E_C and E_L . For a harmonic oscillator, this would be:

$$\hat{\mathcal{H}}_{LC} = 4E_C\hat{n}^2 - \frac{1}{2}E_L\hat{\phi}^2 \quad (2.27)$$

where $\hat{n} = 2q/e$ is the reduced charge and $\hat{\phi} = \Phi/\Phi_0$ is a generalization of the flux we used earlier (with the same notation) and equivalent to φ for JJs [37]). These operators satisfy the commutation $[\hat{n}, \hat{\phi}] = i\hbar$ (like q and ϕ), i.e. $[\hat{\Phi}, \hat{Q}] = i\hbar$, and the Hamiltonian can therefore still be written as Eq. (2.13).

The Xmon, already named as the qubit of our choice, has a nonlinear potential energy. This means the simple $\hat{\phi}^2$ dependence in Eq. (2.27) is replaced with a cosine function:

$$\hat{\mathcal{H}}_X = 4E_C\hat{n}^2 - \frac{1}{2}E_J\cos(\hat{\Phi}_{ext}) \quad (2.28)$$

In Appendix A we show that $\omega_{01} = \sqrt{8E_JE_C} - E_J$, where E_J is the unperturbed energy of the JJs, and $\Delta\omega = E_C$ as above. The Josephson energy is now responsible for (almost) all of the inductive energy stored in the device [21]. The central point in this context is that the inductance term is a direct function of the external flux applied to the SQUID as we saw above. This makes the Xmon a tunable qubit.

2.4.2 The Density Matrix and the Bloch Sphere

We are now concerned with the question of control. How do we excite the Xmon qubit? How to measure its state? The answers to these questions are given by describing the quantum state of the TLS by the density matrix, which in the basis of pure states $|\psi_n\rangle$ is defined:

$$\hat{\rho} = \sum_n p_n |\psi_n\rangle\langle\psi_n|$$

where p_n is the probability of finding the system in the state $|\psi_n\rangle$.

Technically, the density matrix merely generalizes the notation of Dirac formalism. For example, if the system is in some pure state, then $\hat{\rho}$ is simply the outer

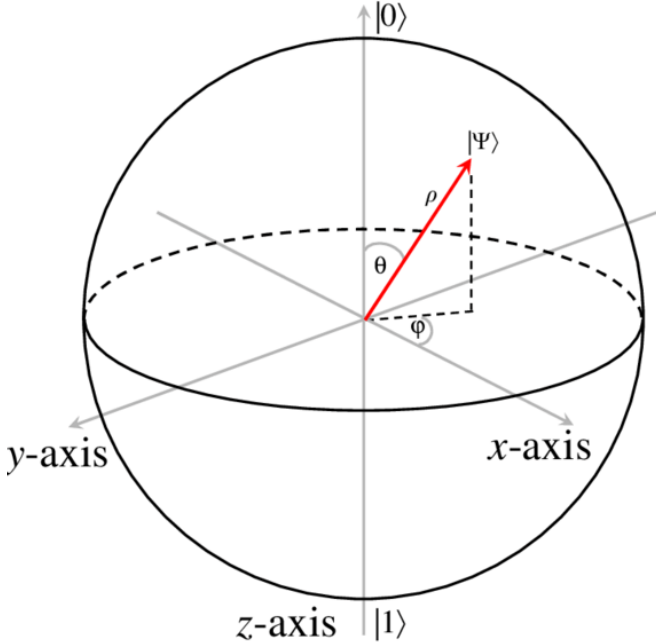


Figure 2.5: The Bloch Sphere visualizes the quantum state (in this case the state $|\Psi\rangle$) of the TLS. The north pole corresponds to the ground state $|0\rangle$, and the south pole to the excited state $|1\rangle$. Any point on the sphere corresponds to a pure state, and points within the sphere to a mixed state. The specific state is thus described in spherical coordinates by a radius and two angles, θ and ψ . By this visualisation, the state $|\Psi_1\rangle = 1/\sqrt{2}(|0\rangle + |1\rangle)$ lies on the x-axis, whereas $|\Psi_2\rangle = 1/\sqrt{2}(|0\rangle - i \cdot |1\rangle)$ lies on the y-axis. Quantum dynamics in the context of TLSs is movements on and inside the Bloch sphere. Image based on [Wikipedia](#) (under Wikipedia Commons License).

product of the state vector and its complex conjugate. In this case $\text{tr}(\hat{\rho}^2) = 1$. However, when decoherence effects occur, the system leaves the pure state (or superposition of pure states). Mixed states have density matrices with $\text{tr}(\hat{\rho}^2) < 1$. We consider decoherence processes in detail in Sec. 2.4.4.

As shown in Fig. 2.5, $\hat{\rho}$ can be specified by spherical coordinates, so that

$$\hat{\rho} = \frac{1}{2} \left(1 + \vec{r} \cdot \vec{\sigma} \right) \quad (2.29)$$

where $\vec{r} = (\sin \theta \cos \varphi, \sin \theta \sin \varphi, \cos \theta)$, and $\vec{\sigma} = (\hat{\sigma}_x, \hat{\sigma}_y, \hat{\sigma}_z)$ is the vector of the Pauli matrices. Here θ and φ relate to the angles in Fig. 2.5, and not to the quantum operators.

Changes of a TLS's quantum state (i.e. of \vec{r}) are associated with movements on the Bloch Sphere. Such changes can be made e.g. by applying an electrical field. The Hamiltonian of a simple TLS with the transition frequency ω_{01} is:

$$\hat{\mathcal{H}}_0 = \hbar \begin{pmatrix} 0 & 0 \\ 0 & \omega_{01} \end{pmatrix} \quad (2.30)$$

If the electric field coupled to the TLS is $\vec{E} = \vec{E}_0 \cos(\omega_{dt})$, we can define the Rabi frequency as

$$\Omega_R = \vec{d} \cdot \vec{E} / \hbar$$

where \vec{d} is the dipole moment of the TLS. Its Hamiltonian then becomes [50]:

$$\hat{\mathcal{H}} = \hbar \begin{pmatrix} 0 & \Omega_R \cos(\omega_{dt}) \\ \Omega_R^* \cos(\omega_{dt}) & \omega_{01} \end{pmatrix} \quad (2.31)$$

We now proceed with the famous rotating wave approximation. This requires that we introduce an auxiliary operator, \mathcal{U} for the subsequent unitary transformation:

$$\mathcal{U}_{int} = \begin{pmatrix} 1 & 0 \\ 0 & e^{-i\omega_d t} \end{pmatrix}$$

With this definition of \mathcal{U} , the transformation of the state vector is $\tilde{\psi} = \mathcal{U}\psi$, where ψ is the state vector in the lab (rest) frame, and $\tilde{\psi}$ in the rotating frame. To determine the shape of the rotating Hamiltonian, we refer to the Schrödinger equation. Writing the state ψ of the lab frame as $\mathcal{U}^\dagger \tilde{\psi}$ we get:

$$i \frac{\partial(\mathcal{U}^\dagger \tilde{\psi})}{\partial t} = \hat{\mathcal{H}} \mathcal{U}^\dagger \tilde{\psi} \quad (2.32)$$

Applying a bit of algebra¹⁹ on Eq. (2.32) reveals the Hamiltonian in the rotating frame:

$$\tilde{\mathcal{H}} = \mathcal{U} \hat{\mathcal{H}} \mathcal{U}^\dagger - i \mathcal{U} \frac{\partial \mathcal{U}^\dagger}{\partial t} \quad (2.33)$$

Plugging $\hat{\mathcal{H}}$ of Eq. (2.31) into Eq. (2.33) returns the Hamiltonian in the rotating frame:

$$\tilde{\mathcal{H}} = \frac{\hbar}{2} \begin{pmatrix} 0 & \Omega_R(1 + e^{2i\omega_d t}) \\ \Omega_R^*(1 + e^{-2i\omega_d t}) & 2\Delta \end{pmatrix} \quad (2.34)$$

Here $\Delta = \omega_d - \omega_{01}$ denotes the detuning (not to be confused with the superconducting gap Δ_g). Usually $\Delta \ll \omega_d + \omega_{01}$. In fact, to drive the field Δ must not be too large²⁰. The rotating wave approximation assumes that $\omega_d \gg \Omega_R$, which is mostly the case. After sufficiently many cycles ($t \gg \omega_d^{-1}$), the average of the rotating terms (with exponents) in Eq. (2.34) vanish. This leaves us with the Hamiltonian of the rotating wave approximation [23, 50, 51]:

$$\tilde{\mathcal{H}} = \frac{\hbar}{2} \begin{pmatrix} 0 & \Omega_R \\ \Omega_R^* & 2\Delta \end{pmatrix} \quad (2.35)$$

Based on Eq. (2.35) we introduce the Rabi vector $\vec{\Omega}$ of coefficients that span $\tilde{\mathcal{H}}$ on the Pauli matrices (i.e. $\tilde{\mathcal{H}} = \vec{\Omega} \cdot \vec{\sigma}$). Since the density matrix as any other quantum operator evolves according to the Schrödinger equation:

$$\hat{\rho}(t) = \tilde{\mathcal{H}} \hat{\rho}(0) \tilde{\mathcal{H}}^\dagger \quad (2.36)$$

With some linear algebra²¹, Eq. (2.36) can be used to present the time evolution of

¹⁹The Schrödinger equation generally reads $i\partial_t \psi = \hat{\mathcal{H}}\psi$. As we open the brackets on the left-hand-side of Eq. (2.32), we get: $i(\partial_t \mathcal{U}^\dagger \tilde{\psi} + \mathcal{U}^\dagger \partial_t \tilde{\psi}) = \hat{\mathcal{H}} \mathcal{U}^\dagger \tilde{\psi}$. Multiplying both sides by \mathcal{U} and re-arranging: $\mathcal{U}i(\partial_t \mathcal{U}^\dagger \tilde{\psi} + \mathcal{U}^\dagger \partial_t \tilde{\psi}) = \mathcal{U} \hat{\mathcal{H}} \mathcal{U}^\dagger \tilde{\psi} \Rightarrow i\partial_t \tilde{\psi} = (\mathcal{U} \hat{\mathcal{H}} \mathcal{U}^\dagger - i \mathcal{U} \hat{\mathcal{H}} \partial_t \mathcal{U}^\dagger) \tilde{\psi}$. This is identical to the Schrödinger equation for the rotating state vector $\tilde{\psi}$, where the purple term is the Hamiltonian in the rotating frame: $i\partial_t \tilde{\psi} = \mathcal{H} \tilde{\psi}$.

²⁰Intuitively, this compares to pushing a swing on a playground. When the pushing is done too far from the resonance frequency of the swing, it will not be effective.

²¹To reach this result, one must write Eq. (2.36) rigorously with Eqs. (2.29) and (2.35).

the density matrix as the rotation of \vec{r} from Eq. (2.29):

$$\frac{\partial \vec{r}}{\partial t} = \vec{\Omega} \times \vec{r} \quad (2.37)$$

The precession of \vec{r} around $\vec{\Omega}$ is known as Rabi oscillations and has been observed in different quantum optical systems. Defining $\vec{\Omega}$ wisely (and implementing it correctly) is thus the key to coherently driving the qubit. When $\Omega_z = 0$, the trajectory of the point representing $\hat{\rho}$ on the Bloch sphere must include both the north and the south pole. In other words, this resonant drive can excite the qubit²². We will refer to this operation as "xy-control".

2.4.3 Jaynes-Cummings and Dispersive Readout

In driving a qubit it must couple to a field as we saw above²³. Ignoring all other states of the qubit than $|0\rangle$ and $|1\rangle$, and assuming energy conservation, the *entire* system, including both field and atom, can be described by the Jaynes-Cummings Hamiltonian²⁴:

$$\hat{\mathcal{H}}_{JC} = \hbar \left(\frac{\omega_{01}}{2} \hat{\sigma}_z + \omega_r \left(\hat{a}^\dagger \hat{a} + \frac{1}{2} \right) + g(\hat{a} \hat{\sigma}^+ + \hat{a}^\dagger \hat{\sigma}^-) \right) \quad (2.38)$$

where $\hat{\sigma}_z$ is the z-Pauli matrix, $\hat{\sigma}^+ = |1\rangle\langle 0|$, $\hat{\sigma}^- = |0\rangle\langle 1|$ (i.e. excitation and annihilation of the qubit), ω_r is the resonance of the field (the resonator in our experiments), and g is the coupling strength, e.g. as we described it in Eq. (2.8) for a capacitive coupling. In Eq. (2.38) the **first** term relates to the state of the qubit, the **second** term to the state of the field, and the **third** term describes the interaction.

For large detuning, i.e. $\Delta \gg g$ the Jaynes-Cummings Hamiltonian can be re-written [52]:

$$\hat{\mathcal{H}}_{JC}^d = \hbar \left(\frac{\omega_{01}}{2} \hat{\sigma}_z + \left(\omega_r + \frac{g^2}{\Delta} \hat{\sigma}_z \right) \left(\hat{a}^\dagger \hat{a} + \frac{1}{2} \right) \right) \quad (2.39)$$

This would resemble the sum of two independent systems' Hamiltonians, except for the appearance of $\hat{\sigma}_z$ in the prefactor (marked in **blue** in Eq. (2.39)) of the field's Hamiltonian. In other words, the field's frequency depends directly on the qubit's state: $\omega_r \rightarrow \omega_r \pm \frac{g^2}{\Delta}$. Therefore, working in the *dispersive* regime ($\Delta \gg g$) allows reading the qubit's state indirectly. And it makes the coupling between readout transmission lines and qubits unnecessary - isolating the qubit further from external noise and loss channels.

The discussion so far (and in the rest of this thesis) concerns "ideal" qubits. These are TLSs with extreme anharmonicity $\eta = (\omega_{12} - \omega_{01})/2\pi$, where all other

²²Exciting the qubit requires that the applied pulse is applied at the qubit frequency, and for the correct time duration. In particular, since only half a circle is required to bring a qubit from $|0\rangle$ to $|1\rangle$, this is called a π -pulse.

²³In our case, this is done by a coupled probe, the XY-control.

²⁴Eq. (2.38) presents the Jaynes-Cummings hamiltonian in the Schrödinger picture after the rotating wave-approximation

Connectivity of the Xmon			
Connector	Purpose	Coupling	Operation
SQUID	Tune ω_{01}	Inductive	Apply Φ_{ext} by near DC-line
XY probe	Excite qubit	Capacitive	Drive, cf. Eq. (2.35)
Resonator	Readout	Capacitive	Drive through transmission line
Quantum bus	Network	Capacitive	Passive

Table 2.2: Proposed connectivity to the four "arms" of the Xmon as displayed in Fig. 2.4: The SQUID is bias by the magnetic field from a DC line in the vicinity, thus changing its L and thus ω_{01} . The XY control drives the qubit as described in Sec. 2.4.3. Measuring the qubit's state is done through a readout resonator, coupled both to the qubit and to a transmission line. When constant waves are applied to the latter, the former absorbs at the resonance frequency, cf. Fig. 2.1, revealing the qubit's state. And coupling to other qubits is possible through a quantum bus - or, alternatively directly to the same arm of other Xmons [54].

energy transitions but those of the qubit operation are relevant (i.e. $|\eta| \rightarrow \infty$). However, when this is not the case (i.e. when $|\eta| \lesssim |\Delta|$) the dispersive shift is affected by ω_{12} , and instead of the expression in Eq. (2.39), it becomes [53]:

$$\omega_r \rightarrow \omega_r \pm \frac{-2g^2\eta}{\Delta^2(1 + \eta/\Delta)} \equiv \omega_r \pm \chi \quad (2.40)$$

An important deduction of Eq. (2.40) is that even when Δ is positive (the qubit's bare frequency lies above the resonator frequency), a negative η will result in an "inverse" dispersive shift: The measured resonator frequency will be $\omega_r - \chi$, when the qubit is in the $|1\rangle$ state, and $\omega_r + \chi$ when in the $|0\rangle$ state, opposite of what one expects in the case of $\Delta > 0$ and $|\eta| \rightarrow \infty$.

2.4.4 Decoherence

In principle, quantum systems could be kept in their initial states forever, if they were perfectly isolated from the environment. But it is extremely difficult, if not practically impossible, to completely isolate a quantum system. Moreover, as physicist interesting in manipulating, or at least observing the quantum state, this kind of isolation is useless. Any realization of the SC qubits is therefore the target of noise from the environment, a process that eventually destroys the quantum state of the system.

From a computational perspective decoherence is obviously a disturbing phenomenon, but acceptable if the relevant operations (the "gates", that we shall not relate to here) can be applied and the results are registered, before the destruction of the state. For this reason the *rate* of decoherence is of vital importance.

Decoherence can be classified as one of two phenomena. In the first, *amplitude damping*, the system loses its energy, and the vector \vec{r} defined in Eq. (2.29) decays to the north pole of the Bloch sphere: $|0\rangle$, as $\theta \rightarrow 0$. The rate of amplitude damping is usually denoted by T_1 .

In the second kind of decoherence, pure *dephasing*, φ (the azimuth angle of \vec{r})

does *not* decay, but becomes random, while θ is conserved. If indeed pure, the process of dephasing reduces $\vec{\rho}$ and aligns it with the z-axis with the rate usually denoted by T_φ .

Amplitude damping has, strictly speaking, parallels in classical systems. One can easily imagine the loss of energy from a classical harmonic oscillator, e.g. a spring, that eventually ceases to move some time after the children have gone home. Dephasing reflects the loss of information without the loss of energy.

Obviously, amplitude damping results in dephasing, since the decay to $|0\rangle$ inevitably results in the loss of a well-defined φ . The measurement of T_1 includes applying a so-called π -pulse, making the rotation from $|0\rangle$ to $|1\rangle$, and then measuring the population after various time scales (and finally plotting to determine the decay rate). Based on these considerations, the so-called T_2 decoherence describes dephasing due to both T_1 and T_φ :

$$\frac{1}{T_2} = \frac{1}{2 \cdot T_1} + \frac{1}{T_\varphi} \quad (2.41)$$

There is so far no known practical generalization of the Bloch sphere that easily visualizes the states of multi-state systems. Visual descriptions of the effect of decoherence on larger systems and composite structures (with coupled TLSs) is therefore hard to present. But given T_1 and T_φ we can simulate the decoherence with the Krauss operators (more on this in Sec. 4.1.1).

Decoherence is a central concept in quantum dynamics. Since formally introduced in Ref. [55], it has become clear to the scientific community that systems for quantum measurements must be well isolated from the environment.

2.5 Boson Sampling

We are now ready, having reviewed all the necessary tools, to introduce boson sampling, an interesting approach to multimode dynamics. As the name suggests, boson sampling is the task of sampling the distribution of bosons, subsequent to their performance of a coherent quantum walk in a linear network. We will clarify this definition below, but first we discuss its purpose.

2.5.1 Quantum Advantage

Boson sampling originally became a topic of attention in the quantum information community, when its implementation was associated with quantum supremacy [2]. This term was later replaced with the more politically correct expression "quantum *advantage*" [56]. The general idea is that certain probability distributions are sampled by a boson sampling device much faster than the alternative classical computation. For large Hilbert spaces, it is even expected that the classical computation would require extended time periods. The anticipation of solving the

problem, yet to be exactly specified, by a quantum experiment will then prove the superior capabilities of quantum devices.

Though SC networks are based on a quantum phenomenon (superconductivity), a linear network of coupled modes can be characterized, simulated, and even operated with all-classical modes. On the other hand, the excitation of single-photon modes, which we will identify as a central part of the boson sampling scheme, is what makes it a quantum experiment.

Through the last decade, additional applications of boson sampling have been suggested. Most of these will be considered in Chap. 6, except for the use of a boson sampling device as an interferometric sensor. This is a major contribution of our publication [26] to the field, and we will discuss it throughout in this thesis.

2.5.2 Original paradigm

More accurately, the scheme for boson sampling to prove quantum advantage goes as follows: Consider a network of coupled linear modes, as depicted in Fig. 2.6, where the two input modes μ and ν are initially excited. The possibility of measuring the excitation of modes ζ and γ as the output of a random walk in this network depends on the mutual coupling between modes, and is illustrated as "routes" (broken lines) within the network. If the connectivity is given by the matrix \mathcal{G} , the amplitude of the transition $|\mu, \nu\rangle \rightarrow |\gamma, \zeta\rangle$

$$A_{\mu, \nu}^{\gamma, \zeta} = \mathcal{G}_{\mu}^{\zeta} \mathcal{G}_{\nu}^{\gamma} + \mathcal{G}_{\mu}^{\gamma} \mathcal{G}_{\nu}^{\zeta}. \quad (2.42)$$

where the colors refer to the routes in Fig. 2.6. Here we left out normalization factors for simplicity (e.g. applying when the numbers of input and output modes differ, or when more than one excitation is allowed in each mode) [57].

The sum in Eq. (2.42) is the permanent, \mathcal{P} [58] of the matrix

$$\mathcal{G}_{\mu, \nu}^{\gamma, \zeta} = \begin{bmatrix} \mathcal{G}_{\mu}^{\zeta} & \mathcal{G}_{\nu}^{\zeta} \\ \mathcal{G}_{\mu}^{\gamma} & \mathcal{G}_{\nu}^{\gamma} \end{bmatrix}$$

The sharp eye will notice that this is in fact a submatrix of the large \mathcal{G} , including only the elements relevant for the possible transmissions. Formally, one must choose the columns corresponding to the input modes and the rows corresponding to the output, whose probability we are interested in emulating. If three modes were excited, the size of the submatrix would become 3×3 , and in general its size grows quickly. Here the complexity enters the stage.

Calculating \mathcal{P} and verifying the results are exponentially hard tasks (growing with the size of the submatrix), when equipped with only classical computers. Despite the existence of a few algorithms by e.g. Ryser [59], R-NW [60], and Zheng [61], finding \mathcal{P} is more time-consuming than the more commonly known

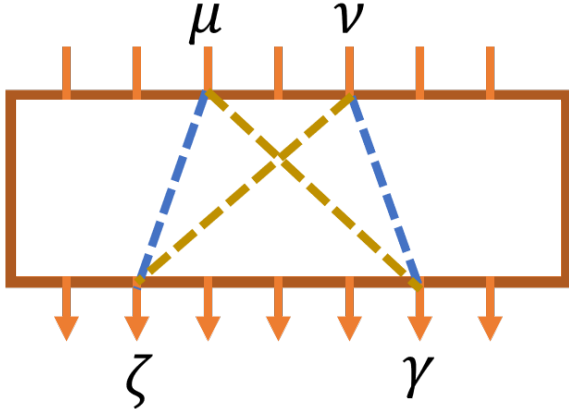


Figure 2.6: The original boson sampling paradigm considers the possible physical or virtual routes (here depicted by broken lines) taken by excitations through an optical network. In this figure, we show the input mode $|\varphi\rangle_{in} = |0\rangle_1 \otimes |0\rangle_2 \cdots |1\rangle_\mu \cdots |1\rangle_\nu \cdots$. Given this input, the output mode $|\varphi\rangle_{out} = |0\rangle_1 \otimes |0\rangle_2 \cdots |1\rangle_\zeta \cdots |1\rangle_\gamma \cdots$ can occur either by the transition $[\mu \rightarrow \zeta, \nu \rightarrow \gamma]$ or by $[\mu \rightarrow \gamma, \nu \rightarrow \zeta]$. Only the matrix elements with these transition amplitudes are important for computing the output probabilities.

determinant, which can be computed in polynomial time and belongs to the computational class \mathcal{P} . Sampling fermions requires the determinant, a problem which is known to be efficiently calculated classically [62]. Boson sampling, on the other hand, is believed to belong to the complexity class $\#\mathcal{P}$ [2]. We elaborate further on the difference between the determinant and the permanent (in terms of the computational hardness) in Appendix A.

Hence the emulation by bosons in a network like that just described offers an exciting opportunity to prove the powerful capabilities of quantum computation. Given the introduction of N indistinguishable bosons into N out of M modes, the evolution of the bosonic states will be determined by the couplings between all M modes, as expressed in the Hamiltonian:

$$\mathcal{H} = \hbar \sum_{i,j} \mathcal{G}_{i,j} a_i^\dagger a_j \quad (2.43)$$

where $a_{i,j}^\dagger$ and $a_{i,j}$ are the ladder operators.

Even though indistinguishable, bosons interfere mutually [63]. Such an interaction has been described for a couple in the famous Hong-Ou-Mandel experiment [1], and generalized in the bosonic birthday paradox [64], which has even been demonstrated experimentally [65] (we will revisit these effects in Chap. 5). This means that unless $M \gg N$, we can hardly avoid that the expectation value of the bosonic population in at least some mode will exceed unity (at least momentarily). This is one of the reasons for the formulation of new boson sampling schemes.

2.5.3 Alternative schemes

From around 2014 other variations of boson sampling have been proposed and implemented, e.g. scattershot boson sampling [66], gaussian boson sampling [67, 68], and driven boson sampling²⁵ [69]. These include random or squeezed

²⁵Ref. [69] defines driven boson sampling as a scheme of itself, while some other papers relate to it as a sub-version of gaussian boson sampling.

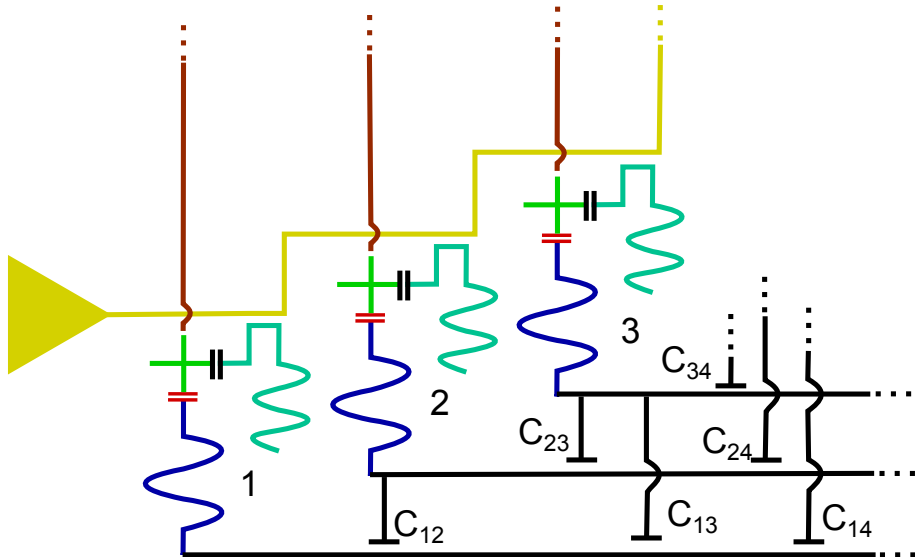


Figure 2.7: Suggested schematic of a superconducting chip for implementing microwave boson sampling. The resonators are loaded from qubits (here represented as the light green schematic Xmons). The qubit state is dispersively measured by a global transmission line (yellow) from readout resonators (magenta), when qubits are brought back into resonance with their respective quantum bus resonators (blue). These are capacitively coupled to each other (black waveguides) with capacitance C_{ij} , and this graph is made possible by air-bridges or dielectric cross-overs effectively coupling the lines.

states as the input, and the classically hard-to-compute functions are in some cases the hafnian rather than the permanent [70]. The general idea remains the same; what is hard (= time consuming) to calculate classically can quickly be emulated by quantum algorithms²⁶.

2.5.4 Microwave Implementation

The original proposal of boson sampling from Ref. [2] involves generating single bosons, i.e. Fock states and loading these into a network of modes [74]. Also the "output" modes to be sampled are Fock states, and this is the scheme our numerical simulation studies. Conveniently, qubits can be used both to generate the Fock states and for the readout stage as described below. And the network of coupled modes can be realized by coplanar standing wave resonators, like those we studied in Sec. 2.1. In the following, we refer to resonators belonging to the network as "quantum buses", unlike resonators solely used for dispersive readout (and accordingly named "readout resonators").

The operations to be repeated multiple times to sample the boson distribution includes the following few steps:

1. Exciting the qubits into the $|1\rangle$ -state.
2. Tuning the qubits into resonance with their coupled quantum buses.

²⁶Besides the family of sampling problems, there are many other computational tasks in which quantum devices are expected to be more efficient than classical computers. The most outstanding of these is that of simulating multi-particle systems, where the Hilbert state is very large. It is thus appealing to employ a quantum system with its implicit quantum behaviour (e.g. mutual entanglement between particles, superposition of states, etc.) to mimic another quantum system [71]. Other examples are the study of optical lattices [72] and Rydberg atoms [73].

3. Allowing sufficient time to reach a "rich" distribution, i.e. many nontrivial density matrix elements.
4. Detecting occupation of quantum buses by dispersive readout.

We have already described the operation of qubits in Sec. 2.3.2. To allow global couplings (as opposed to nearest-neighbor couplings only), either dielectric cross-overs or standing bridges are necessary for waveguides to pass each other (Fig. 2.1(b), Ref. [36], and Appendix B)²⁷.

The dispersive readout method was discussed in Sec. 2.4.3, including both readout resonators and a common transmission line. The latter allows the simultaneous measurement of the states of all qubits, given that the readout resonators have different frequencies²⁸; this is multiplexed readout.

Fig. 2.7 (originally published in Ref. [26]) suggests the schematic layout of a SC microwave boson sampling chip. It consists of a number of identical unit cells, each centered around a qubit with multiple connections. The actual experiment of interest takes place in the network of waveguides, linked to the qubits through quantum buses (in some papers also referred to as "quantum walk resonators").

Each qubit is also coupled to XY-probes (named so due to their operations on the Bloch sphere), allowing the excitation of the individual qubit, to Z-controls through SQUIDs, enabling tuning of the qubit as necessary for the operational scheme shown above, and to readout resonators. Importantly, the latter must be slightly different in length for each qubit, to ensure that readout frequencies are different.

²⁷As briefly mentioned above, SC qubits can be coupled in numerous ways: By mutual capacitance and/or mutual inductance; constant or tunable [75], etc.

²⁸The dispersive shift changes the qubit's energy level and thus the energy of the photons in the qubit. Since each readout resonator has a different resonance, the quantum walk resonators can be thought of as distinguishable at the readout stage, but this is subsequent to the quantum walk. Their mutual interference is thus expected to occur, when they are still indistinguishable.

CHAPTER 3

Background II: Kinetic Inductance and Parametric Amplification

The last chapter reviewed the powerful properties of superconducting circuits in the framework of quantum dynamics. In particular, we saw how the nonlinear inductance of the Josephson Junction is the key to nonlinear resonators that effectively serve as qubits.

Nonlinearity is, however, also a key ingredient for travelling-wave parametric amplifiers. In this kind of device, the power of a signal at some frequency ω_s is increased by so-called "wave-mixing" with a pump at frequency ω_p , an interaction relying on the nonlinearity of the amplifier in complete analogy with the nonlinear (χ^2) crystals commonly known in optics [76].

This chapter introduces another source of nonlinearity: The kinetic inductance of certain superconducting materials. We will see why choosing microstrip traces are preferred over CPW, and how the coupled mode equations predict the wave-mixing, later to be observed experimentally Chap. 5.

3.1 Kinetic Inductance

Inductance is essentially electromagnetic inertia, parallel to what Newton observed in mechanics. When a force is applied to an object it accelerates, and the acceleration is proportional to its mass. In electrodynamics, a conductor experiences an increasing current, I when a voltage, V is applied, and the proportion between V and dI/dt , referred to as inductance, L , is most often discussed in terms of the magnetic field created around the conductor (as explained by Maxwell's equations). In this context, the inductance expresses the energy (or energy density) of the magnetic field:

$$U_B = \frac{1}{2} \int_0^T \int_0^I V dI dt = \frac{1}{2} \int_0^T \int_0^I L \frac{dI}{dt} dI dt \quad (3.1)$$

and when L is independent of the current, Eq. (3.1) becomes: $U_B = \frac{1}{2} LI^2$.

But inducing a current does not only create a magnetic field with the associated magnetic energy. It also implies accelerating charged particles, a process which requires additional *kinetic* energy. To quantify this, we can imagine a superconductor of cross-section A and length l . The density of Cooper pairs n_s equals half the density of electrons n_e . When denoting the pairs' mass $2m_e$, and their velocity v_s , we get the total kinetic energy, E_k to be that of a single pair times the number of pairs:

$$E_k = \frac{1}{2} 2m_e v_s^2 \cdot \frac{n_e}{2} Al \quad (3.2)$$

The current is by definition $I = qn_s Av_s = 2e \frac{n_e}{2} Av_s = en_e Av_s$, where $q = 2e$ is the charge of a Cooper pair, and e the elementary charge. Thus, by defining

$$L_{kin} \equiv \frac{1}{2} \frac{m_e l}{n_s e^2 A} = \frac{\mu_0 \lambda_L^2}{A} \cdot l$$

where λ_L is the London penetration depth of Eq. (2.14), we can re-write Eq. (3.2) as

$$E_k = \frac{1}{2} L_{kin} I^2 \quad (3.3)$$

The "magnetic" inductance L of Eq. (3.1), hereafter referred to as *the geometric inductance*, L_g is usually orders of magnitude larger than L_{kin} , and E_k can be neglected. But in certain superconductors, where the v_s becomes relatively high compared to other materials (and the value of $n_s A$ decreases), L_{kin} becomes significant²⁹. The *kinetic inductance ratio*,

$$\alpha = \frac{L_{kin}}{L_g + L_{kin}} \quad (3.4)$$

²⁹Kinetic inductance is also of importance for plasmonics [77].

is a central figure in the work with kinetic inductance materials and will become important, when we discuss nonlinear wave-mixing.

In some publications and theses the theoretical derivation of α , L_{kin} , and more interestingly, the dependence on external parameters such as current and temperature, include the surface inductance, and a geometrical factor g that can be calculated by numerical models. But in this work we will limit ourselves to case of very thin films, where the thickness h of the kinetic inductance material is a few nm, $< \lambda_L/50$. In this regime, α indeed reduces to Eq. (3.4) (given that the factor g is close to unity) [32].

3.2 Tungsten-Silicide Micro-strips

A relatively unexplored high-kinetic inductance material is W_xSi_{1-x} , tungsten-silicide. From here on onwards, we will abandon the stoichiometric notation, but it is worth noting that as an amorphous material the relation between tungsten and silicon determines λ_L and as a direct outcome also L_{kin} . In our fabrication recipes, we achieve values of α close to unity (i.e. $L_{kin} \gg L_g$). This in itself creates interesting research perspectives, but even more exciting is the fact that L_{kin} of WSi also turns out to be non-linear³⁰.

The inductance per unit length, $L_{kin,l} = L_{kin}/l$, can be written as [3,32]

$$L_{kin,l} = \frac{\mu_0 \lambda_L^2}{A} \left(1 + \left(\frac{I}{I_*} \right)^2 \right) \equiv L_0 \left(1 + \left(\frac{I}{I_*} \right)^2 \right) \quad (3.5)$$

where we used the definition of λ_L from Sec. 2.3.1. In Eq. (3.5), I_* is the characteristic current scale of nonlinearity and is of the order of I_c . We will return to the subject of nonlinearity in Sec. 3.3. For now, it will suffice to consider the coefficient outside the brackets in Eq. (3.5). According to this, $L_{kin,l}$ reaches orders of 15-60 μH , given the typical values $\lambda_L \sim 0.5\text{-}1 \mu\text{m}$ for transmission lines of WSi alloys³¹ that are a few μm wide and $\sim 10 \text{ nm}$ thick [78].

Our WSi circuits are based on microstrip geometry, rather than the CPW of the former chapter. This affects the characteristic impedance Z_l and the phase velocity v_{ph} , and introduces dielectric loss in parallel to the transmission line.

3.2.1 Impedance Matching in High Inductance Circuits

The characteristic impedance of a lossless superconducting transmission lines is, as already mentioned, $Z_0 = \sqrt{L_l/C_l}$, where L_l and C_l are the inductance and capacitance per unit length.

In Sec. 2.1.1 we discussed the importance of matching Z_L to 50Ω . Typical CPW traces, such as those in Figs. 2.1(b) and 2.2(d), can be prepared by means of optical

³⁰See Appendix A for a derivation of the source of nonlinearity.

³¹The stoichiometric relation determines the exact value of λ_L and can in principle be controlled in the fabrication process, as we shall see in Chap. 4.

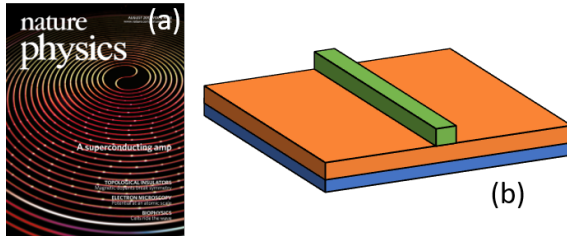


Figure 3.1: (a) Front page of *Nature Physics*, Vol. 8, 2012, celebrating the CPW amplifier of Ref. [3], approximately 1 m long. This implementation also includes extend tapers to match Z of the surrounding electronics with Z of the amplifier. (b) Microstrip geometry (distorted dimensions) with green signal trace, orange dielectric material and blue ground to be compared to Fig. 2.1(a).

lithography, and in Table 3.1 we compare the characteristic geometric and electrical values for traces fabricated in our lab, where the CPW are of aluminum. When preparing 50Ω matched waveguides with this material, L_{kin} is mostly negligible³², and α is much smaller than in WSi.

In Chap. 4 we will consider the practical limitations of fabrication in detail, including those of exact impedance matching. Reaching 50Ω is nearly impossible in conventional³³ CPW of materials where $\alpha \lesssim 1$. In designs, where $Z_l \gg 50\Omega$, extended adiabatic tapers³⁴ are therefore required to suppress reflections and ringing in the transmission spectrum [79].

An immediate solution emerges when replacing the CPW geometry with microstrips (Fig. 3.1(b)). In microstrips the traces are separated from the ground plane by a dielectric layer, and the thickness, t of the latter can be as narrow as a few nm. This (for SC circuits) rather novel approach allows for direct engineering of C_l , in this case simply the capacitance of a plate capacitor, i.e. $C_l = \epsilon_d \frac{w}{t}$, where $\epsilon_d = \epsilon_0 \epsilon_r$ is the dielectric permittivity and w the trace width. In turn, we can now also design Z_0 to match Z_L . This alone is a major innovation, but the control of C_l has a more profound implication: It can be used to slow down the phase velocity.

Characteristic values of transmission lines			
Al CPW		WSi microstrips	
Al thickness	100 nm	WSi thickness	~ 10 nm
Trace width	8 μm	Trace width	3 μm
Gap to ground	5 μm	Dielectric layer	30 nm
L_l	0.5 $\mu\text{H/m}$	L_l	50 $\mu\text{H/m}$
C_l	0.2 nF/m	C_l	20 nF/m
v_{ph}	$\sim 10^8$ m/s	v_{ph}	$\sim 10^6$ m/s

Table 3.1: Characteristic values of Al CPW and WSi microstrip traces as implemented in our lab with impedance matching (i.e. $Z_l = 50 \Omega$) in both cases. The practical limitations of fabrications are described in Chap. 4. Numbers in this table refer to theoretical values according, cf. Eqs. (3.5)-(3.6).

³² L_{kin} is both geometry and material dependent. For waveguides with identical geometries, L_{kin} is lower for Al than for WSi, so impedance matching can only be achieved with different dimensions, and for Al CPW with the sizes of Table 3.1, the geometric inductance is dominant. An exception is for experiments with extremely high powers, where the nonlinearity of L_{kin} , even in Al, become apparent.

³³Impedance matching can be achieved with a fractal structure in the design [4], but this structure is sensitive to fabrication errors and spurious ground plane resonances, requiring wire bonds across the trace.

³⁴The length of the tapers depend on the impedance of the trace. For $Z \sim 500 \Omega$, a few mm are needed, and this makes the transmission line even longer and sensitive to magnetic flux noise.

3.2.2 Decreasing phase velocities

The phase velocity, $v_{ph} = c/n$, where c is the speed of light in vacuum and n the refractive index, expresses the speed with which a CW propagates through media. For electromagnetic waves transmitted through transmission lines [34, 80],

$$v_{ph} = \frac{1}{\sqrt{C_l L_l}} \quad (3.6)$$

One can also think of Eq. (3.6) as the velocity of the transmitted photons passing through the transmission line. Its importance in the field of wave dynamics is manifested in the wave equation, here expressed in terms of the current³⁵:

$$\frac{\partial^2 I}{\partial x^2} = \frac{\partial}{\partial t} \left(L_l(I) C_l \frac{\partial I}{\partial t} \right) \quad (3.7)$$

Considering the nonlinearity of L_l (as indicated in Table 3.1), the solution(s) to Eq. (3.7) is far from trivial. It is presented below, but at this point two remarks can already be made: First, as both C_l and L_l are two orders of magnitude larger in our WSi microstrips than in the CPW of Al, v_{ph} becomes two orders of magnitude *smaller* in the former than its value in the latter. This implies that photons spend more time travelling through our WSi microstrips [81]. Second, the nonlinearity of Eq. (3.7) itself is the feature that allows wave-mixing.

3.2.3 Dielectric Loss

Dielectric materials are known as a source of loss, and this troublesome effect can be modelled as energy-absorbing "parasitic" TLS's [6, 82]. Consequently, the integration of dielectric materials in our devices results in a loss coefficient:

$$\Gamma_p = \frac{2\pi f_p}{v_{ph}} \frac{1}{2} \frac{\tan\delta_0}{\sqrt{(1 + \Omega_R^2 T_1 T_2)}} \quad (3.8)$$

where Ω_R is the Rabi frequency in the standard TLS model³⁶, $\tan\delta_0$ is the loss tangent (without saturation effects), and T_1 and T_2 are the decay and dephasing times of the TLSs [6, 34]. We defined Ω_R already in Sec. 2.4. Here it arises from the coupling of the TLSs to the field, and assumes a dipole moment of $d = 1$ D. T_1 and T_2 in the standard TLS model are formally defined as [84]:

$$\frac{1}{T_1} = \frac{2}{T_2} = A \frac{(\Delta_0 \hbar \omega)^2}{k_b^3} \coth \left(\frac{\hbar \omega}{2k_B T} \right)$$

³⁵Alternative to the model of transmitted photons, the wave equation describes the transmission of current and voltage.

³⁶The standard TLS model assumes an ensemble of TLSs, each modelled as two potential wells. At low temperatures (~ 20 mK) the excitation, i.e. transition between the states is mainly by tunneling through the barrier separating the wells [83].

where ω is the TLS's angular frequency, Δ_0 its tunneling amplitude, which together with the asymmetric energy Δ defines the eigenenergy $\hbar\omega = \sqrt{\Delta^2 + \Delta_0^2}$, and $A \sim 10^8 s^{-1} K^{-3}$ [6, 82, 83]. These parameters vary between the TLSs, and in our simulations of Eq. (3.8), we use the value $T_1 T_2 = 10^{-14} s^2$, i.e. both time scales are assumed to be in the order of 100 ns. As we will see later, this ansatz produces simulations which largely agrees with our empirical observations.

At high pump powers the TLSs become saturated, and the energy absorption decreases. The square-root in Eq. (3.8) accounts for absorption of a strong CW (hereafter the "pump") at frequency f_p , not only by TLSs at the same frequency, but also those slightly detuned by $\delta f = f_p - f_{TLS}$. In two-tone measurements, involving a pump and a weaker signal at $f_s \neq f_p$, we assume that saturation effects are mainly caused by the pump, and that the absorption of the signal tone is linear. The loss at f_s is thus a function of the probability that TLSs at $f_{TLS} = f_s$ are excited by the signal itself rather than the pump. We approximate this probability by the saturation parameter s of TLSs at f_s , when the pump is at f_p [50]:

$$s = \frac{\Omega_{Rp}^2 T_1 T_2}{1 + (\delta f)^2 T_2^2} \quad (3.9)$$

where Ω_{Rp} is the Rabi frequency of the pump, and *not* of the dielectric material's TLS's as in Eq. (3.8). The excited population ρ_{ee} of the TLSs due to the pump is then

$$\rho_{ee} = \frac{s}{2(1 + s)} \quad (3.10)$$

Thus we write both for the signal and the idler a pump dependent decay constant:

$$\Gamma_{s,i} = \Gamma_{s,i}^0 (1 - 2\rho_{ee}) \quad (3.11)$$

where

$$\Gamma_{s,i}^0 = \frac{1}{2} \frac{2\pi f_{s,i}}{v_{ph}} \tan \delta_0 \quad (3.12)$$

is the linear decay constant, referring to the linear loss of the signal (idler) only, as if no pump were present.

Summarizing this subsection: We assume that the dielectric TLS loss by the signal is linear, but since the pump also saturates TLS's *at the signal frequency* (detuned from the pump frequency), the energy absorption of the signal becomes nonlinear.

The numerical value of $\tan \delta_0$ depends on the material, a point we will consider further in Chap. 4.

3.3 Wave-Mixing and Amplification

We solve Eq. (3.7) by the ansatz

$$I(z, t) = \frac{1}{2} \sum_n \left(A_n(z) e^{i(k_n z - \omega_n t)} + c.c. \right) \quad (3.13)$$

where k_n is the wavenumber, and $\omega_n = 2\pi f_n$ [3,85]. This expression can in principle include an unlimited number of modes n , but we limit the discussion to degenerate four wave-mixing. In this process we follow the evolution of the three modes: The signal (who should be amplified), a pump (several orders of magnitude stronger than the signal), and an idler, which we will denote $n = s, p, i$ respectively. Energy conservation requires that $2 \cdot \omega_p = \omega_s + \omega_i$. This also holds for non-degenerate four wave-mixing³⁷.

3.3.1 The Coupled Mode Equations

We will adopt the "slowly varying envelope" approximation, stating that the complex amplitudes $A_n(z)$ do not change nearly as fast as the exponent [3]:

$$\left| \frac{\partial^2 A_n}{\partial z^2} \right| \ll \left| k_n \frac{\partial A_n}{\partial z} \right| \quad (3.14)$$

Moreover, following the so-called "coupled-mode" analysis (described in detail in Appendix A), and with Eq. (3.14) we arrive at the three coupled-mode equations [85] governing the dynamics of the transmission:

$$\frac{\partial A_p}{\partial z} = \frac{i k_p \alpha}{2 I_*^2} \left(|A_p|^2 A_p + 2 |A_s|^2 A_p + 2 |A_i|^2 A_p + 2 A_s A_i A_p^* e^{i \kappa z} \right) \quad (3.15a)$$

$$\frac{\partial A_s}{\partial z} = \frac{i k_s \alpha}{2 I_*^2} \left(|A_s|^2 A_s + 2 |A_i|^2 A_s + 2 |A_p|^2 A_s + A_i^* A_p^2 e^{-i \kappa z} \right) \quad (3.15b)$$

$$\frac{\partial A_i}{\partial z} = \frac{i k_i \alpha}{2 I_*^2} \left(|A_i|^2 A_i + 2 |A_s|^2 A_i + 2 |A_p|^2 A_i + A_s^* A_p^2 e^{-i \kappa z} \right) \quad (3.15c)$$

where we defined $\kappa = k_s + k_i - 2k_p$. Eqs. (3.15) can be further simplified, under the assumptions that

- $\kappa \sim 0$ (our modus operandi will be clear in Chap. 4)
- $\alpha \lesssim 1$
- that we apply a strong pump, i.e. $|A_p| \gg |A_s|, |A_i|$

³⁷In this process $\omega_{p1} + \omega_{p2} = \omega_s + \omega_i$, i.e. with two pump tones p_1 and p_2 at different frequencies.

If all these conditions exists, the equations simplify radically:

$$\frac{\partial A_p}{\partial z} = \frac{ik_p\alpha}{2I_\star^2}|A_p|^2 A_p \quad (3.16a)$$

$$\frac{\partial A_s}{\partial z} = \frac{ik_s\alpha}{2I_\star^2} \left(2|A_p|^2 A_s + A_i^* A_p^2 e^{-i\kappa z} \right) \quad (3.16b)$$

$$\frac{\partial A_i}{\partial z} = \frac{ik_i\alpha}{2I_\star^2} \left(2|A_p|^2 A_i + A_s^* A_p^2 e^{-i\kappa z} \right) \quad (3.16c)$$

The solution for A_p is immediately found analytically, as its propagation is independent of the signal and the idler:

$$A_p(z) = A_p(0) \cdot \exp\left(\frac{ik_p\alpha|A_p(0)|^2 z}{2I_\star^2}\right) \quad (3.17)$$

By denoting the nonlinear phase shift $\phi = k_p\alpha|A_p(0)|^2/(2I_\star^2)z$, Eq. (3.17) simply becomes $A_p(z) = A_p(0)e^{i\phi}$. In nonlinear optics, ϕ is typically referred to as the *self phase modulation*.

3.3.2 Amplification metrics

It is natural to define the the *signal power gain*:

$$G_s = \frac{|A_s(z)|^2}{|A_s(0)|^2} = \frac{|I_s(z)|^2}{|I_s(0)|^2} \quad (3.18)$$

i.e. the ratio between the output and the input signal power (or, equivalently, the squares of the current amplitudes). In the linear amplification regime, $G_s = 1 + \phi^2$ [5]. This emphasizes the importance of a large kinetic inductance fraction α , a low critical current (in the order of I_\star), and a strong pump $|A_p(0)|$.

An additional coefficient, important as a witness of the wave-mixing occurring in the amplifier, is the idler conversion efficiency. Following Ref. [3], we will define this

$$\tilde{G}_i = G_s - 1 \quad (3.19)$$

If $G_s \geq 1$ (see further reflections on this assumption below), the definition of \tilde{G}_i should be considered in light of Eqs. (3.16) and the conservation of energy. The generation of signal photons takes place, while an equal number of idler photons are created. The rise of an idler is therefore not only a proof of the wave-mixing, but also an alternative measure of the amplification.

Finally, we address the assumption that $G_s \geq 1$. In the definition of Eq. (3.18) the possibility of loss, scattering, and reflections in the amplifier are not expressed. When operated for the sole purpose of amplification, all that matters is the ratio

between output and input, but from a scientific viewpoint we want to understand the dynamics of amplifier. In the optics of a research and development, a strong amplification factor with significant losses is much better than a weak, lossless amplifier. The former can perhaps be improved, if losses are limited, unlike the latter. For this reason, we prefer using *the pump amplification factor*

$$G_p = \frac{|I_s(z)^{\text{pump}}|^2}{|I_s(z)^{\text{no-pump}}|^2} \quad (3.20)$$

rather than G_s . This is the ratio between the amplifier's output signal power, measured *with* pump and *without* it.

CHAPTER 4

Methodology

In all research, whether in natural science, humanities or any other field, the documentation of the applied methods is considered a fundamental must in reports and publications. Results are worthless, if the research cannot account for their acquisition.

In this spirit, the following pages describe both the methods of simulation, the fabrication of devices, and the experimental setups. Despite the modest volume dedicated to this topic in the thesis, more than 80% of the research was assigned to coding in Matlab, development of fabrication recipes, and calibration of equipment.

A clear distinction is made between simulative *tools* and simulative *results*. The former is presented in this chapter as e.g. relevant equations, adapted or re-written for the numerics, and techniques for efficient compilation. Results of the simulations appear in Chap. 5, and there, when available, they are compared to empirical data.

4.1 Simulation Techniques

Simulations are an integrated part of experimental physics. They are used not only to predict the behaviour and feasibility of experiments, but can even serve to verify results, or explain experimental deviations from otherwise reliable theory.

In this work we used simulations in Matlab for several purposes: First we describe the behaviour the proposed microwave boson sampler, and next we simulate the various kinetic inductance circuits later implemented experimentally.

4.1.1 Boson Sampling with the Bose-Hubbard Model

It can be quite time-consuming to simulate a large quantum system on an ordinary desktop. First, because quantum systems are best simulated by other quantum systems, and second, because of the quite large computational resources required solve problems with large Hilbert spaces³⁸.

SETTING UP THE SYSTEM The core of the simulation is the "graph" G (a coupling matrix corresponding to \mathcal{G} in Sec. 2.5.2) of couplings between the M modes. The energies of the couplings are randomly generated according to a uniform distribution in a bandwidth of ~ 100 MHz. The couplings are symmetrical, so to save space, only the elements in the triangle below the diagonal of the coupling matrix are saved, and the remaining matrix elements are zeros.

The simulation does not include any sources; photons may be lost during iterations with decoherence³⁹, but under no circumstances are they created after the initialization. For this reason, the initial number of photons (excitations) N determines the number of possible quantum states⁴⁰:

$$S_N = \binom{N + M}{M} = \binom{N + M}{N}$$

Bosonic annihilation operators \hat{b}_m are mode-independent and implemented as off-diagonal terms in $S_N \times S_N$ matrices, removing photons from one mode, and making them re-appear elsewhere (or simply removing the photons, when decoherence is simulated). Raising operators b_m^\dagger (associated with creation of photons) are the Hermitian conjugate of \hat{b}_m , and the density matrix is initialized

³⁸Papers claiming quantum computational advantage, e.g. Refs. [8, 16] usually compare to the world's strongest supercomputers and not personal computers.

³⁹To estimate the effect of decoherence, some iterations are run with $T_1, T_\varphi \rightarrow \infty$.

⁴⁰One can easily reach this results with the so-called "bars and stars" method known from discreet math. If modes are bars (|) and excitations are stars (*), we place the stars between bars on a row, and consider each star (excitation) as belonging to the bar (modes) to its left, e.g. ||*||**|| represents the state $|1, 0, 2, 0, 0\rangle$. There are N stars to be placed and all together $M + N$ items, so the problem is solved by the binomial function.

as $\hat{\rho} = \vec{Y} \times \vec{Y}^*$, where \vec{Y} is the initial state, e.g.

$$\vec{Y} = \prod_k^{S_N-1} \left(|0\rangle_k \right) \otimes |1\rangle_i$$

Here $|x\rangle_k$ represents the occupation of the k 'th state, not the state of the physical mode (the latter materialized as a CPW resonator).

Multiplication of \hat{b}_m and \hat{b}_m^\dagger with unity operators provides us with global creation and annihilation operators $L_{i,j}$, where i and j are two coupled modes⁴¹. The system can now be described by the Bose Hubbard model [86], whose Hamiltonian is:

$$\mathcal{H}_{BH} = - \sum_{i,j} G_{i,j} \hat{b}_i^\dagger \hat{b}_j + \sum_i \frac{U_i}{2} \hat{b}_i^\dagger \hat{b}_i (\hat{b}_i^\dagger \hat{b}_i - 1) \quad (4.1)$$

neglecting mutual interactions between bosons. Whereas the first term in Eq. (4.1) describes the coupling, the second one relates to the occupation energy, and this might include nonlinearity. In practice $U_i = G_{i,i} = 0$ for all i modes in our simulations as an ideal network. In our script we replace the multiplications of ladder operators in Eq. (4.1) with $L_{i,j}$, but only for numerical reasons⁴².

Given the Hamiltonian, we now have the time propagator $\hat{P}_t = \exp(-i\mathcal{H}_{BS}dt)$ evolving the state over the infinitesimal time period dt . In Matlab, the function *expm* rather than *exp* must be used to find the matrix exponential rather than the exponents of the single matrix elements.

The density matrix at $t + dt$ is then

$$\hat{\rho}(t + dt) = \hat{P}_t \hat{\rho}(t) \hat{P}_t^\dagger \quad (4.2)$$

All matrices are sparse or "spalloc", a feature available in Matlab saving both space and time. However, the physics described so far is without decoherence effects and can actually be simulated without matrix multiplication. We could simply evolve the state vector, \vec{I} in time as $\vec{I}(t) = \hat{P}_t \vec{I}(0)$, since the coherent transformation is unitary. The trouble forcing us to use matrix multiplication and (allocating much more space for computation) begins, when including damping and dephasing in the simulation, and our quantum state becomes mixed.

KRAUS OPERATORS Decoherence (cf. Sec. 2.4.4) is a central component in the simulative study of boson sampling. Random processes cannot be exactly reproduced by a determinant script, but on average, i.e. with the decoherence times T_1 and T_φ

⁴¹In terms of syntax, it is important to distinguish between the ladder operators of an isolated TLS, which are 2×2 matrices on one hand, and the ladder operators of the TLS in a large network on the other, whose dimensions equal that of the larger system. We have not used specific symbols here to distinguish between these two operators, but emphasize that $L_{i,j}$ is the multiplication of the large \hat{b}_i that removes a photon from the i 'th mode and \hat{b}_j^\dagger that adds a photon in to the j 'th mode.

⁴²The density matrix is $S_N \times S_N$, and we cannot multiply this by a 2×2 operator without changing the Hilbert space.

we can imitate the system's behaviour. This is done with the Kraus operators E_k :

$$\sigma(t) = \sum_k E_k \rho_k E_k^\dagger \quad (4.3)$$

where $\sigma(t)$ is the density matrix *with* decoherence effects, and $\rho(t)$ - without.

Decoherence occurs in all multilevel systems coupled to the environment, and in general the operator describing amplitude damping is [87]:

$$E_k = \sum_k \sqrt{\binom{n}{k}} \sqrt{e^{(-\Delta t/T_1)(n-k)} (1 - e^{-\Delta t/T_1})^k} |n-k\rangle\langle n| \quad (4.4)$$

It is convenient to define $\gamma = 1 - e^{-\Delta t/T_1}$, which is the probability of loosing the excitation in the time interval Δt , and $|n\rangle$ is an eigenstate of the system [87]. Obviously, $\gamma \rightarrow 1$ for $\Delta t \rightarrow \infty$.

When dealing with TLSs such as qubits, Eq. (4.4) reduces to

$$E_0 = \begin{bmatrix} 1 & 0 \\ 0 & \sqrt{1-\gamma} \end{bmatrix}; \quad E_1 = \begin{bmatrix} 0 & \sqrt{\gamma} \\ 0 & 0 \end{bmatrix} \quad (4.5)$$

E_0 describes the lack of change, when the TLS is in the ground state and the decay of the excited state, while E_1 shows the *transition* from the latter to the former.

Unlike the Kraus operators for amplitude damping, dephasing does not involve transition between $|0\rangle$ and $|1\rangle$, i.e. there are no off-diagonal elements in the dephasing operators:

$$E_2 = \begin{bmatrix} 1 & 0 \\ 0 & \sqrt{1-\lambda} \end{bmatrix}; \quad E_3 = \begin{bmatrix} 0 & 1 \\ 0 & \sqrt{\lambda} \end{bmatrix} \quad (4.6)$$

where $\lambda = 1 - e^{-\Delta t/T_\varphi}$ is the probability for complete loss of information without the loss of energy (e.g. scattering of a photon in a waveguide). E_2 and E_3 are applied together, and they affect the phase of the matrix elements in the density matrix $\hat{\rho}$, but not the amplitude.

4.1.2 Simulation of the Microstrip Amplifier

Numerical simulations of the microstrip amplifier are based on Eqs. (3.16). By choosing sufficiently small Δz values⁴³, we get

$$A_{s,i}(z + dz) = A_{s,i}(z) + \Delta z \cdot \left(\frac{\partial A_{s,i}(z)}{\partial z} \right) \quad (4.7)$$

⁴³The results converge, when $\Delta z < 0.1$. The important parameter is the wavelength, which must be much large enough so that $\Delta z \cdot \partial A_{s,i}/\partial z \ll A_{s,i}$

for the signal and the idler, while the pump in principle can be solved analytically with Eq. (3.17).

These solutions, however, do not include loss. To make up for that, and following the derivations in Sec. 3.2.3, we add the decay constant Γ_p (from Eq. (3.8)) to the pump, i.e.

$$A_p(z + \Delta z) = A_p(z) + \left(\frac{\partial A_{s,i}(z)}{\partial z} - \Gamma_p \Delta z \right) \quad (4.8)$$

Here, the first term in the large brackets (marked in green) is the derivative as found from Eq. (3.16a) without loss effects.

4.1.3 Simulating Transmissions in Multimode Networks

The simulation of the transmission through travelling and standing waveguides is more complicated than a single multimode trace. Here we are especially interested in the eigenmodes of the system, **and** the intensity of their excitation (i.e. how strong do we couple to these modes).

To achieve a uniform model for simulation of all kinds of networks, we consider each segment of the networks (shown in Fig. 4.1) in terms of the voltage and the currents. In particular, for each segment n , either a $50\ \Omega$ -matched waveguide or a submicronic wire (marked by blue and orange respectively in Fig. 4.1), we search for the amplitudes V_0^\pm of Eqs. (2.3)

Practically, each intersection ("node") of waveguide and submicronic wire adds two Kirchoff equations cf. Eqs. (2.3), so depending on the number of intersections N , we are left with $2 \cdot N$ such equations with the same number of unknown variables.

In Appendix C we rigorously compute these circuit variables of the networks shown in Figs. 4.1(a)-(b), and how the solution can be discussed in light of the tight-binding model.

The lattice (Fig. 4.1(c)) is a bit more challenging. Here the current "directions" are rather arbitrary, as we deal with standing waves in a resonant structure rather than travelling waves in transmission lines. To solve this problem, we double the number of variables and equations to define *ingoing* and *outgoing* voltages with respect to each intersection, rather than to a globally defined direction.

At all nodes nano-wires meet the wider main traces. For e.g. the lattice of Fig. 4.1(c), nodes are the ends of resonators, i.e. are any point combining orange and blue lines on this figure. Edges on the other hand, we define as either main traces or nano-wires, in principle only distinguished by their impedances (distinguished and determined by different trace widths), Z_0 or Z_c , and lengths, L and d , for main traces/couplers respectively. For the q 'th node, we consider the voltage in the j 'th edge (of all J_q edges connected to this node). The edge voltage with

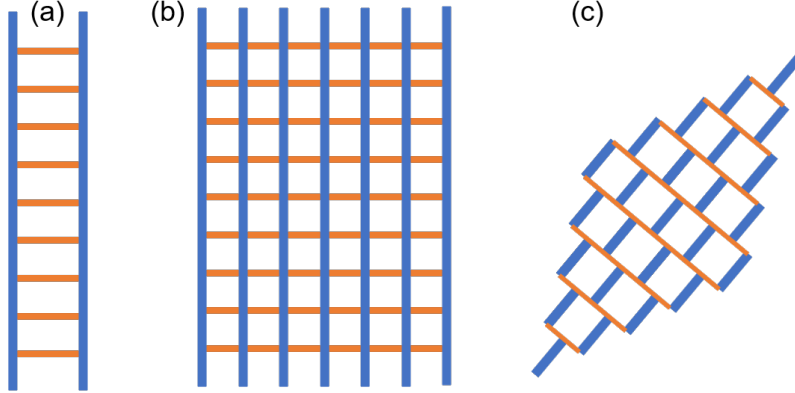


Figure 4.1: Schematic illustration of HKI networks as implemented experimentally. Blue: 50Ω -matched waveguides. Orange: Submicronic couplers (a) Two travelling microstrips coupled every $100 \mu m$. (b) A generalization with seven parallel microstrip traces with the same periodic nearest-neighbor coupling. (c) The two-dimensional square lattice of standing microwave resonators.

respect to the node then can be written in accordance with Eq. (2.3)(a):

$$V_q(x) = A_q^j e^{ik_j x} + B_q^j e^{-ik_j x} \quad (4.9)$$

where x denotes the distance from the q 'th node along the j 'th edge and k_j is the impedance and frequency dependent wave-number; A_q^j is voltage wave leaving the q 'th node on the j 'th edge, and B_q^j the voltage wave arriving at the same node on the same edge.

We solve for A_q^j and B_q^j for all the Q nodes' $J = \sum_q J_q$ connected edges, but the number of unknowns can be reduced by mapping the connectivity correctly:

$$A_{q_1}^j = B_{q_2}^j e^{ik_j \delta_j} \quad (4.10)$$

if the j 'th edge connects the nodes indexed q_1 and q_2 and has the length δ_j . The input and output nodes (injection and readout) constitute the boundary conditions. For all other nodes the lossless assumption requires that

$$\sum_{j=1}^{J_q} A_q^j = \sum_{j=1}^{J_q} B_q^j \quad (4.11)$$

We encode Eqs. (4.9)-(4.11) together with the boundary conditions in a matrix, \hat{M} , in which each row represents an equation, so that

$$\hat{M} \times \vec{V} = \vec{K} \quad (4.12)$$

where $\vec{V} = (A_1^1, B_1^1, A_1^2 \dots A_1^{J_q}, B_1^{J_q} \dots A_2^1, B_2^1 \dots A_Q^1, B_Q^1 \dots A_Q^{J_Q}, B_Q^{J_Q})$, i.e. the vector of unknowns. \vec{K} is a vector almost exclusively of zeros due to the nature of the equations, except for those regarding the boundary conditions.

4.2 Nano-fabrication

Cleanroom fabrication is an art of itself, covering many scientific disciplines, such as wet chemistry, vacuum systems, material science, and semiconductor processing. Certain projects, after numerical simulations and theoretical planning, got stuck for weeks due to challenges at the fabrication stage. The single most important point of focus is the consistent uniformity of recipes. To ensure reproducibility, fabrication standards must be constant, or only changed carefully one by one to test the effect.

The technical details of the most important recipes appear in Appendix B, providing parameters such as spinning speeds, exposure doses, etc. Here, we review some aspects of central cleanroom processes.

4.2.1 Planning the circuit

Prior to designing a SC circuit, performance estimates must be done. As an example, when planning to produce readout resonators, the frequencies must be designed to fall within the detectable bandwidth and driving/pump resonances should be achievable⁴⁴. These requirements lead to constraints on L and C , cf. Sec. 2.1. And as we have already seen, also the need for impedance matching calls for careful engineering of the electrical properties).

In CPW, L_l and C_l can be estimated by the elliptic integral of the first kind [80]:

$$L_l = \frac{\mu_0}{4} \frac{K(k_1)}{K(k_2)} \quad (4.13a)$$

$$C_l = 4\epsilon_0 \epsilon_{eff} \frac{K(k_2)}{K(k_1)} \quad (4.13b)$$

where $k_1 = w/(w + s)$ and $k_2 = \sqrt{1 - k_1^2}$, and w and s are the trace width and the gap to the ground, respectively. Here we ignored L_{kin} , whose geometrical dependence appeared in Eq. (3.5), but in most circuits of e.g. Al, it is negligible. Interestingly, the thickness of the traces does not appear explicitly in Eqs. (4.13), but it does have a weak effect on ϵ_{eff} .

A useful rule of thumb prescribes that impedance matching of circuits on bulk Si substrates is achieved, when $s = 5/8 \times w$, i.e. 8 μm transmission lines must have 5 μm wide gaps to the ground plates on either side⁴⁵.

The only microstrips presented in this thesis are of HKI WSi, and computing L_{mag} in that geometry is therefore irrelevant. Here, L_{kin} is the all-dominating contributor to L_l , and C_l is found as the capacitance of a plate capacitor. For this

⁴⁴The technical limitations of frequencies are discussed in Sec. 4.5.

⁴⁵This is again under the assumption that $L_{mag} \gg L_{kin}$.

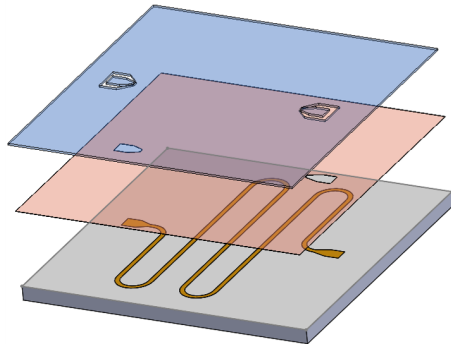


Figure 4.2: Breaking down the layers of fabrication in the microstrip parametric amplifier. Conceptual illustration (not in scale). The meandered trace is 11.6 cm long and fills a 6.2×6.2 cm² chip. Color code: Grey - bulk Si substrate (wafer). Orange - WSi strip. Red - amorphous Si (aSi) dielectric. Blue - Al ground. To ensure step coverage, each layer applied (in the order WSi, aSi, and Al) must be thicker than the former one.

reason, not all dielectrics allow impedance matching in micronic microstrips. This becomes clear when considering the layers of Fig. 4.2. Given the width w of the microstrip we have

$$C_l = \frac{w\epsilon_0\epsilon_r}{d} \quad (4.14)$$

where d is the thickness of the dielectric layer. This implies that for low permittivity materials (e.g. SiO₂), we have to keep d extremely very small to reach $Z = 50 \Omega$. But d must be at least some 20% larger than h , the metal (WSi) height to ensure step coverage. And lowering h is not a solution. This would only increase L_l further according to Eq. (3.5), raising the requested value C_l even further.

4.2.2 Material deposition

Two different methods were employed in this research for depositing materials: Sputtering and evaporation.

SPUTTERING When charged ions are accelerated by an electrical field to bombard a target, the latter releases its particles and these are deposited on the substrate wafer (in our case Si wafers). Typically an Ar⁺ plasma is used, since Ar is a noble gas, and does not react chemically with the target. Al thin films produced by sputtering are very uniform compared to evaporated films of the same material (the latter tends to appear "grainy" on SEM images). However, substrates with photoresist are banned (at least in our lab) from the sputtering system to avoid its

Electrical and SC properties				
Material	Permittivity ϵ_r	Deposition method	λ_L [nm]	$\tan \delta$
Al	-	Sput. or evap.	16	-
WSi	-	Sputtering	500-600	-
aSi	11.7	Evaporation	-	5×10^{-4}
SiO ₂	3.4	Evaporation	-	$2-3 \times 10^{-2}$

Table 4.1: Properties of four materials employed in the experimental devices mentioned in the thesis. The high λ_L of WSi makes the kinetic inductance dominating for this material, but it can still be observed for Al. Note that ϵ_r of aSi depends on the crystallinity, which is partly determined by the rate of evaporation.

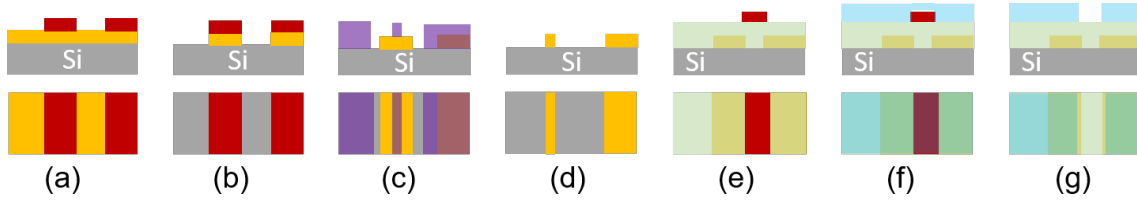


Figure 4.3: Example of fabrication flow: The preparation of the WSi microstrips, e.g. of Fig. 4.2. Steps illustrated with disproportional dimensions to enhance readability. Upper row: Cross-section, bottom row: Top view. (a) On the $300\mu\text{m}$ thick Si substrate (grey), 10nm WSi (yellow) is sputtered and a protective photoresist mask (red) is applied. (b) Wet-etch removes the vast majority of WSi, leaving main traces and intended couplers with similar widths. (c) An additional lithographic step is performed with PMMA (purple), stripped only at windows on either side of the couplers. (d) Wet-etch narrows down the coupler widths, while main traces are untouched. (e) The dielectric layer (partly transparent green) is evaporated unto the sample, and a new protective photoresist mask (red) is patterned. For this and the following step we display a different part of the device: Around the launcher and far away from the couplers (note that the "Si" tag is translated). (f) Evaporation of Al (transparent blue) covers the wafer. This layer is, unlike the dielectric amorphous Si, in reality opaque. (g) After lift-off in NMP and sonication, the device's top ground plane is isolated from the launchers. The intentionally shown slight misalignment, which unavoidably arises from optical lithography, causes only very short discontinuities without $Z = 50\Omega$

contamination.

WSi was deposited by sputtering at low powers. Initially, we "cracked" a target by bombardment with Ar^+ at too high current. After calibration, the low power meant that thin film growth rate of WSi was $\sim 10 \text{ nm/min}$, whereas, to compare, the Al was grown at $\sim 2 \text{ nm/sec}$.

EVAPORATION Evaporation is an appealing alternative to sputtering. Instead of letting particles intersect their intended substrate with high velocities after bombarding with accelerated ions, we place the material in a crucible and heat it⁴⁶. Eventually the material's temperature exceeds its boiling temperature and it evaporates. The vacuum chamber is filled with the desired thin film's material in its gaseous state, and a layer grows by adsorption on the substrate.

4.2.3 Lithography

Prior to patterning the actual layers of material (waveguides, junctions, capacitors, and all other features), traces and features are defined in resists⁴⁷. These are, as the name hints, resistive, and thus protective to later processing and serves as masks, later to be disposed. In electronic lithography, special e-resists are used, sensitive to electron beams, and optical resists, sensitive to light at $\sim 400 \text{ nm}$ wavelengths, are used for laser-lithography. In either case the devices with their resists are exposed to radiation according to pre-determined designs (CAD-files), and exposed areas of the resist are removed by developers. The pattern now appears in the resist-mask, but the material is still a uniform film.

⁴⁶Through this research, two heating methods were implemented: Thermal evaporation and e-beam evaporation. In the former, heat is applied to the crucible, and in the latter, the material is bombarded with accelerated electrons to heat it directly. E-beam evaporation was by far more successful than thermal evaporation. The latter often failed as the crucible overheated and cracked during processing.

⁴⁷Lithography is Greek for "stone writing" and was applied already in the 17th century for artworks and navigation maps. In modern nanotechnology it is the standard method for defining patterns in sacrificial masks, and then mirroring these patterns into the materials.

4.2.4 Patterning

WET-ETCH One way of using the lithographically defined mask is indeed as protection. In this case, the wafer (at this stage covered uniformly with the film of the material to be patterned, and with a partly open mask, as in Fig. 4.3(a)) can be dispensed in an etching solution (basic or acidic depending on the film to be patterned). This method, referred to as "chemical wet-etch", is highly selective; if the correct etchant is applied, it attacks only⁴⁸ the intended material. A disadvantage of chemical etching is that it is isotropical. In the uncommon case that the material thickness, i.e. the depth of etching, is comparable to the transverse dimensions of the area (say, the width of the traces), the final patterned film will have oblique walls.

DRY-ETCH Mechanical ("dry") etch can replace the wet-etch described above by bombarding the surface of the thin film with accelerated particles. This method was not as widely applied in our research as wet-etch, though a few experiments did explore the possibilities of the former⁴⁹. One version of dry-etch is called "ion milling", and relates to the acceleration of charged particles. These are directed to intersect the wafer's surface and remove its surface' first few nm. Such a step is especially useful for Al films that tend to create a layer of native oxide, when exposed to the atmospheric air [88]. As alumina, this native oxide layer is isolating, and when galvanic contact is desired between consecutive layers, a few minutes of ion milling is useful to "shave" the Al surface⁵⁰.

LIFT-OFF It is also possible to prepare a resist mask before material deposition, and not subsequently. After the device is covered by a uniform film (as in Fig. 4.3(f)), where part of the resist mask is "caught" below the material to be patterned), the wafer is placed for hours in solvents such as acetone and/or n-methyl-2-pyrrolidone, commonly known as NMP. These solutions attack not the material, but the resist. This patterning method is therefore negative; where resist has been removed, the material remains after the process.

In many cases lift-off is preferable over etching for various reasons. First, unlike wet and dry-etch, no apparent harm is done to the material, which is typically harder to remove than resist. Second, when alignment between consecutive layers are required at the exposure level, and the film to be deposited is opaque (e.g. 100 nm Al), it can be easier to see through a resist mask to find the features of the underlying layer. Since liftoff involves patterning of resist before applying the

⁴⁸Usually the etchant will dissolve other reactants on the wafer with much slower rates. The trick is to assure protective layers, either of resist or even of alternative sacrificial films, later to be removed, sufficiently persistent against the chemistry of the etchant.

⁴⁹See e.g. Fig. 6.2.

⁵⁰Also Si is known for its native oxid growth, and prior to evaporation of Al, the bulk Si wafers were dispensed in hydrofluoric acid to remove the SiO₂ layer, but this was mainly to get rid of parasitic TLS's, and to improve the adhesion of the Al.

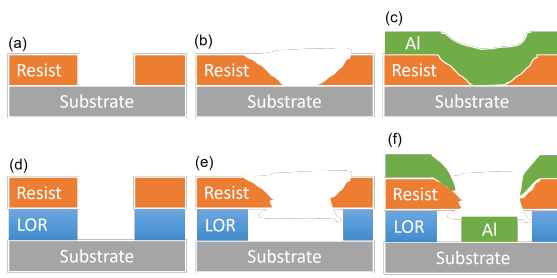


Figure 4.4: Double lithographical layer in lift-off processes. Ideally, if using only one layer, the mask should look like (a) after development, but in practice, due to imperfect focus of the lithography beam and the proximity effect, the mask's wall are oblique like in (b). After deposition, the material (here exemplified by Al) to be removed (on top of the mask), and that intended to remain are connected to each other as in (c), and lift-off of the former may wrap of the latter. When using a double layer (here shown with LOR), the cross section of the wafer *could* look like (d), but when chosen and treated wisely (e.g. by spinning correctly), the LOR is more sensitive to exposure and looks like (e) after development and (f) when deposition has been completed.

metal, the alignment process is far less challenging. And third, eventually the device must be stripped of the resist mask, even after etching processes, and lift-off patterning practically turns this otherwise auxiliary cleaning step into a central part of the fabrication scheme.

Despite its clear advantages lift-off can be difficult, and in the development of new fabrication recipes, it often fails for various reasons:

- The adhesion between evaporated film and the underlying surface is insufficient; e.g. A does not stick to B. In this case, sonication can sometimes removes material residues. For certain substrates the adhesion is improved by a short ion milling sequence prior to evaporation.
- During the evaporation process, the resist is heated radically by the gaseous material during deposition. Of course, baking of resist is a standard step in many processes; softbake is mandatory before lithography exposure to get rid of solvent residues and improve the resist's adhesion to the substrate. Prior to wet-etch, the resist is also hardbaked after development to **harden** the resist, making it robust. But when intended for lift-off, this is obviously counter-productive. The resist must only endure the evaporation, and hardening makes adhesion stronger and the removal becomes even hard. This problem can be overcome by cooling the wafer during the evaporation⁵¹.
- If the exposed areas (i.e. the regions where material is to stay) are too small⁵², the material to be "lifted" draws along the material that landed on the surface at the exposed areas. This problem can be overcome with a double layer of resists. For optical lithography, one uses LOR (lift-off-resists) and for electronic lithography a so-called "co-polymer". The problem and its solution is illustrated graphically in Fig. 4.4.

⁵¹At The Hebrew University's cleanroom facility two evaporators served this research. Only in one of these a chiller system was installed - unfortunately, the pressure in this evaporator only reached $\sim 10^{-6}$ - $\sim 10^{-7}$ torr after 24 hours of pumping, and could only deposit at poor rates of 0.1 nm/sec. The new evaporator (by "Angstrom Engineering") went down to similar pressure in less than an hour and operated at up to 1 nm/sec.

⁵²The characteristic width of traces required for successful lift-off is ill-defined, but in this research all attempt for lift-off of less than $\sim 8 \mu\text{m}$ Al failed.

4.3 Microwave Packaging Environment

The completed fabrication is followed by dicing into 6.2×6.2 cm chips, which are then to be placed in the dilution refrigerator. But mounting and wiring the microscopic nano-devices to a refrigerator's base plate are not trivial tasks. High-fidelity measurements require careful design of both mounting boxes and printed circuit boards (PCBs) and must consider impedance matching⁵³, magnetic field penetration, thermal conductivity, vacuum technology, etc., and remain subject to the attention of many research groups [89, 90].

Boxes and PCBs can in principle be manufactured commercially, but we spent several months to develop an easy approach to design and fabricate simple, yet highly effective packaging consisting of Al boxes and patterned copper PCBs. The fabrication process involves only optical lithography, wet-etch, and computer numerical control (CNC) machining; all facilities which are available at most academic campuses. In addition to the clear advantage of "in-house" manufacturing, an extra convenient property of our packaging environment is that we need to replace only part of the packaging, when changing the geometry of a device.

4.3.1 Defining Box Dimensions

Our architecture includes three layers of which the central part is the PCB, caught between two Al parts (see Fig. 4.6(a)) with a groove for the chip. The chip is secured with vacuum grease, and this installment also benefits the efficient thermalization of the device.

In general, the frequency of the transverse electric ($TE_{m,n,l}$) or transverse magnetic ($TM_{m,n,l}$) standing waves in a rectangular cavity with dimensions a_1, a_2, a_3 , given the modes m, n , and l in the three dimensions, is [34]:

$$f_{m,n,l} = \frac{1}{2} \frac{c}{\sqrt{\mu_r \epsilon_r}} \sqrt{\left(\frac{m}{a_1}\right)^2 + \left(\frac{l}{a_2}\right)^2 + \left(\frac{n}{a_3}\right)^2} \quad (4.15)$$

where c is the speed of light and μ_r and ϵ_r the relative permeability and relative permittivity. For our purpose, assuming $a_2 < a_1 < a_3$, the dominant cavity mode will be TE_{101} . The fact that one of modes m, n , and l can be zero is due to the vectorial nature of the cavity modes. This means that the smallest dimension, typically perpendicular to the chip, is insignificant. To avoid the coupling between the grounded box and the device, a small volume above and below the device is kept hollow. In vacuum, using the ansatz $l = 0$ and following the notation from Eq. (4.15) the lowest TE excitation is thus $f_{101} \simeq c/(2 \cdot a_1)$. Therefore, we require the side length of the cavity to be below 10 mm, ensuring the $f_{101} > 15$ GHz. Such a

⁵³In Sec. 2.1.1 we related to impedance matching of the device, i.e. waveguides on the chip, but also the environment must be impedance matched.

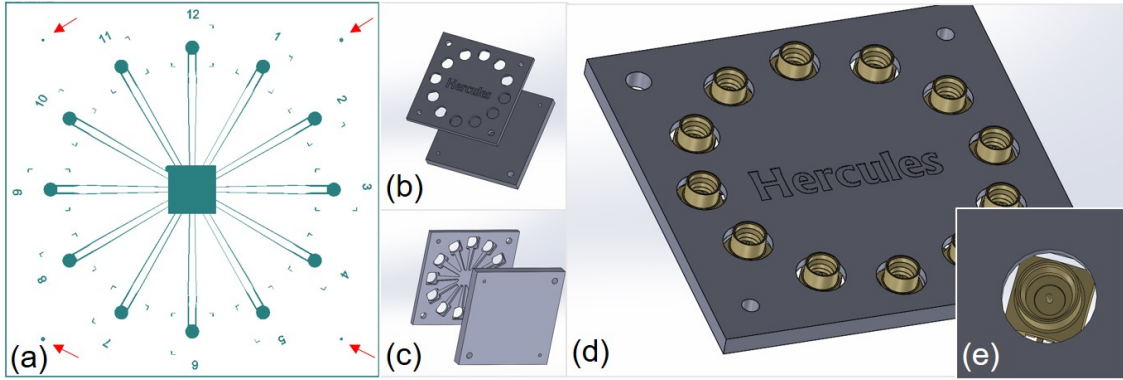


Figure 4.5: Design of box parts: (a) CAD file for PCB production, green areas are etched away during. Square side: 5 cm. Central square side is 6.4 mm, just 0.2 mm larger than the chip. Red arrows mark the points for drilling holes for screws. (b) Top and (c) bottom view of the Al parts, as designed for 3D printing in Solidworks. (d) Upper part of box as seen in Solidworks together with SMP connectors of the "Hercules" box (named so due to the 12 connectors). (e) Zoom on one connector. Note the rounded clamp to increase mechanical strength of the SMP.

box mode is usually sufficiently remote from the experimental bandwidth defined by the measurement electronics⁵⁴.

4.3.2 Printed Circuit Board

In planning the geometry of the PCB (see Fig. 4.5a), we are mainly concerned with matching its traces' impedance Z_t to 50Ω , and to preserve Z_t from the connector to the edge of the chip-groove, while it narrows adiabatically from the geometry recommended by the supplier of the SMP-connectors. We accomplish this by defining macroscopic ($> 100 \mu\text{m}$) coplanar waveguides. The permittivity of the $762 \mu\text{m}$ thick dielectric in this material is $\epsilon_r = 3.48$, covered with $35 \mu\text{m}$ copper.

Using the AppCad software, and accounting for the complete stripping of the rear side's copper plate, we find that $Z_t = 50 \Omega$ is accomplished, when the width of the coplanar waveguide's center-strip is $500 \mu\text{m}$ and the gaps on either side to the semi-infinite groundplanes are $130 \mu\text{m}$. These dimensions result in the phase velocity $v_{ph} = 0.68c$, comparable to the value in coaxial cables [91], and allow the connection of multiple launchers onto the chip, while maintaining sufficient space between PCB traces for thermosonical wirebonds between the respective grounds of the PCB and the chip. This is crucial as at least a handful of the non-impedance-matched wirebonds are required together. In this way their mutual couplings reduce their total combined inductance, and lowers their effective impedance to 50Ω [89].

The RO4350B sheet is initially cut a 3" disc to allow efficient cleanroom handling (e.g. spinning and wet-etch). The disc is cleaned with acetone, spun with a extraordinary thick ($4.3 \mu\text{m}$) photoresist, and patterned with the laser-writer. After development, the copper is removed by wet-etch in ferro-chlorid for 30 min (which is relatively long for a wet-etch sequence).

⁵⁴Our readout circuit includes HEMT and B&Z amplifiers, microwave circulators and attenuators, splitters and other devices, narrowing our operational bandwidth to 2-14 GHz and in some cases 4-8 GHz.

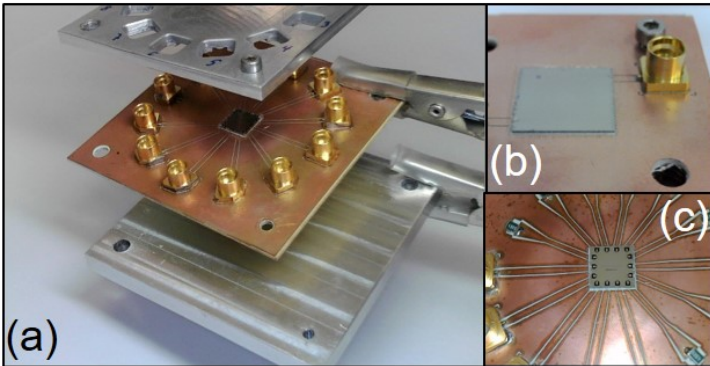


Figure 4.6: Examples of packaging parts. (a) Bottom part, PCB, and top part of "Hercules" box (with 12 connectors). (b) Closer look at PCB of "bird" box (with 2 connectors, of which only one is visible here). Holes for mounting are visible. (c) Closer look at PCB of "Zechariah" box (with 14 lines, some of which are terminated in connectors, others in ground through $50\ \Omega$).

4.3.3 Mounting Box

The two Al plates enclosing the PCB, cf. Figs. 4.5(b)-(c), 4.6(a), are patterned with grooves at the relevant places to avoid contact with traces on the PCB and to lower capacitance between chip and box. Holes are prepared for connectors, and an important detail is the rounded corners (Fig. 4.5(e)) adding mechanical strain on the connectors' corners. Without this feature only the (possibly weak) soldering paste keeps the connector in place, when SMP cables are detached.

The boxes also include holes for mounting to the dilution fridge's base plate, fastening the PCB between the two parts of the box and creating galvanic contact between all three parts. Two additional holes without threads serve for connecting the box to the refrigerator's base plate.

Tiny holes ($\lesssim 0.5$ mm) are also drilled parallel to the box' major plane, both in the top and bottom part, from an arbitrary side and into the central cavity, permitting the evacuation of air, when the exterior of the box is in vacuum.

To avoid direct contact with the ground, traces are opened in the box lid above the designated traces.

4.4 The Dilution Refrigerator

Experiments in SC rf-circuits are performed at ~ 20 mK, i.e. where $kT \ll \hbar\omega$. Dilution refrigerators are required to reach such temperatures, and we use an Oxford Vericold DR-200 model for this purpose.

The refrigerator's operation includes a number of physical processes⁵⁵, but can roughly be divided into three cooling steps: First, temperatures in the single-Kelvin scale are achieved by thermal contact with a ${}^4\text{He}$ bath at ~ 4 K. Next,

⁵⁵The dilution refrigerator is divided into several stages, kept at temperatures of 70 K, 4 K, 900 mK, 100 mK (the "cold" plate) and 20 mK (the "base" plate) respectively. This division stems from the different physical cooling methods working at each stage, and it limits the heat radiation to the base plate.

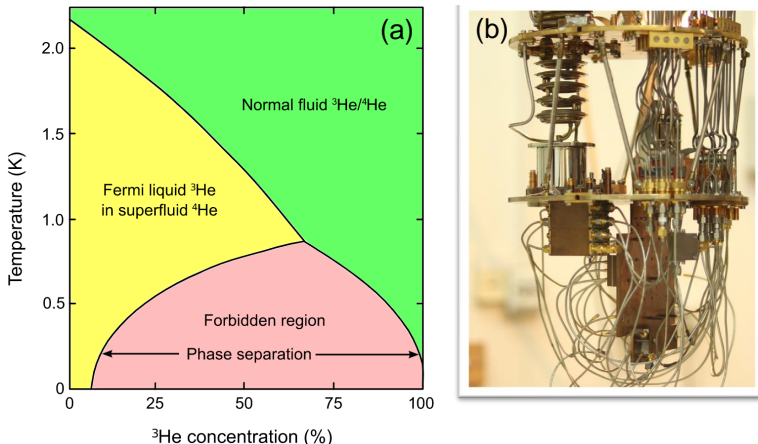


Figure 4.7: (a) Helium mixture phase diagram showing the ³He-rich region in green, and the diluted region in yellow. The second cooling stage (from $\sim 0.9 \text{ mK}$ to 20 mK) exploits the unstable state of the intermediate "forbidden" region (pink). Image from [Wikipedia](#) (under Wikipedia Commons License), reproduced from [92]. (b) Photography showing our refrigerator's two coldest stages with numerous SMA cables. To the left, the mixing chamber (metallic grey box) is visible).

the temperature decreases to below 1 K by means of a Joules-Thompson cycle. This is the endothermic process of adiabatic expansion of the volume of a helium mixture consisting of ³He and ⁴He isotopes. And finally, below $\sim 0.9 \text{ K}$, the mixture spontaneously separates into two phases: A ³He-rich phase (close to 100%) and a dilute phase (which can also be considered a ⁴He-rich phase). In the mixing chamber, ³He is pumped through the phase boundary into the dilute phase. This leaves the formerly rich phase in the thermally unstable intermediate phase (marked in pink in Fig. 4.7(a)). The restoration of the two stable phases occurs, when ³He crosses the phase boundary back again, and this requires enthalpy (i.e. an endothermic process), and provides the source of the cooling power [92]. The mixing chamber is located on the coldest and lowest plate of the refrigerator. Boxes are mounted below it, or to its vertical extension (see Fig. 4.7(b)), which increase the space for boxes, allowing many devices to be cooled down together.

⁵⁶.

The dilution refrigerator is closed by a number of cans for thermal isolation, and an outer vacuum chamber ("OVC") is evacuated to $\sim 10^{-6} \text{ torr}$. Three μ -Metal cans shield the refrigerator (the devices) from external magnetic fields.

4.5 Wiring

After wire-bonding of the devices to PCBs (of the former section), the closed box is mounted to the 20 mK base plate, and SMP-SMA signal cables are attached to the box's connectors.

Engineering the signal transmission is a challenge of its own. Even low powers can result in unwanted heating, so "power budgets" are planned in prior to experiments, detailing what powers are applied in what channels. At the lowest stages cables are of NbTi, superconducting at 10 K, and cables for AC transmission pass through -20 dB attenuators on the 4 K stage and additional attenuators (whose value varies according to the experiment's needs) at the 20 mK plate. Circulators

⁵⁶For more information on the specific dilution refrigerator in our lab, see Fig. 2.3 in Ref. [93].

on the way up (i.e. after measurement, the "output" line) minimize the reflections back into the devices. In certain experiments we also employ cold switches, allowing up to six connected devices occupying only one input/output port.

The output in AC measurements is usually amplified at the 4 K stage with a high-electron-mobility transistor (HEMT) LNR4_8 s/n 091 amplifier from Low-Noise-Factory, increasing the signal by approximately 40 dB. Outside the refrigerator at room temperature we often connect a Low-Noise-Factory LNR4_14 s/n 010 amplifier and/or (depending on the experiment) a BZ-02000800-200822-102020 amplifier, adding 32 dB and 26 dB respectively to the signal.

Cables designated for DC transmission are typically used to measure critical currents of JJ or to create magnetic flux bias in the vicinity of a SQUID. These cables include resistors on the 4 K plate and metal powder filters at the 20 mK plate, to limit the high-frequency noise [94].

In Sec. 5.2.4 we further discuss the noise properties of the components in the microwave measurement chain.

4.6 Electronics

In the simplest transmission experiments⁵⁷ we measure with a Keysight P5024A vector network analyzer. This device is a reliable, user friendly signal generator and also measures output signals, but only at the same frequency as the input. More advance experiments, where input and readout frequencies are different, Anritsu microwave generators produces the input signal. In this case the output is measured with the Agilent N9010A spectrum analyzer or the Agilent infiniium DSO90604A digital storage oscilloscope.

In certain experiments, we make use of in-phase and quadrature (IQ) mixing. An IQ mixer is a microwave component, receiving the input from a local oscillator (LO), and two signals $I(t)$ and $Q(t)$. The LO signal at frequency ω_{LO} is multiplied by $I(t)$ and $Q(t)$ (the last of these with a $\pi/2$ phase shift) and combined in the output signal, which is then

$$V(t) = I(t) \cos(\omega_{LO}t) + Q(t) \sin(\omega_{LO}t) \quad (4.16)$$

As such, the IQ-mixer can be employed for phase modulation and side-band mixing, which all serve standard qubit characterization schemes [53, 95]. Such measurement are not presented here⁵⁸. Instead, we use the Marki 4509LXP IQ mixers for pulse generation. By choosing $I(t)$ and $Q(t)$ wisely, Eq. (4.16) becomes

⁵⁷The characterization of most circuits starts with a transmission experiment. In any circuit with an AC transmission line, we always couple the latter to a test LC-oscillator, whose resonance is sufficiently detuned from the operational frequencies of whatever experiment is served by the transmission line. In this way we confirm the connectivity before commencing actual experiments.

⁵⁸We did fabricate and measure qubits in the lab, but without any innovation value, and those results are not presented in this thesis.

a microwave signal with the desired amplitude and phase.

Measurements including multiple devices were operated with the LabRad software, developed by the Martinis group at UCSB [96]. In 2018 (half way through the research) we purchased a Quantum Machines OPX unit, allowing orchestration the experiments with multiple tools such as arbitrary waveform generation (AWG), analogue-to-digital-conversion (ADC), field-programmable gate array (FPGA) etc.

CHAPTER 5

Results

We are now ready to appreciate the actual results of the research. Many of these are available in the three articles written by the student as first author (see publications), but are concentrated here with additional measurements not previously presented. Following the chronological order of the scientific publications, this chapter is organized as three sections:

- 1) Simulative results of microwave boson sampling
- 2) Amplification experiments in the parametric travelling wave amplifier
- 3) Photonics in compact high-kinetic inductance networks

Empirical data sets in the latter two sections are accompanied by the relevant simulations as explained in the former chapter.

5.1 Analyzing the Superconducting Boson Sampler

5.1.1 The Richness Time

The first necessary step in working with the boson sampling simulator is to establish the time duration necessary to achieve a sufficiently "rich" distribution (given simple Fock states as inputs). A "rich" distribution is, for the purpose of our simulation, defined according to the variance of the occupation of states:

$$\text{Var}\left(P_i(t > T_{\text{rich}})\right) < 1/M^2 \quad (5.1)$$

In our globally coupled network, T_{rich} decreases slowly with the number of modes M . This can be understood intuitively: The more available modes directly coupled to the initially excited mode(s), the faster the latter is (are) depleted. The results of simulations to determine T_{rich} with $M = 10$ and $M = 250$ respectively are depicted in Fig. 5.1.

In the majority of our simulations (all those shown here, except where otherwise explicitly stated) we work with networks of $M = 10$, and our simulations cease at the *final simulation time*, $T_f = 25 \text{ ns}$.

5.1.2 Estimating Decoherence by the Density Matrix

Having established the evolution time necessary for sufficient mixing of the multi-particle walk, we now turn to the main results: Estimating the effect of decoherence in a SC boson sampler. As a metric of this effect, we use the distribution distance:

$$\Delta(\rho(t), \sigma(t)) = \|D_\rho - D_\sigma\|_1 \quad (5.2)$$

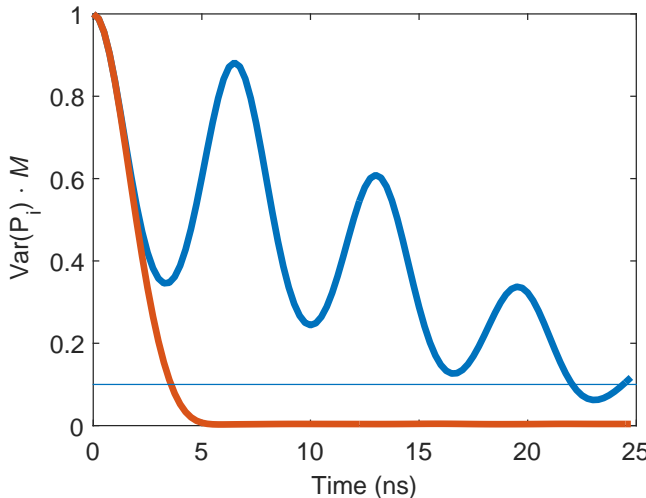


Figure 5.1: Normalized variance of the occupation probabilities for a single boson in the network of M modes. The graphs plot $\text{Var}(\langle P_i(t) \rangle) \cdot M$ for $M = 10$ (red line for $M = 250$) randomly and globally connected resonators. The horizontal line ($1/M$ for $M = 10$) intersects the blue curve at T_{rich} . Note that the normalized variance can rise again over $1/M$ as there is no decay in this simulation. For 250 resonators the richness time is reduced to $\sim 5 \text{ ns}$.

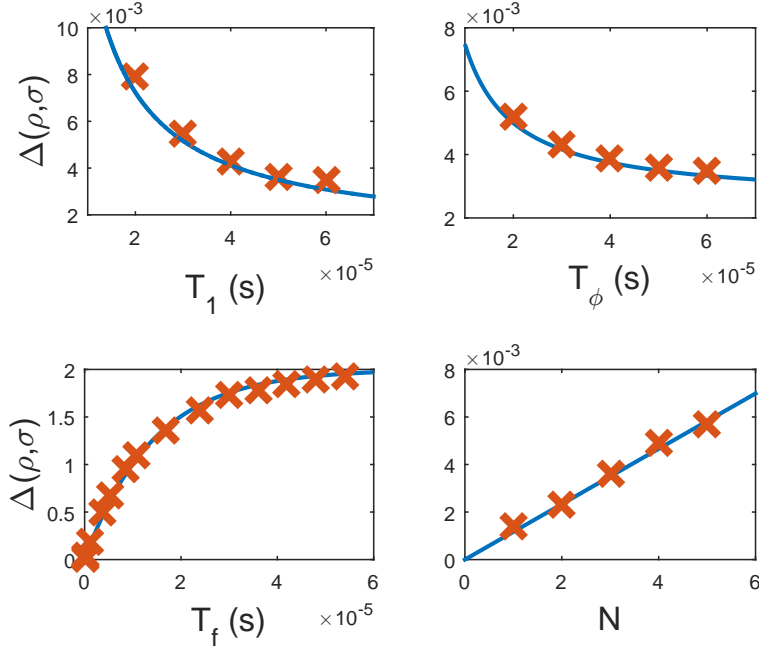


Figure 5.2: Distribution distance, $\Delta(\rho, \sigma)$ for a decohering (with relaxation $T_1 = 50 \mu\text{s}$ and dephasing $T_\phi = 50 \mu\text{s}$ processes) quantum walk of $N = 3$ bosons in a 10 site resonator network, simulated up to $T_f = 25 \text{ ns}$. in each panel plot we simulate the outcome of varying one of the above default values and compare to the phenomenological Eq. (5.3). Top left: varying T_1 , top right: varying T_ϕ , bottom left: varying T_f , bottom right: varying N . For 250 resonators the richness time is reduced to $\sim 5 \text{ ns}$.

i.e. the norm-1 distance between the vectors D_ρ and D_σ , which represent probability distributions in ρ and σ (the matrix diagonals). Here $\rho(t)$ and $\sigma(t)$ are the density matrices after coherent and decohered time-evolutions respectively.

In all numerical experiments, we calculate only a moderate exponential increase in $\Delta(\rho(t), \sigma(t))$ over time. We find this quantity to fit the phenomenological formula:

$$\Delta(\rho(t), \sigma(t)) = 2 \left(1 - e^{-\frac{Nt}{3} \left(\frac{5}{2} \frac{1}{T_1} + \frac{1}{T_\phi} \right)} \right) \quad (5.3)$$

where T_1 and T_ϕ are the energy relaxation and pure dephasing times of the resonators⁵⁹.

The reliability of the empirical approximation of Eq. (5.3) can be seen in Fig. 5.2. In this figure's four panels we scan the different parameters of our simulation (T_1 , T_ϕ , T_f , and the number of excitations N) and plot Eq. (5.3). For all panels (unless the particular parameter is explicitly scanned in the x-axis), we set $T_1 = 50 \mu\text{s}$, $T_\phi = 50 \mu\text{s}$, $N = 3$, $M = 10$, and random global couplings with a uniform distribution between 20-40 MHz⁶⁰. The same randomly generated coupling graph was used in all simulations (iterations performed using other randomly generated graphs with similar energies did not reveal any remarkable difference). The exponential growth of the required Hilbert space required extensive runs (over a few hours per run) on a powerful desktop computer to complete simulations for $N > 4$.

⁵⁹While Eq. (5.3) fits the experimental data quite well as shown in Fig. 5.2, the source of the specific numerical factors (1/3 and 5/2) are still subject to research. The same goes for Eq. (5.5).

⁶⁰High quality, planar, state-of-the-art superconducting resonators and qubits have demonstrated energy decay times T_1 of $\sim 50 \mu\text{s}$ and T_ϕ , the dephasing time, is here conservatively assumed to be $\sim 50 \mu\text{s}$ [97]. Fabrication and control of qubits have improved since our work was published in 2017. Works with SC qubits with decoherence times in the order of milliseconds have been published [98, 99], but our analysis show that even with decent, but not superior qubits, SC circuits are capable of boson sampling despite the decoherence effects.

An additional interesting observation in our simulations is that the number of resonators does not appear directly to affect the decay and only enters implicitly through the requirement of achieving the richness time of fully propagating individual bosons throughout the array. This is of-course important for scaling up systems.

The trace distance $\mathcal{D}(\rho(t), \sigma(t))$ is a quantitative measure of decoherence, alternative to the distribution distance $\Delta(\rho(t), \sigma(t))$ that we have used so far. It is harder to measure than $\Delta(\rho, \sigma)$ directly in experiments, but with Wigner tomography it can be reconstructed [100]). Defined as

$$\mathcal{D}(\rho, \sigma) = \frac{1}{2} \sum_i |\lambda_i| \quad (5.4)$$

where λ_i are the eigenvalues of $(\rho - \sigma)$, we find the trace distance to be well fitted by the phenomenological model

$$\mathcal{D}(\rho(t), \sigma(t)) = 1 - e^{-Nt\left(\frac{1}{T_1} + \frac{3}{2}\frac{1}{T_\phi}\right)} \quad (5.5)$$

It is stressed that \mathcal{D} does not depend on the specific couplings between the M resonators (this was verified with different randomly generated graphs).

When comparing the two metrics, $\mathcal{D}(\rho, \sigma)$ turns out to be more sensitive to changes in T_ϕ than to T_1 , and more sensitive to such changes in T_ϕ than $\Delta(\rho, \sigma)$ was found to be. On the other hand, $\Delta(\rho, \sigma)$ was more sensitive to changes in T_1 . This conclusion can be reached and intuitively understood by the definition of $\mathcal{D}(\rho, \sigma)$, where off-diagonal terms are considered and thus relating more directly to the dephasing effects, i.e. T_ϕ . Since $\Delta(\rho, \sigma)$ measures the probabilities only and not the phases, the energy relaxation implemented by T_1 naturally has a more significant effect on this parameter than T_ϕ .

5.1.3 Interferometric Sensitivity of Boson Sampling

We test the sensitivity of our system by randomly perturbing the couplings between resonators. An ensemble of perturbation graphs is generated (again with random couplings uniformly chosen between 20 and 40 MHz) and added to the reference graph with a pre-factor of 10^{-3} . This procedure establishes slightly altered Hamiltonians by which the system evolves. Specifically, we take a random-coupling network of 10 resonators and generate 1000 randomly perturbed graphs. Here we do not include Krauss operators to avoid confusing the perturbation and decoherence effects. The subsequent distribution distance between a perturbed and reference evolution after a simulation of $2T_{rich}$ is calculated.

The distribution distances yielded by perturbations in the graphs are now computed for both initial Fock states (one photon in each of three different resonators)

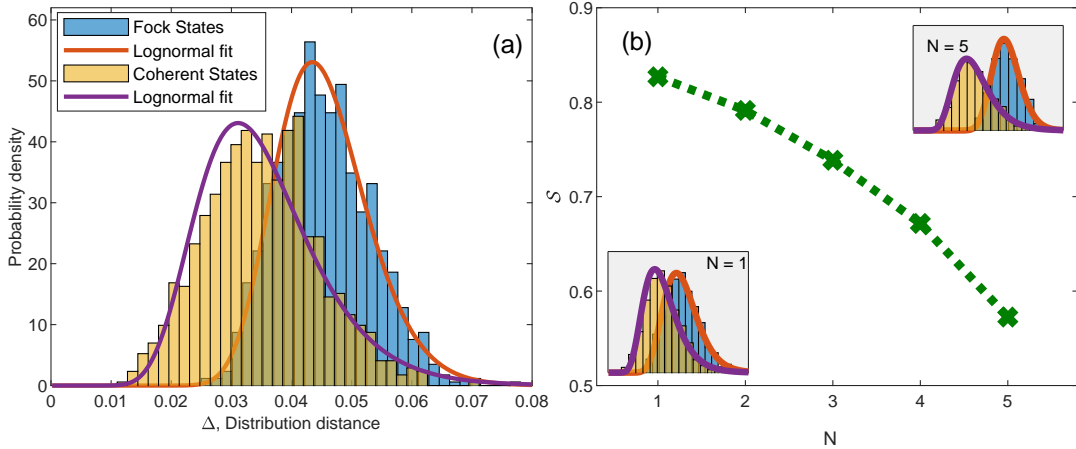


Figure 5.3: (a) Histogram of the distribution distances, Δ , for initial single photons in resonators and coherent states. The simulation was carried out in a 10 site network, with an ensemble of perturbations, and $N = 3$ bosons. The same perturbations were applied for both kinds of initial states. For the coherent state a classical "amplitude simulation" was performed, with $\alpha=1$ in three resonators in same modes. (b) S decreases as N grows larger, emphasizing the advantages of using quantum states rather than classical states for sensing with the boson sampler. Insets show S for the first and last data point of the graph.

and initial coherent states,

$$|\alpha\rangle = e^{-\frac{|\alpha|^2}{2}} \sum_{n=0}^{\infty} \frac{\alpha^n}{\sqrt{n!}} |n\rangle \quad (5.6)$$

with an average occupation $\langle n \rangle = |\alpha|^2$ of one photon in three of the resonators. This allows us to distinguish classical interferometric sensitivity vs. many-body effects.

Fig. 5.3(a) shows the distribution distances for many realizations of perturbed couplings, and we observe a definite difference between the coherent state inputs and single photons. Both histograms of distribution distances are fit well by log-normal distributions, but the input Fock state is clearly less robust to perturbations than the coherent states. This is promising as it indicates higher interferometric sensitivity for the quantum walk interferometry vs. classical (coherent state) probing. Surprisingly though, the result is the opposite for $D(\rho, \sigma)$ as described above and seems to indicate less interferometric sensitivity for the quantum walk interferometry vs. classical (coherent state) probing. The explanation as to this difference lies within the nature of coherent states. These dephase faster than the Fock states, and this is exactly the tendency, which the trace distance detects efficiently compared to the distribution distance. The decoherence estimator must therefore be chosen appropriately, when given processes are to be distinguished [26].

The higher sensitivity of the Fock states is enhanced as the number of bosons increases. To quantify this effect, we define the "distribution overlap":

$$\mathcal{S} = \int dx \sqrt{f_{Fock} f_{coh}} \quad (5.7)$$

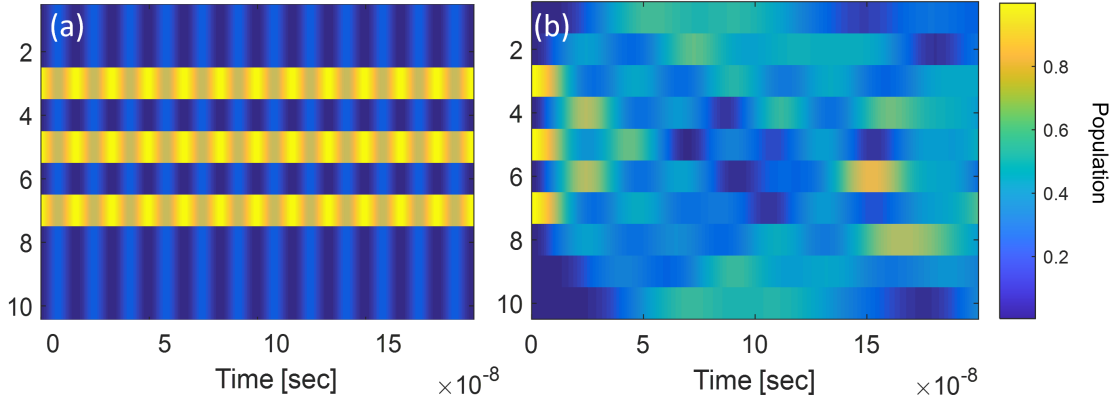


Figure 5.4: Confinement when disorder is removed. (a) Time evolution as 10 resonators are all mutually coupled to each other with the same coupling strengths. The three photons initially excited in the $3^r d$, $5^t h$, and $7^r d$ resonators stay at those sites. (b) When returning the disorder (by limiting couplings to nearest neighbors) an ordinary diffraction pattern appears

corresponding to the shaded area on Fig. 5.3(a), where f_{Fock} and f_{coh} are the probability distributions emerging from iterations of the simulation with initial Fock states and coherent states respectively. \mathcal{S} equals unity, when the two distributions are identical. Fig. 5.3(b) shows that the quantum advantage is enhanced (\mathcal{S} decreases) when the number of initially excited states is raised.

5.1.4 Confinement and Localization

Our simulations also show that interference together with perfect symmetry leads to confinement of the propagating excitations in our network. When disorder is removed from the system and all couplings are made equal as in Fig. 5.4(a), the excitations remain in their initial resonators throughout the duration of the simulation. This happens, as they are detuned from the dressed reservoir of other sites - it is the disorder in interaction strengths that releases them. The confinement effect becomes more pronounced as the number of resonators is increased, starting with simple sloshing between two modes. For the same reasons, when initially placing an equal amount of excitations in each resonator, there is no change in the occupation of the resonators. This is of course true even with disorder.

We note connections to the extensively investigated Anderson localization phenomena; *high* degrees of disorder⁶¹ causes a transition from ballistic propagation to localization of particles traveling in a lattice. This has been demonstrated with photons traveling in a two dimensional coupled lattice of waveguides, a system closely related to our proposed network of SC circuits [101, 102].

5.1.5 The Boson Birthday Paradox

Finally, our simulations predict the occurrence of the "bosonic birthday paradox" [64] in our proposed network. The physics of this interesting quantum

⁶¹Anderson localization was observed when the onsite energies were uniformly distributed between 250-750 MHz.

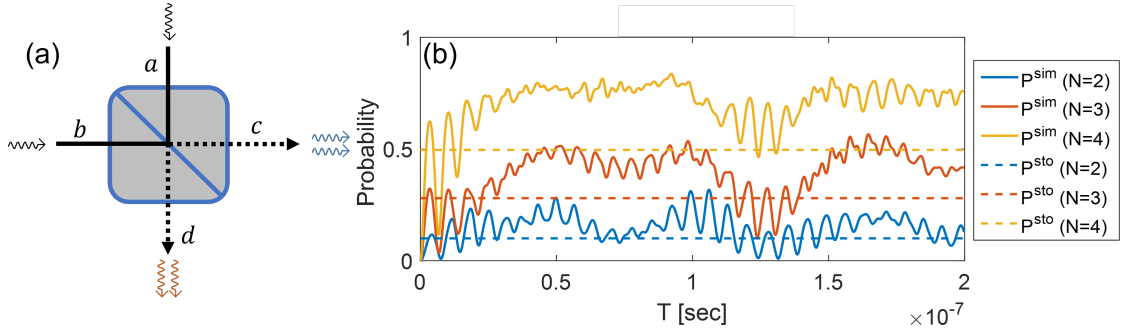


Figure 5.5: (a) The Hong-Ou-Mandel experiment describes the bunching of two photons entering a beam splitter separately and leaving together. (b) Observation of bunching in our simulations. Colors represent the number initially excited modes (all by single photons only). Broken lines are stochastic probabilities, cf. Eq. (5.8), and full lines show P_b from the simulations.

phenomenon has roots in the Hong-Ou-Mandel experiment [1] illustrated in Fig. 5.5(a), where two photons simultaneously enter the two input ports in a linear beam splitter, one in each (marked as ports *a* and *b* in Fig. 5.5(a).) The exciting effect is the surprising exit of the two photons together; either through port *c* or port *d*, but not separately, due to destructive interference. Appendix D derives this result analytically together with the "birthday paradox": Against commonsense intuition, there is a rather high probability P_d that at least one pair of people in a group of N individuals share a birthday, even when $N \ll 365$, the number of possible birthdays, e.g. $P_d(N = 23) = 50\%$, and for $N = 70$, $P_d \sim 99.9\%$.

Replacing humans with photons and calendar dates with output modes in the linear network, the bosonic version of the birthday paradox relates to fact that, due to interference between the bosons as in the Hong-Ou-Mandel experiment, we expect a high probability of observing more than one boson in at least one mode (the probability of bunching, P_b).

Fig. 5.5(b) compares the probability from the simulation (without decoherence) with the stochastic expression that two bosons occupy a common mode:

$$P_{\text{sto}} = 1 - \frac{1}{M^N} \frac{M!}{(M-N)!} \quad (5.8)$$

As the number of initially excited modes grow larger, also the accumulated ratio of time where $P_b > P_{\text{sto}}$ is extended. Even though the bosons in our system do not interact "directly" (i.e. $U_i = 0$ in Eq. (4.1)), the quantum states interfere with each other. This is a multipartite version of the Hong-Ou-Mandel effect.

5.2 The Kinetic Inductance Travelling Wave Amplifier

The work on the microstrip kinetic inductance travelling wave amplifier was mainly experimental, but was accompanied by simulations, both in planning and design, and in evaluation of the results.

In the attempt to fabricate a reliable amplifier many generations of devices were

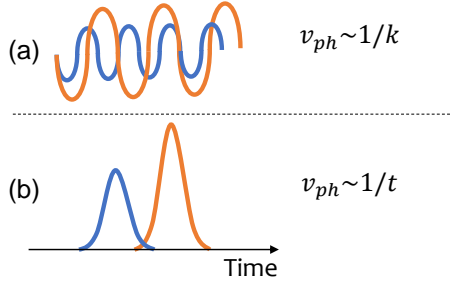


Figure 5.6: Methods for measuring the phase velocity through the HKI amplifier: (a) Comparing the phase difference between CW transmitted through the amplifier and through the control line, and (b) comparing the arrival time of pulses transmitted through the same two channels. The value of v_{ph} found by both methods deviate by less than a few percents for the theoretical estimation.

prepared and measured. Consistent with the theoretical values of Table 3.1, our best functioning microstrips had $L_k \sim 50 \mu\text{H/m}$, and $C_l \sim 20 \text{nF/m}$. Such numbers ensured a characteristic impedance of 50Ω and a theoretical $v_{ph} \sim 0.004c$, where c is the speed of light in vacuum. We verified this value in two ways:

1. by detecting the phase shift of constant wave (CW) signals and comparing to similar signals transmitted in a different measurement through a parallel control channel, and
2. by broadcasting a pulse (a gaussian wave packet) through the amplifier, and comparing the delay in arrival with the corresponding measurement through the control channel.

We found similar values of v_{ph} by both methods, consistent with the theoretical expectation. In a separate measurement we determined the critical current of the WSi trace to be $I_c \simeq 0.06 \text{ mA}$.

5.2.1 One-tone experiments

The most basic characterization of our device is the single-tone transmission measurements done by the vector network analyzer. We thus plot the nonlinear mag-

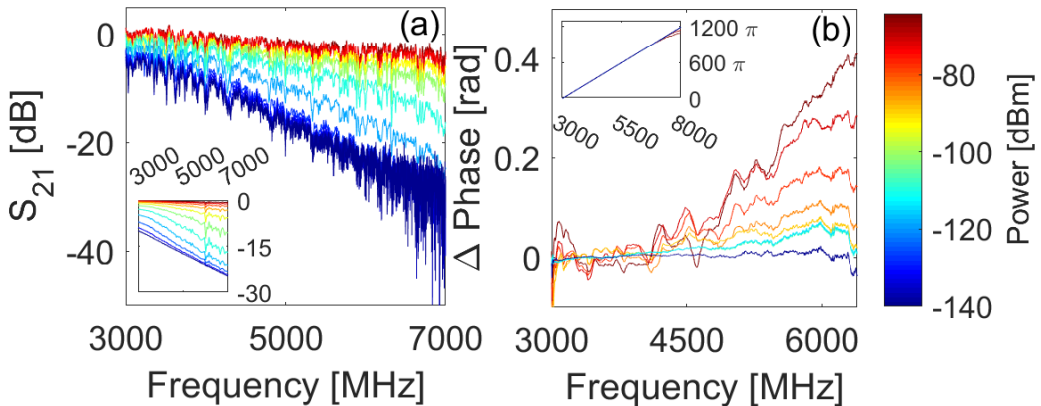


Figure 5.7: Nonlinearity in single tone measurements. (a) Magnitude of the measured signal transmission, as the input power is scanned. Inset: Simulation, accounting also for loss saturation according to the standard TLS model [6, 82] (assuming a low power loss tangent of 5×10^{-4}), cf. se (b) Unwrapped nonlinear phase of measured signal, referenced to the lowest power and to the individual power level's phase at 3 GHz. Inset: Linear phase, relative to lowest measured frequency.

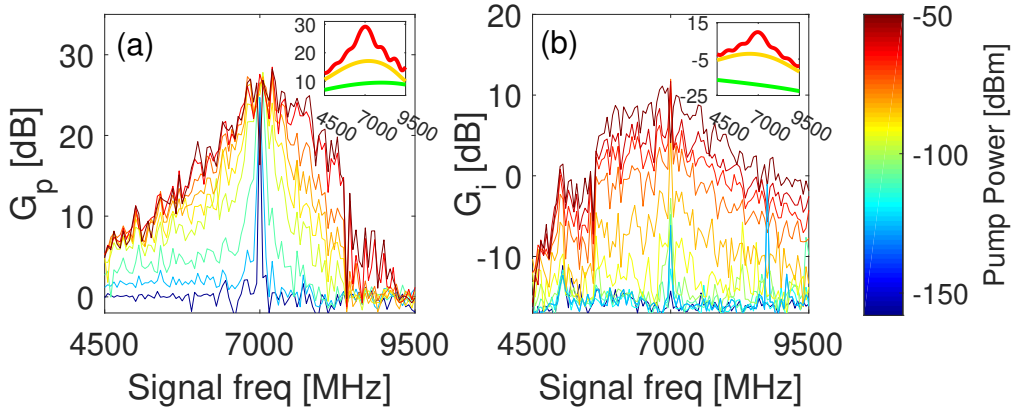


Figure 5.8: Two-tone experiments demonstrate the parametric amplification and wave-mixing in the microstrip amplifier. (a) Pump amplification factor G_p for a signal at various f_s (at -140 dBm), when the power of pump at $f_p = 7.0$ GHz is increased. Inset: Simulations for pump powers -50 dBm (red), -80 dBm (yellow), and -110 dBm (green) show consistent amplitudes and bandwidth of G_p as in experiment. (b) Idler conversion efficiency measured at $f_i = 2f_p - f_s$. Inset: Simulation with color map as in (a).

nitude of the transmission in Fig. 5.7(a). The power-dependent loss is associated with saturation of two-level systems (TLSs) as we described in Chap. 2, and agrees with ab initio simulations (where we use $\tan\delta = 5 \times 10^{-4}$) shown in the inset of the same figure. These simulations also indicate that stronger amplification is accomplishable with only moderate improvements to the device, such as higher nonlinearity (i.e. lowering I_c) or reduced loss (achieved by alternative dielectric materials).

In turn, Fig. 5.7(b) displays the *nonlinear* phase accumulated through the device. This is the feature allowing wave-mixing and amplification, cf. Eq. (3.17). The nonlinear phase should be considered in light of the *linear* phase accumulation of $\sim 10^3$ radians (inset of Fig. 5.7(b)). The slope of the nonlinear phase increases linearly as a function of the pump power in accordance with Eq. (3.17). Here we show measurements up to 6.3 GHz. Losses make the extraction of the nonlinear phase difficult at low power beyond this frequency.

5.2.2 Two-tone experiments

We now proceed to the more important two-tone (amplification) experiments, where wave-mixing between a signal at low power at frequency f_s and a high-powered pump at f_p amplifies the former and produces an idler tone at f_i . The idler tone emerging at $f_i = 2f_p - f_s$ is found as f_p is kept constant at various powers, and the signal power is kept constant for changing f_s .

The strong idler (shown in Fig. 5.8b) confirms the wave-mixing taking place in the amplifier.

Quantitative characterization is done with G_p introduced in Eq. (3.20) and G_i , the idler conversion efficiency (analogous to \tilde{G}_i defined with G_s in Eq. (3.19), but now with G_p). In the lossless case G_i can be written as $G_i = |A_i^{out}|^2 / |A_s^{in}|^2$). As

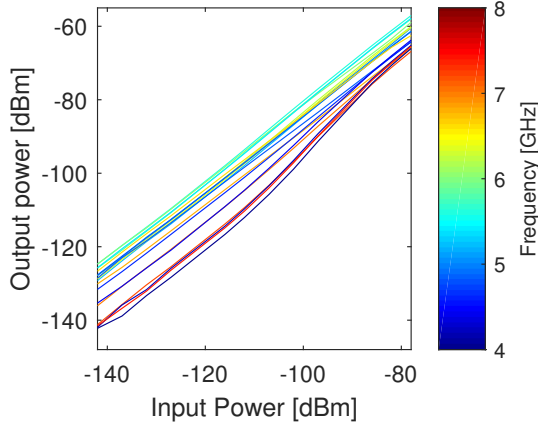


Figure 5.9: Dynamic range: G_p is nearly constant for various f_s values, when we increase the signal power six orders of magnitude and keep the pump power -53 dBm constant at $f_p = 6.0$ GHz.

mentioned, G_p is chosen to evaluate the efficiency of the amplifier instead of G_s from Eq. (3.18) as it emphasizes the nonlinearity of the amplifier itself⁶². Hence, using G_i instead of G_s allows us to separate the amplification from the loss effects, at least for the lowest energy levels where no saturation effects occur.

5.2.3 Dynamic range

The dynamic range is a central property, when characterizing any sensor or amplifier. Most commonly defined as the ratio between the largest and the smallest values that can be assumed by the device, it practically sets the range of operation.

Below the lower bound of an amplifier's range, signals are simply not picked up. In our amplifier, this would happen, when the pump is not sufficiently strong to generate enough wave-mixing. At the upper limit of an amplifier's operational range, it reaches a "compression point", where amplification might still take place, but with reduced efficiency⁶³

The transmission of the signal through the amplifier is nearly linear (as can be seen in Fig. 5.9), as the power increases by more than six orders of magnitude from -140 dB (below the power level equivalent to single-photon), while a pump at 6 GHz is kept constant at -53 dB.

5.2.4 Noise temperature

Like the dynamic range, the noise temperature is an important benchmark of the amplifier.

Any measurement suffers from noise. The level of noise can be expressed as a temperature by division with the Boltzmann constant. Our dilution refrigerator's physical temperature is 20 mK at the MC plate, but the noise temperature is higher.

Our amplifier is the first component in a cascade of components, including

⁶²For our device, $G_s \simeq 10$ dB over a ~ 1.5 GHz bandwidth around the pump depending on the frequency. Had we chosen the more conventional signal gain, the result had been ~ 5 dB lower due to the loss.

⁶³It is never recommended to work about the compression point of an amplifier or a sensor. Even though the exact amplification might be known, the amplifier might, at some point be damaged by the strong power transmitted.

commercial amplifiers and effective attenuators as shown in Fig. 5.10(b), and we find its effective noise temperature T_{eff} by solving the recursive equations for N_{in} and N_{out} , the input and output noise of all components from the amplifier and up through the line. Each component is treated either as an attenuator or as an amplifier. The mathematical definitions for the numerics appear in Table 5.1, and depend on the bandwidth B (91 Hz in all our measurements), the effective noise temperature, and the gain ratio G^* . Of course $0 < G^* < 1$ for attenuators and attenuating components (cables, circulators, etc.), and $G^* > 1$ for amplifiers.

An example⁶⁴ of the recursive computation is given in Table 5.2. When loss is considered bigger in e.g. the circulators, a different result is obtained.

We determine the G^* of the amplifier by comparing the measured output in the case of the highest transmission on Fig. 5.10(a) with that from the control line (not shown), and we hereafter adopt the base line or *noise floor*, -108 dBm, as the noise output at the end of the cascade. Rigorously solving for each component in the chain, including cable loss (treated as attenuation), sets the noise temperature of the amplifier to be 0.25 K $< T_{eff} < 0.41$ K. The uncertainty results from an additional loss of ~ 3 dB in the line measured, which we were unable to affiliate with localized components in the cascade (leaving the temperature and position of these sources of loss in the line uncertain).

5.2.5 Simulations of the Amplifier

The results from the work on the HKI WSi amplifier are supplemented with simulations in addition to those shown in the insets of Fig. 5.8.

Fig. 5.11(a) shows how the reduced v_{ph} is expected to enhance the amplification. Though based on the specified amplifier length, pump frequency, and pump power of our implementation, the result is quite general and has been reproduced for various other frequencies.

Noise definitions	
Noise figure	$F = \frac{S_{in}/N_{in}}{S_{out}/N_{out}} = T_{eff}/T_l \geq 1$
Loss factor	$L^* = 1/G^* > 1$
Attenuator output noise	$N_{out} = N_{in}G^* + (1-G^*)hf\left((e^{hf/k_bT}-1)^{-1} + \frac{1}{2}\right)$
Amplifier output noise	$N_{out} = N_{in}G^* + k_bT_{eff}B$

Table 5.1: Definitions of the noise figure, the loss factor, and the output noise used to find the noise of the amplifier as shown in Tab. 5.2 by recursive calculations [34]. S and N are signal and noise and output (subscripts signifying if for input or output). A star ($*$) indicates units of power *ratio* rather than dB (e.g. -20 dB $\rightarrow 10^{-2}$, $+40$ dB $\rightarrow 10^4$). T_l is the physical temperature, T_l the temperature of the load, and T_{eff} the effective noise temperature. B is the bandwidth and k_b the Boltzmann constant. Also, T in the attenuator's output noise is the physical temperature. Note the various limits of this expression: For $T \rightarrow 0$, the exponent goes to infinity, and we receive the quantum noise $\frac{1}{2}hf$ (times the gain fraction). At high temperatures, $T \gg hf/k_b$, the exponent can be Taylor approximated to $1 + \frac{hf}{k_bT}$. We then reach the classical noise term of k_bT .

⁶⁴The numbers in Table 5.2 are based on the most optimistic scenario with relatively low noise in the various components in the chain.

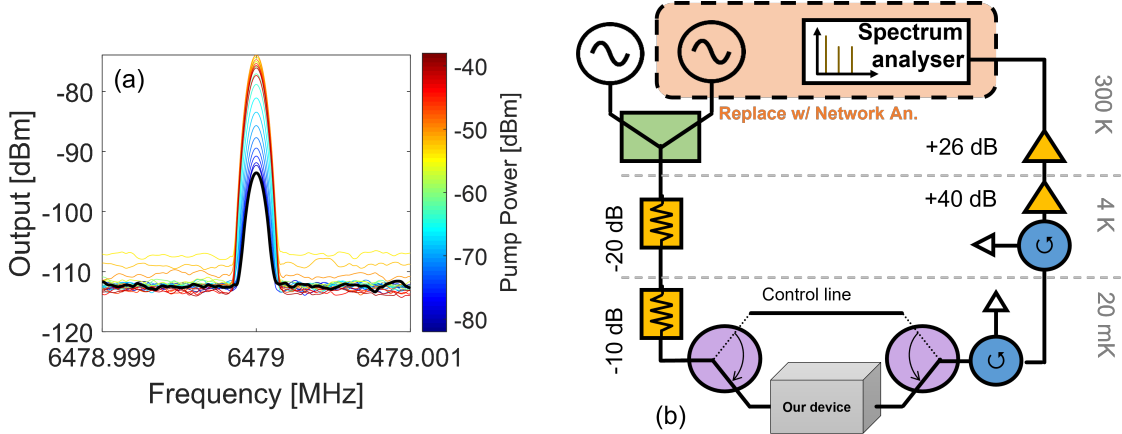


Figure 5.10: (a) Signal-to-Noise measurement of our amplifier at changing powers of an off-resonance. Black line indicates the case without a pump. From this graph we determine the gain ratio of our device used in Tab. 5.2. (b) Measurement chain: Signal and pump are generated in two Anritsu MG3692B microwave generators (MG), merged in a power combiner (green) at room temperature, and passed through microwave attenuators (yellow). For calibration we connect the MI-KITWA in parallel with a control line through cold switches (purple) on both sides. The output passes through circulators (blue) to avoid reflections. Conventional amplifiers are placed at 4K (HEMT LNF-LNC) and T_{room} (B&Z LNA 2-8 GHz) before readout in a Keysight EXA N9010A spectrum analyzer (SA). In experiments without idler-measurements, the SA and one MG are replaced with an N5230A vector network analyzer (light orange).

In practice, we cannot distinguish between pump and signal photons, when their frequencies coincide, but in the close vicinity of the pump (detuning of $\lesssim 100$ MHz), Fig. 5.8(a) does not indicate any significant decrease of G_s , and $G_s(f_s = f_p)$ is thus a legitimate measure even for experimental purposes. Based on this assumption Fig. 5.11(b) quantifies the effect of the linear loss effects, i.e. without saturation effects for a signal at $f_s = f_p$. As indicated in the caption, the central parameter in this simulation is the *nonlinear phase shift* $\phi = \gamma kz$ where $\gamma = |A_p(0)|^2 / (2|I_\star|^2)$.

Extending the length z of the amplifier increases G_s , but the loss intensifies as expressed by the loss factor $L = e^{-2\Gamma_s z}$ (note the factor of 2: as this is *power* decay, whereas $A_{s,p,i}$ are amplitudes of current components). Here we again ignore

Gain and noise in the measurement chain					
Component	Gain ratio	P_{out} [W]	T_0 [K]	Noise [W]	P_{in} [W]
End cable	3.0×10^{-1}	2.5×10^{-14}	3×10^2	3.8×10^{-19}	8.3×10^{-14}
B&Z	3.98×10^2	8.3×10^{-13}	3×10^2	1.6×10^{-19}	2.1×10^{-16}
HEMT	10^4	2.1×10^{-16}	4	3.8×10^{-21}	1.7×10^{-20}
Circ@4K	9.0×10^{-1}	1.7×10^{-20}	4	3.8×10^{-21}	1.9×10^{-20}
Circ@20mK	9.0×10^{-1}	1.9×10^{-20}	2×10^{-2}	2.5×10^{-23}	2.1×10^{-20}
Switch	6.3×10^{-1}	2.1×10^{-20}	2×10^{-2}	2.5×10^{-23}	3.3×10^{-20}
Our amp	63	3.3×10^{-20}	2×10^{-2}	?	5.2×10^{-22}

Table 5.2: Working from the top of the refrigerator and down to the base plate, we estimate the noise temperature of each component, given the noise added at the former level as shown in Fig. 5.10(b). The "end cable" is the co-axial cable between the commercial B&Z amplifier and the signal analyzer. Everything but the amplifiers are treated as effective attenuators, as the signal transmission is slightly reduced in their presence. Circ@4K and Circ@20mK are the circulators at the 4 K plate and the base plate respectively.

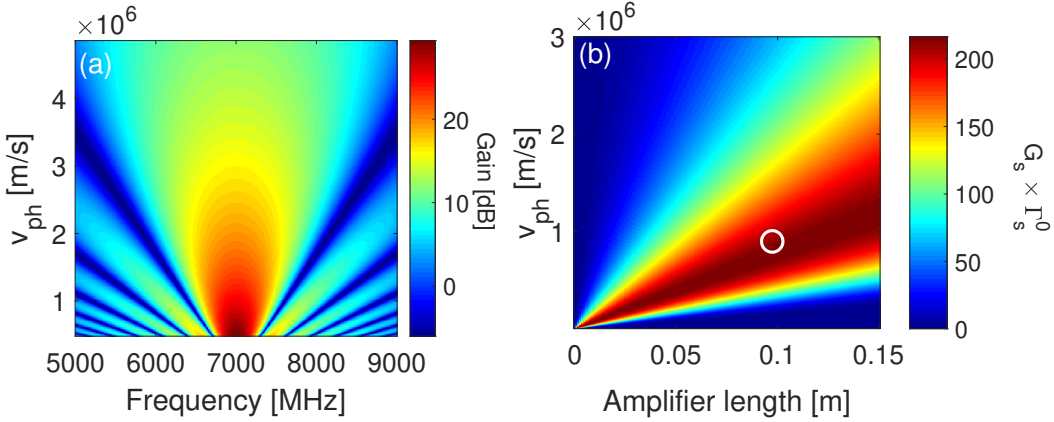


Figure 5.11: Simulations showing the impact of reducing the phase velocity on the amplification. (a) Amplification (in dB) for a -48 dBm pump at $f_s = 7 \text{ GHz}$ and a signal of -110 dBm , neglecting nonlinear loss effects. (b) Signal gain ratio as defined in Ref. [3]: $G_s = (\gamma kz)^2 + 1$ times the power loss factor $L = e^{-2\Gamma_s^0 z}$, simulated without saturation effects for $f_s = 7 \text{ GHz}$ (with $\gamma = |A_p(0)|^2 / (2|I_*|^2) = 0.1$). The white circle indicates our working parameters $z = 11.6 \text{ cm}$ and $v_{ph} = 0.0035c$. Note that the theoretical amplification is a few dB higher than what we found empirically, even after loss effects are taken into account. This discrepancy is likely due to the simulation's sensitivity to parameters such as $\tan\delta$ and I_* .

saturation effects. Also the signal gain $G_s = (\gamma kz)^2 + 1$ depends on both length and phase velocity [5], and the product $G_s \times L$ thus predicts for which (v_{ph}, z) the highest amplification is accessible, as shown in Fig. 5.11(b).

5.3 Networks of Microstrip Waveguides

Photonics is an important research discipline for quantum optics, simulation, and technologies, but its integration in superconducting circuits is constrained by the long wavelengths (in the order of $\sim \text{cm}$) and as we have already discussed: impedance mismatches in this platform. Long wavelengths result in long waveguides, and when advanced photonics is to be demonstrated, devices are often required to include multiple waveguides, each of several wavelengths to ensure sufficient phase accumulation and strong couplings (if desired for specific experiments). On other words, the devices quickly grow large, beyond the compatible areas of SC devices⁶⁵. The challenge is, in other words, scalability.

The geometry of our microstrip amplifier provides an immediate solution to this problem. With v_{ph} two orders of magnitude shorter than the typical figure for Al waveguides, wavelengths λ reduce to $\sim 10^2 \mu\text{m}$.

In addition to 50Ω matched waveguides, approximately $3 \mu\text{m}$ wide, we employ submicronic wires as already described in Chap. 4 as effective couplers in our system. Since the couplers' widths are narrowed down to about 1/10 of the 50Ω waveguides' width, L_l of the former is increased by an order of magnitude. Following these geometric changes also C_l becomes smaller by the same ratio,

⁶⁵There are various limitations on the size of devices, perhaps most central is to avoid box modes in the operational bandwidth, as described in Sec. 4.3.3.

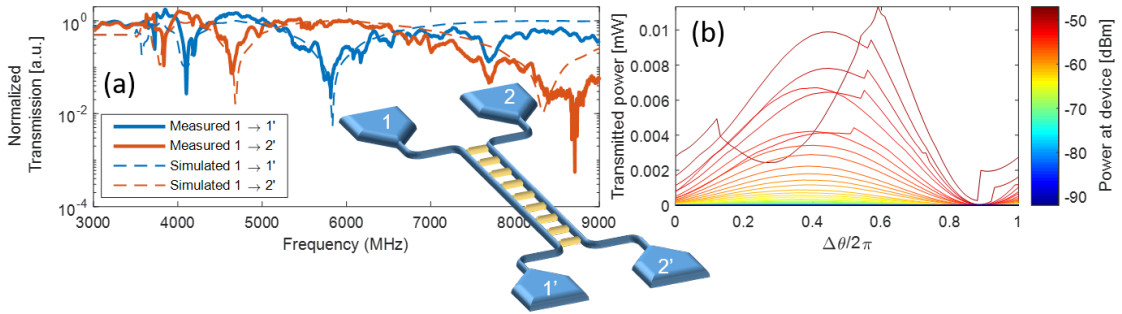


Figure 5.12: (a) Direct and coupled transmission measurements and simulation for two parallel microstrip traces periodically coupled through highly inductive nano-wires. Inset: Graphical illustration of the device. Blue: Launchers and traces. Yellow: Coupling nano-wires. (b) Phase-dependent transmission, as CW signals are applied in both traces simultaneously, with changing input powers in port 1 (represented by colorbar) and changing phase in port 2 (horizontal axis). The measured output in port 2' (vertical axis).

and the outcome is that the couplers behave as mostly inductive links. It is also worth noting that the couplers' Z_l is an order of magnitude larger than that of the waveguides, confirming their perturbative role as a weak link.

We demonstrate the possibilities of the SC microwave photonics with three different networks (as shown in Fig. 4.1) constructed of waveguides and couplers.

5.3.1 Two Coupled Travelling Waveguides (2CTW)

The 2CTW consists of two parallel microstrip travelling waveguides, distanced by $30 \mu\text{m}$, and connected by couplers every $100 \mu\text{m}$. The total length of each waveguide, i.e. from launcher to launcher, is $3 \text{ mm} > \lambda \simeq 400 \mu\text{m}$. An illustration of this device appears in the inset of Fig. 5.12(a).

In an initial characterization of the 2CTW we measure the output in both of the waveguides, when CW signals are applied into one of them (see Fig. 5.12(a)). The unemployed launcher (port 2 in Fig. 5.12(a)) is connected to the ground through attenuators and a 50Ω resistor at the refrigerators base plate (i.e. at 20 mK) to avoid reflections into the waveguide. Our simulations, based on voltage continuity and current conservation, quantitatively predict the frequency-dependent transmission of this circuit (broken lines in Fig. 5.12(a)).

Characteristic features, such as the flat region at low frequencies and the alternating transmission peaks and dips, can be linked to the band structure of the corresponding periodic (infinitely extended) device. See Appendix C for details on the simulation of this device.

We also observe interference between signals introduced simultaneously in the two waveguides: In Fig. 5.12(b) we alter the phase difference between the two inputs, and while we measure the transmission through one wave-guide, the signal power in the other ("the neighbor") is scanned over four orders of magnitude (and for all relative phases). With negligible power in the neighbor, the signal in the waveguide alone is large enough for us to observe a drastic reduction of

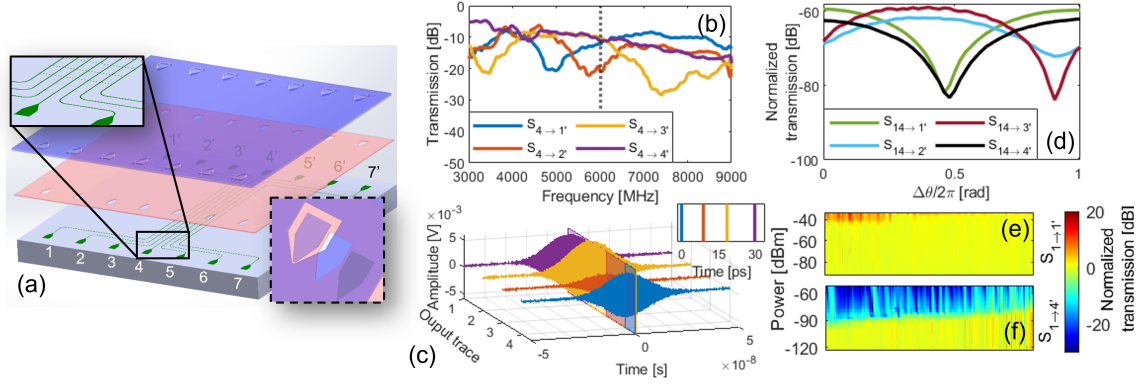


Figure 5.13: Characterization of the 7PTW as described in the main text. (a) Graphic representation, also illustrating the various layers of fabrication: Si substrate (grey), WSi (green), dielectric amorphous Si (pink) and Al (purple). Top-left corner inset: Zoom, showing traces and coupling lines. Bottom-right inset: Angled top view, showing the opening in Al and Si layers, fitting the launch pad of the WSi seen as shadow. (b) Transmission spectra for signals introduced in the center trace (trace no. 4). Broken line indicates frequency for the next experiment. This graph is presented with rolling averages of 150 MHz to eliminate ringing caused by minor reflections at connectors. (c) Measurement of wave packets with the central frequency f_4 , introduced in the center waveguide, perpendicular squares marking the center of the pulse, corrected for unequal launching traces. Inset: Zoom on the (time,amplitude)-plane analogue to the colored planes in the main figure. (d) Interference measurement: Measured transmission to ports 1'-4', as we split the CW input signal at $f_{1,4} = 5.12$ GHz between port 1 and 4, varying the phase difference and relative power input. (e) Simulation showing the power in the waveguides, as we apply a CW of frequency 6 GHz in the center trace.

the transmission due to nonlinearities. This effect is reproduced by our numerical simulation where non-linearities are present in the couplers only. As the power in the neighbor increases, the signals interfere, and the nonlinearity of the couplers quenches and phase shifts the highest-power signal outputs.

In the linear regime, the characteristic features of Fig. 5.12(a) such as the flat region at low frequencies and the alternating transmission peaks and dips, can be linked to the band structure of the corresponding periodic (infinitely extended) device. By plain simulations with the Kirchoff laws, the behaviour of this circuit can be recovered even without a deeper understanding of the underlying physics. In the full treatment in Appendix C, we find the eigenmodes of the 2CTW and show how the symmetries of the device determine its transmission spectra. When, for instance, the input is a symmetric combination of incoming waves, these will couple to the symmetric eigenmode, and the double-line decouples into two independent single-channel problems. These are effective Fabry-Perot scattering problems of the inputs and outputs coupling to the eigenmodes.

5.3.2 Seven Parallel Travelling Waveguides (7PTW)

Our next device is a generalization of the 2CTW with seven waveguides coupled mutually in a nearest-neighbor network, as portrayed in Fig. 5.13(a), which also visualizes the various layers of the fabrication scheme. In this device, we boost the couplers' Z_l further by removing the ground above them (not shown), hence minimizing their C_l which now resembles the capacitance of CPW. The performance of the 7PTW is tested by applying CW signals over a bandwidth of 6 GHz

in the center trace (no. 4) and by measuring the output, presented in Fig. 5.13(b). Here the broken vertical line marks the frequency $f_4 = 5.99$ GHz, chosen for the subsequent measurement, since there is significant, and equally strong, amplitude of transmission to most of the other ports (except port 2') at this frequency. We now replace the CW signal with short gaussian-shaped wave packets generated by side-band mixing control and again introduced in the center trace. Their arrival is detected at the output terminals of the device; it takes nanoseconds to transverse the network, but when subtracting the electrical delay, we register the arrival with a delay of $\sim 10\text{-}30$ ps (see inset of Fig. 5.13(c)), compared to the arrival of the first pulse at port 4'. In this figure, the smaller amplitude of the detected pulse at port 3' (shown in red) is consistent with the slightly smaller transmission through that specific trace at this frequency.

Returning to CW signals, we proceed at the frequency $f_{1,4} = 5.12$ GHz for which the eight transmissions ratios from ports 1 and 4 to ports 1'-4' (according to annotation of the ports in Fig. 5.13(a)) are all relatively high and similar in magnitude. Splitting the input power between the former two, we vary the relative phase and measure the output in Fig. 5.13(d). The nearly symmetrical interference patterns are due to similar transmission coefficients in the network (e.g. $4 \rightarrow 1'$ vs. $1 \rightarrow 4'$). Injection at port 4 has the possibility also to coherently diffuse to traces 5'-7', causing the slight asymmetries in Fig. 5.13(d).

We demonstrate the nonlinearity in the 7PTW emerging from the HKI of WSi by transmitting CW of increasing powers through chosen waveguides, starting at signals corresponding to an occupation of ~ 1 photons in the device. The frequency transmission spectra of the former, plotted in Figs. 5.13(e),(f) emphasize that the nonlinearity commences in the couplers before in the waveguides. The direct transmission $S_{1 \rightarrow 1'}$, is thus hardly affected until the highest excitations are reached and the signal is confined in the trace. Transmitting power from this waveguide to the center of the device (i.e. $1 \rightarrow 4'$) relies on couplers between all waveguides in between, resulting in the more power dependent $S_{1 \rightarrow 4'}$. The case of transmission through the central waveguide (trace 4, not plotted) differs from the two above: Despite again considering a coupler-free transmission path, this waveguide is connected to neighbors on either side, and hence it is more sensitive to the couplers' behaviour than trace 1.

The physics of the 7PTW is in principle not very different from the 2CTW. At least the inputs and outputs are still expected to couple to the eigenmodes of the device, and we can again find the latter by solving the numerous Kirchoff equations for the large network. The major difference between the behaviour of the two structures, due to the larger number of traces, is that the propagation of waves in the 7PMT can be associated with a coherent random walk rather than the

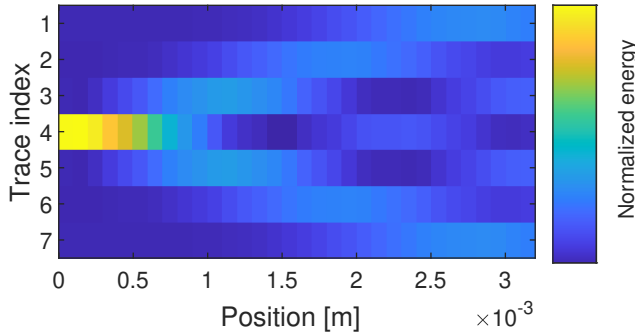


Figure 5.14: Simulation showing the power in the waveguides, as we apply a CW of frequency 6 GHz in the center trace.

more intuitive "hopping" between two traces⁶⁶.

With the current measurement method, where inputs are introduced in one end of the traces and the output is collected in the other end, we cannot specify the power distributions throughout the networks empirically. But our simulations (see Fig. 5.14) suggest that a random walk takes place within our network, just as has been demonstrated in other platforms [103–105].

The experiment with short microwave pulses, depicted in Fig. 5.13(c), adds value to this point. The pulses generally maintain the shape, as they transfer through the network. At other frequencies (cf. Fig. 5.13(b)) also the transmission to port 3' (shown in red in Figs. 5.13(b)-(c)) exits the structure with only very limited energy loss. This bodes well for implementations of routing experiments, where fast (strong) couplings are vital for information processing, and where energy loss can seriously harm the measurement.

The clear symmetry in the interference experiment (as shown in Fig. 5.13(d)) supports this statement. When the transmission $S_{14 \rightarrow 1'}$ (i.e. the output measured in port 1', when the input is split between ports 1 and 4) is almost identical with $S_{14 \rightarrow 4'}$, and $S_{14 \rightarrow 2'}$ strongly resembles $S_{14 \rightarrow 3'}$, it is because the coupling is roughly symmetric.

5.3.3 Two-dimensional Square Lattice (2DLS)

The third and final demonstration of the capabilities of SC microstrip WSi circuitry switches the focus from travelling to standing waves in a two-dimensional square lattice (2DLS) consisting of 49 microstrips, effectively acting as a multi-mode resonance cavity. Each microstrip resonator is $\sim 400 \mu\text{m}$ long and is coupled to four neighbors (two in either end as shown in Fig. 5.15(a)). The resonators in the two opposing corners of the 2DLS are capacitively coupled to coplanar transmission lines (see inset of Fig. 5.15(a)), terminated in large (0.3 mm wide) launch-pads, enabling excitation and measurement. Scanning CW the transmission spectrum (plotted in Fig. 5.15(b)) reveals three distinctive energy bands within the opera-

⁶⁶For this reason, we refer to the simple device of two lines as "two **coupled** travelling waveguides" and the more advanced version as "seven **parallel** travelling waveguides". In the former, the two traces are mutually coupled, whereas in the latter the couplings are "nearest neighbor" only.

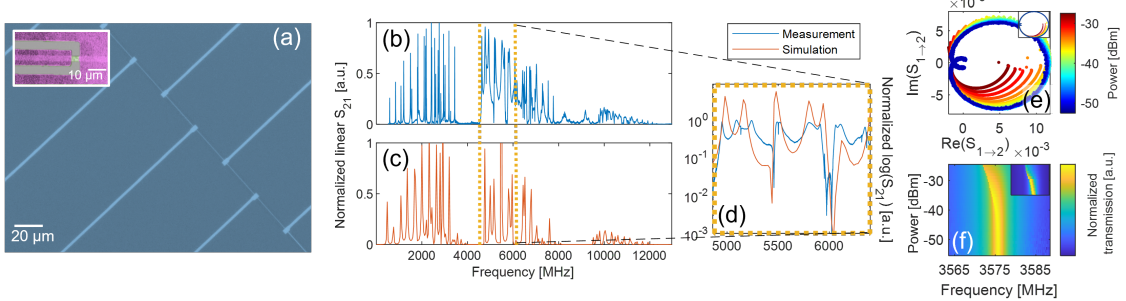


Figure 5.15: Characterization of the 2DSL. (a) Optical microscopy image (false colored), showing parts of wide microstrip resonators coupled with narrow couplers. Inset: SEM photo of coupling to input or readout with colors matching Fig. 5.13 (grey substrate and green WSi visible in the gap separating purple readout line from purple ground). Transmission vs. frequency normalized by the strongest response shown by (b) measurement and (c) simulation. For this device there are only two ports, 1 and 2. Here and elsewhere $S_{x \rightarrow y} = P_y / P_x$, where P_i is the power at port i . (d) Zoom on part of the spectrum joining (b) and (c). (e) Nonlinearity of the 2DSL measured by a polar representation of the transmission S_{21} in one of the peak frequencies from (b) (inset: simulation) and (f) magnitude of the transmission around the same peak frequency as shown in (e) (inset: simulation).

tional bandwidth of our readout-chain, comparable to the linear simulation (see Fig. 5.15(c)), which considers both dielectric loss and the transmission profile of attenuators, amplifiers, and circulators applied in the experiment. The simulation, similar in principle to that in Fig. 5.15(a) as it rests on the Kirchoff laws, also correctly draws out smaller features within the energy bands (Fig. 5.15(d)).

Also in the 2DSL nonlinearity is observed, when we introduce sufficiently strong powers and affect the resonance frequencies' phase and magnitude. This is exemplified in Figs. 5.15(d) and (e) respectively, and the results can be explained by a Duffing-type toy-model (which is integrated in the simulations, see insets in these figures).

Also in the two-dimensional square lattice a quantum walk can, in theory, be implemented. To see how this is possible, we re-write the state in which only the input resonator is excited (in the following described by the state $\chi(0)$) as a linear superposition of eigenmodes ψ_m in the second energy band in Fig. 5.15 (between 4-8 GHz). Driving such a single site excitation requires a large instantaneous

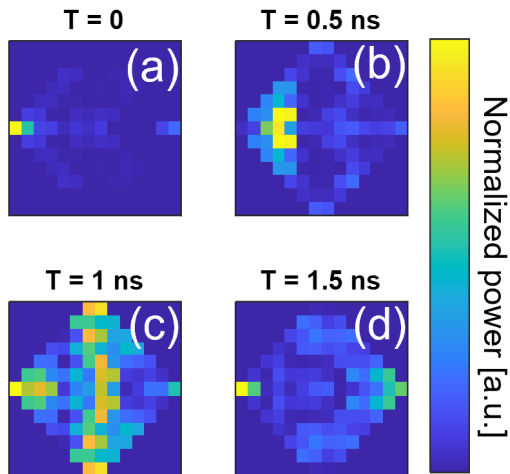


Figure 5.16: Simulated power propagation of the initial state mainly occupying the left-most resonator. Note that the energy scale in is normalized in each image according to the highest value (which slightly decreases due to loss effects).

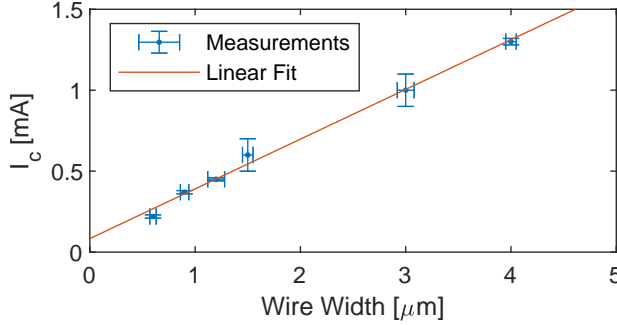


Figure 5.17: Critical current vs. width (proportional to cross section) of $\sim 11\text{-}13$ nm thick WSi wires. This graph was created from six different test-wires measured with DC current in two different cooldown-sessions.

bandwidth of about 1.5 GHz. This is beyond the current capabilities of our IQ mixers, but it would produce the energetic maps shown in Fig. 5.16 marked T=0. We numerically propagate the time-dependent state χ according to

$$\chi(t) = \sum_m \alpha_m \psi_m e^{-i\omega_m t} \quad (5.9)$$

where $\omega_m = 2\pi f_m$, with f_m being the frequency of the m 'th peak, and α_m are the superposition coefficients of $\chi(0)$. As the excitation evolves throughout the lattice (time dependent panels of Fig. 5.16), it preserves a certain degree of localization⁶⁷.

The 2DSL's geometry is closely related to that of photonic gratings employed to demonstrate a variety of many-body problems [106], such as quantum entanglement [107], interacting polaritons [108], and phase transitions of Mott-Insulators [109, 110].

A common, and very interesting feature of all three device (2CTW, 7PTW, and 2DSL) is the nonlinearity shown in Figs. 5.12(a), 5.13(e),(f), and 5.15(e),(f). According to Eq. (3.5), nonlinearity of the couplers arises at lower currents (and powers) than the nonlinearity of the $50\ \Omega$ matched waveguides. The kinetic inductance at low powers $L_{kin,0}$, is larger for the couplers (due to their smaller cross sections A), and so is the nonlinear term, $(I/I^*)^2$, since decreasing cross sections also lead to lower critical currents (see Fig. 5.17).

Our measurements span several orders of magnitude in power, starting from $P = -120$ dBm, which corresponds to an expectation of 0.2 photons within our device. This number is found as

$$N_{photons} = \frac{PL}{hfv_{ph}} \quad (5.10)$$

with h being Planck's constant, $f = 6$ GHz, and $L = 3$ mm the length of each of the 7PMT traces. Remarkably, the nonlinearity of the couplers confines the transmission in Fig. 5.13(f) at -90 dBm corresponding to only 200 photons. This is an extraordinarily low power for nonlinearity to arise, but non unlikely.

⁶⁷The imperfection of this simulation is partly, because only eigenmodes in the second energy band were included in the expansion of the single-site mode. In principle, the simulation could cover all eigenmodes, but that would require an even larger bandwidth of the IQ mixers. In this simulation we ignore dissipation effects.

In the next chapter, we will mention three wave-mixing as a possible future project. At this stage though, and closely connected to the advantages of three wave-mixing, we can imagine **tuning** the nonlinearity by applying strong waves ("pumps") far off-resonance from the signals to be transmitted in the experiment. This would push the couplers into their nonlinear regime, just as we witness in Fig. 5.13(e),(f).

Additional Experimental Data

In this chapter, we have reviewed the large amount of experimental results accumulated over the course of five years of research.

Naturally, not all projects I initiated (or to which I contributed) succeeded. In fact, some are still in progress by other students in our research group and include e.g. three wave-mixing in the amplifier and single photon detection with superconducting nano-wires. Preliminary data from these and other projects, also covering important conclusions from fabrication recipe development, appear in Chap. 6.

CHAPTER 6

Discussion and Outlook

In this chapter, we elaborate on the results presented above and discuss additional on-going research projects which, mainly due to time constraints, have not been completed yet. These projects are all based on the methods and/or experimental findings presented throughout the thesis and emphasizes the relevance of the research.

We conclude the chapter and thus the thesis' main text with a summary of the results and provide some perspectives of SC quantum optics.

6.1 Discussion of Results

6.1.1 Boson Sampling

Our proposal to implement boson sampling in SC networks was written in 2016. While our letter was in review for publication in *Physical Review Letters*, Ref. [111] was published with a similar proposal, but without the in-depth analysis of decoherence effect provided by us. This analysis was based on T_1 and T_φ characteristic of the time (presented in the former chapter), and promised the feasibility of implementing boson sampling in SC circuits in the near future.

In 2020, boson sampling was finally demonstrated in a network of SC resonators, but the purpose was the simulation of molecular vibronic spectra, and not quantum advantage. [112]. The latter had, as mentioned in the introduction, been demonstrated by Google in 2019 [16] in a random-sampling circuit of SC qubits, and in 2020 a Chinese group showed quantum advantage with boson sampling in an optical circuit [8].

In light of these scientific landmarks, it is obvious that proving quantum advantage with boson sampling in a SC circuit will not be ground breaking development for the quantum science community. In the contemporary research environment, where mainly innovative ideas and results are pursued, boson sampling must be redirected to serve alternative applications to justify its study. Fortunately, we do not have to look far for such applications.

The Hamiltonian describing the dynamics in the linear network, the Bose-Hubbard model, is also used in e.g. characterization of magnetic spin systems and the gas of interaction particles on an optical lattice (subject to minor changes in Eq. (4.1)) [113, 114].

It turns out that also the characteristic behaviour of molecules can be emulated by boson sampling. This includes both vibrations (and the consequent emission spectra) [115] and the docking of large molecules to receptors, which is important in the pharmaceutical industry for drug design [116]. And as we showed in our publication and discussed further Sec. 5.1.3, boson sampling devices can also be used for interferometry [26].

As such, our proposed system should be of interest to other disciplines in physics. Given the major improvements in the SC qubit qualities since the publication of our proposal [98, 99], there are likely numerous research fields that may benefit from SC microwave boson sampling.

6.1.2 Four-Wave Amplification

As the interest in SC circuits and its applications, and in particular in SC qubits, continue to grow, the need for reliable, low-noise microwave amplifiers will grow.

Fabricating a travelling wave parametric amplifier⁶⁸ for SC microwave signal is not an easy task. It includes the integration of several branches of natural science, the most important being microwave engineering, nonlinear optics, and superconductivity, but in the fabrication we also involved material science and chemistry. Our device overcomes many of the challenges met by earlier implementations and produces a bandwidth of ~ 2 GHz with amplification of $\sim 15 - 20$ dB. This is a bandwidth, somewhat narrower than Ref. [3], a pioneer in the field, but the amplification is ~ 10 dB stronger. And the "ringing" of the signal, i.e. the noise around the average transmission in *our* amplifier (see Fig. 5.8(a)) is only $\sim 1-2$ dB, whereas the spectrum of Ref. [3] is much noisier (~ 10 dB).

A special and important feature of our device is the length. The amplifier of Ref. [3] is more than a meter long, while we keep our microstrip limited to mere 11.6 cm. This is an advantage both for fabrication (which is more reliable for short devices) and for the packaging considerations, and shorter devices ensures limited dielectric loss effects.

The observation of an idler is not an insignificant outcome of the experiment, but a proof of the four wave-mixing taking place. Without an idler, one could wrongly assume the signal amplification spectrum to be the work of pump saturation; a strong pump saturating TLS's at f_s , which in turn would lead to intensified signals. Our simulations however, considering the loss effects, show that this is not the case, but the idler is experimental evidence of the four wave-mixing, and would not arise simply because of pump saturation.

Also the demonstrated noise temperature of around a single photon is an encouraging result, suggesting that the quantum limit is within reach, subject to design and fabrication improvements as proposed below. The uncertainty of the exact noise temperature can be reduced in a designated measurement, without attenuators, circulators, and additional components, necessary only for wave-mixing and high-power experiments⁶⁹.

There are many immediate questions, whose answers might boost the performance of our amplifier:

OPTIMAL PUMP FREQUENCY Around f_p the amplification is the strongest, and 7 GHz was chosen, after finding the associated amplification of the signal in a ± 1 GHz bandwidth stronger than e.g. $f_p = 6.4$ GHz, 6.7 GHz. But the chosen frequency is

⁶⁸Many places in the scientific literature, these devices are referred to as "TWPA's" (pronounced "TUPA").

⁶⁹In our current experimental setup such a measurement would require a cooldown with the amplifier solely for the purpose of measuring the noise temperature, and without further measurements with the device. For this reason we prioritized other projects

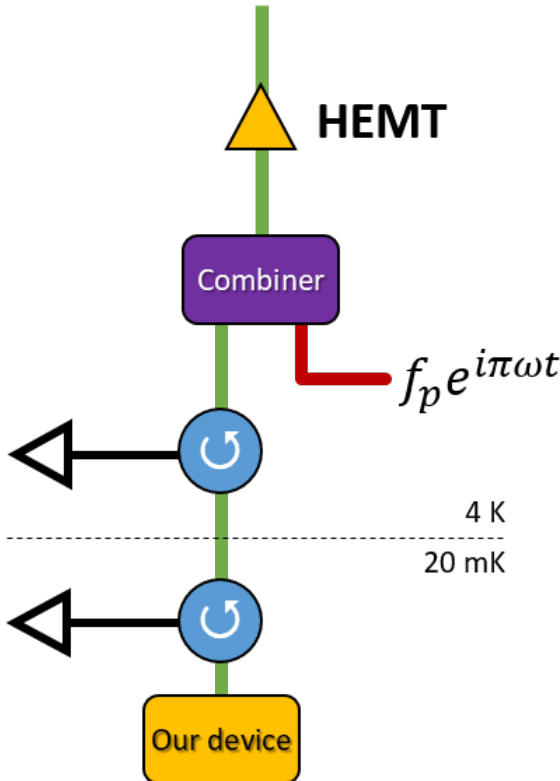


Figure 6.1: Strong pump powers can be applied to the device without damaging the HEMT by pump cancellation based on destructive interference. On the ordinary readout line (marked here in green), we add a combiner (purple) that merges the output from our device with a pump-cancelling signal (red). The frequency of the latter is chosen to equal f_p , and its phase is calibrated to be opposite that of the output emerging from the amplifier at f_p . The circulators (blue) are included in the readout constellation cf. Fig. 5.10 to avoid reflection back in to our device. In this way we allow the introduction of high-powered pumps to our device, without damaging the HEMT amplifier.

at the boundary of the operational bandwidth of the measurement chain⁷⁰, and this is assumed to be the reason for the rather sudden drop of the amplification profile in Fig. 5.8 at approximately 8 GHz. One could speculate that for higher values of f_p , we could accomplish even stronger amplifications, but that would require replacing several microwave components.

STRONGER PUMPS We are limited in the pump powers we apply to the amplifier for three reasons: 1) The signal generators have a maximal output, which is attenuated down through the measurement chain. 2) The HEMT amplifier at the 4K channel reaches its compression point at –10 GHz, and as a safety precaution, we do not exceed this value (to be absolutely sure not to cause damage to the amplifier). 3) We do not want to exceed the critical current of the device itself.

During our research, we discussed internally in the group to engineer what we called "pump cancellation" by merging the output of our device with an additional strong signal. The frequency of the pump-cancelling signal would be the same as the pump frequency, and would be applied *before* the HEMT. When mounted as depicted in Fig. 6.1, and with anti-phase matching, destructive interference would protect the HEMT, allowing the application of increasingly strong pumps to our device.

In practice, we did try out this idea experimentally, even though the anti-phase matching to ensure destructive interference was challenging, and had to be re-

⁷⁰Both combiners, circulators, and conventional amplifiers for the 4 K and the 300 K stages are only linear up to 8 GHz

peated frequently (during experiments) to ensure the safety of the HEMT. But even then, the highest pump powers that reached the amplifiers were $\lesssim 40$ dBm, due to the limited range of the generator. Such powers correspond to $0.1 \mu\text{W}$, or roughly $40 \mu\text{A}$ in a 50Ω matched waveguide. This is quite close the critical current⁷¹ of the device measured to $60 \mu\text{A}$.

ALTERNATIVE DIELECTRIC MATERIALS Our choice of amorphous Si as the dielectric was based on both the dielectric constant and the loss tangent of this material, as we described in Sec. 4.2.1. If too high, the impedance matching will require a capacitance not achievable with the current microstrip design⁷². Currently, however, the dielectric is responsible for the loss in the amplifier, so replacing the Si with a dielectric of lower $\tan \delta$ would be a major improvement to the current composition [117].

NARROWING THE AMPLIFIER Every working station, apparatus, sensor, and fabrication system has its boundaries, bandwidth, resolution etc., within which it functions smoothly. Outside this operational range, the given system is inefficient, and at the borders the user can often "push" the behaviour to extreme performance. With a $2\text{-}3 \mu\text{m}$ wide transmission line, the optical lithography is operated well within its own resolution. One can also fabricate reliable $\sim 1.5 \mu\text{m}$ wires⁷³, but mainly over short distances. When preparing micronic waveguides of more than a few mm, the focus of the laser writer usually changes a little (even with three-point-plane z-alignment). Small changes in the focal plane of the laser caused by inaccurate focusing alters the exact exposure dose of the resists, and eventually leads to changing widths of the waveguide. Over large areas of a bulk Si wafer, which might be slightly convex further adding to the problem, this naturally affects the impedance more, when the error is 1.4 instead of $1.5 \mu\text{m}$, then when 2.8 instead of $2.9 \mu\text{m}$. Unless alternative optical lithography systems (not tried out in this research) can provide a better resolution, the way forward is electronic lithography, which also offers much better alignment. Replacing the laser lithography with e-beam would benefit the impedance mismatched around the input launchers, where (due to the necessary tolerance) a few μm of the transmission line are not covered by Al to avoid shorting the line. On the other hand, e-beam lithography is much more time consuming than optical lithography.

⁷¹The critical current of our device is somewhat lower than what we expected based on its geometry. In other experiments, we fabricated test wires with various cross sections, and measured I_c for each, as plotted in Fig. 5.17. Yet, that graph is made for wires double as thick ($\sim 11\text{-}13 \text{ nm}$) as our microstrip amplifier, and when preparing an 11 cm long meandered transmission line only 5 nm thick, it is almost impossible to avoid local weak links, whose critical current affects I_c of the entire line.

⁷²This is, as described in Sec. 4.2.1 because we *must* require step coverage to avoid possible electrical contacts between ground and WSi waveguide.

⁷³This was demonstrated in dose tests and e.g. for the wires of Fig. 5.17.

Besides these impending questions, also more fundamental changes could be done to improve the amplifier's performance.

As we mentioned in Chap. 2, we attempted to implement dispersion engineering in our operation of the amplifier in its first few generations. This concept covers the situation where in, Eqs. (3.15), $\kappa = k_s + k_i - 2k_p > 0$. Our simulations assumed $\kappa = 0$ and were indeed consistent with our empirical observations. But those simulations relied on the assumption of a nearly linear transmission line, cf. Fig. 5.7, where the linear phase was $\sim 10^3\pi$. In this regime, the gain $\propto (k_p l)$, when $\kappa = 0$. However, to achieve the highest possible amplification in the *nonlinear* regime, we require the phase matching

$$2 \left(\frac{\alpha |A_p(0)|}{2I_*^2} \right) k_p \equiv 2\gamma k_p \stackrel{!}{=} \kappa \quad (6.1)$$

where we introduced the denotation γ , being the order of nonlinearity, which is related to the nonlinear phase shift $\phi = \gamma k_p z$. If Eq. (6.1) is valid, then the maximal gain possible is

$$G_s \approx \frac{e^{2\phi}}{4} \quad (6.2)$$

i.e. exponentially dependent on the amplifier's length [5]. Working with perfect phase matching is, at least **theoretically**, not beneficial for the amplification, because the application of the strong pump (and thus $\phi \geq 1$) in a dispersionless nonlinear Kerr medium is expected to generate Shock waves [118]. In fact, the nonlinear inductance includes higher order terms neglected in Eq. (3.3), e.g. the voltage $I^2(\partial I/\partial t)$. This causes the creation of the third harmonic of the pump, $3f_p$, which initializes the Shock wave. In Ref. [3] the dispersion is engineered by periodic broadening of the transmission. Such a geometry leads to band gaps in the transmission spectrum: In certain bandwidths the transmission is suppressed by $\sim 10^1\text{-}10^2$ dB. The width and length of the periodic broadening in such a manner that $3f_p$ falls within such a band gap, preventing its transmission.

But during experiments we never observed Shock wave generation, and we abandoned the broadenings. The width of the amplifier, whose results appear in Sec. 5.2, was kept constant throughout the 11.6 cm long meandered line.

6.1.3 Networks of Coupled Microstrips

The study of coupled travelling and standing waveguides (shown in Sec. 5.3) serves first and foremost as the "proof of concept" to show the wide horizons for experiments with the platform for microwave photonics with a strongly decreased v_{ph} .

The advantages of SC circuits includes both the efficient single-photon gener-

ation, the quite simple fabrication techniques for various designs with changing couplings, and the low loss⁷⁴. Nevertheless, a deeper insight on the specific experiments reveal rich physics even in the simple structures as we showed with simulations in Sec. 5.3, and which are further discussed in Appendix C.

There are multiple additional possibilities for practical applications of a SC microwave photonics platform. The next section mentions some of these and their relevance for contemporary physics research. Hopefully, other research groups in the field will adopt our methods for circuit engineering and perhaps even pursue alternative devices.

6.2 On-going Experiments

Here we briefly review projects currently in progress. These are either based directly or indirectly on the technologies and tools developed by the author of this thesis, and/or include his aid/guidance/fabrication skills. None of the results are considered mature for publication, but rather serve as inspiration for future students, and to demonstrate the large potential of SC circuits, and in particular HKI WSi.

6.2.1 Superconducting Nanowire Single-Photon Detector

BACKGROUND We have already mentioned that any sensor has a limited range of operation. However, the smallest quanta of energy is a photon, and a single-photon detector would thus be the ultimate sensor.

METHOD The Superconducting Nanowire Single-Photon Detector (SNSPD) is, as the name indicates, a submicronic wire. The absorption of a photon creates quasiparticles in the superconductor, which undergo scattering events, breaking Cooper pairs in a cascade of scattering events, and the bias current of the wire (pre-defined) is diverted away from the "epicenter": the position where the photon intersected the wire. The current density then rises, eventually surpassing the critical current, and the wire becomes resistive [119].

Other groups have already explored this technology, but as for the development of any detector, there are open research questions: How to improve sensitivity? Even if every photon *intersecting* the wire is detected, not every photon *intersects* the wire. How to limit dark counts? The rise and drop of the detection signal are proportional to L , the inductance, which as we have witnessed, is very high for WSi. It would therefore be interesting to develop an WSi SNSPD.

⁷⁴The loss in SC circuits is in general very limited, and can be reduced when fabrication is done with proper cleaning procedures. As mentioned elsewhere, the *dielectric* loss of our microstrips is still subject to research.

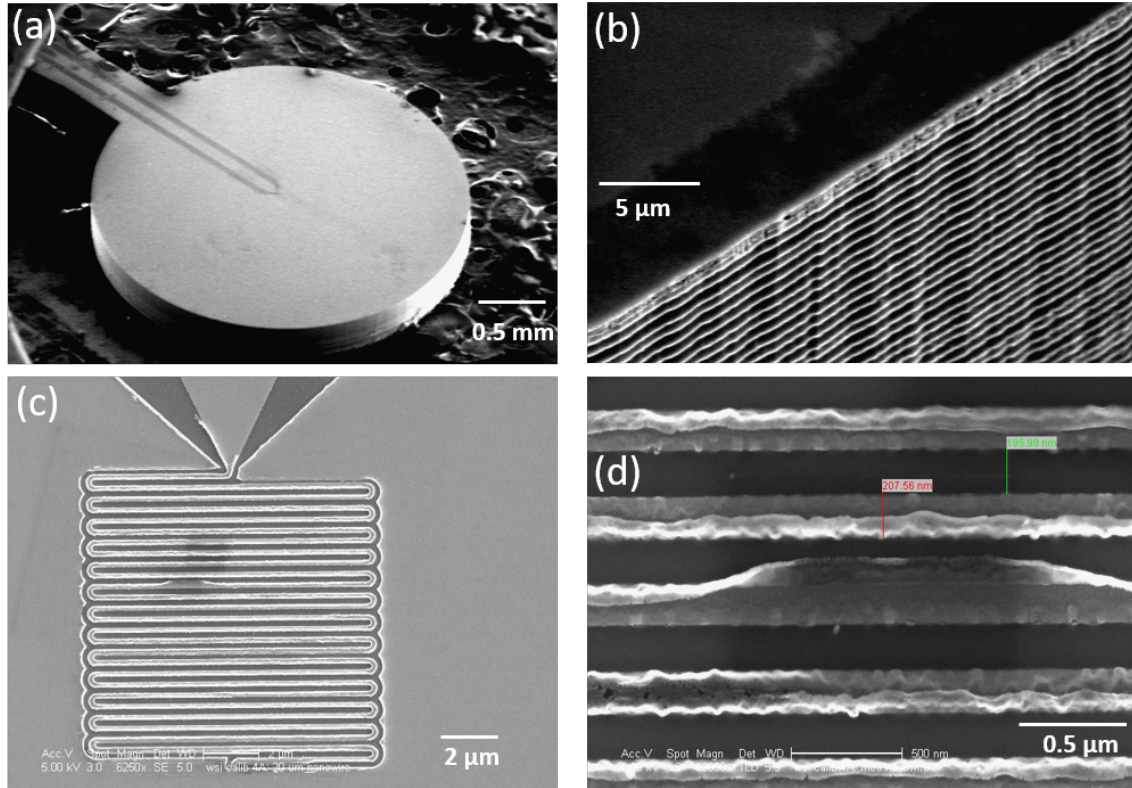


Figure 6.2: SEM images of the SNSPD based on WSi. (a) The "lollipop" shaped device. The geometry is chosen to fit at the bottom of a cylindrical tube fixing the optical fibre. The two long dark polygons are the gaps of the transmission line, terminating in the actual nanowire. (b) Edge of the SNSPD, cut by BOSCH process (at the Reactive Ion Etch station), since ordinary dicing is incompatible with the lollipop shape. (c) The nanowire is a meandered transmission line at the end of the transmission line. Importantly, the meandered structure is a dense area to optimize the probability of detection. (d) Zoom on a defect in (c). [37].

STATUS On Fig. 6.2 we show a prototype version of the WSi-based SNSPD. This project includes a number challenges, both technical (fabrication and measurement) and scientific. Many have been overcome over months of calibration of the fabrication process in the cleanroom, and in our dilution refrigerator we currently have an optical fibre going down to the base temperature plate for the purpose of this project. So far, however, experiments have not been successful.

6.2.2 The Hybrid Interdigitated Amplifier

BACKGROUND The Achilles heel of our travelling wave parametric amplifier is the dielectric material. Without it, the loss of the signal is expected to be significantly reduced. In the hybrid (WSi-Al) amplifier we aim to return to the CPW geometry and add capacitance along the transmission line, quite similar to the method of Ref. [4]. But we will do so with a much more limited capacitor area, limiting the vulnerability to fabrication flaws.

METHOD The novelty in our approach is the design and material of choice for the capacitor: Instead of a quasi-fractal capacitor with a very large area, we electrically shorten the WSi transmission line to the fingers of an interdigitated capacitor of

aluminum rather than of the HKI material (which in our case is WSi). This yields the extra capacitance per unit length required to reach $Z = 50 \Omega$, but does not add additional inductance.

STATUS As if this writing, we are progressing with the challenging fabrication of this device. We are planning a multi-step process, where alignment is critical to avoid shorts and to achieve values of C_l and Z as close to the design as possible.

6.2.3 Quantum Illumination

BACKGROUND Stealth technology is an advanced technology of modern warfare, making e.g. aircraft invisible to radars⁷⁵. The operational principle of conventional radars is to detect the reflection of some electromagnetic signal (wavelengths typically in the RF domain) from an object. By detection the radar confirms the object's existence, and estimates its position and velocity. It is of great concern to defense systems that stealth objects reflect only a very limited number of photons, such that the detected signal is below the noise level. Quantum illumination offers a solution to this problem⁷⁶ [120, 121].

METHOD The proposed idea⁷⁷ is to generate of pair of strongly correlated photons, store one (the "idler"), and emit the other (the "signal"). In this way, even when only a limited number of signal photons are reflected from the stealth object, they are "recognized" by the radar by virtue of the correlation to the idler. This is true even when the SNR-level is below unity [122]. For this detection scheme to work, we must generate many such photon pairs, and the no-cloning theorem forbids the actual entanglement⁷⁸ between the two modes [123]. But when the signal-idler pair is generated jointly, e.g. by down conversion of a pump as we have seen in the microstrip amplifier, their correlation might be stronger than for two random photons [124, 125]. In particular, Josephson Travelling Wave Parametric Amplifiers, such as that in Ref. [5], have been shown to generate signal-idler pairs compatible for exactly quantum illumination [126]. One could also imagine a strong correlation between the output ports of the 2CTW (in Fig. 5.12), when a pump is applied in one of the input ports.

STATUS So far, we have not attempted neither to simulate or experimentally implement quantum illumination in our lab.

⁷⁵Radio Detection and Raging.

⁷⁶In the eyes of the stealth attacker, quantum illumination is (as any asset on the battle field) obviously a serious problem rather than a solution.

⁷⁷So far, experimental quantum illumination has been successful in detected materials at the distance of ~ 1 m. The technique exists, but the way from the lab to commercial and military applications is long.

⁷⁸We have not described quantum entanglement in this thesis. In short, it is the strong correlation of e.g. two particles in such a way that mathematically, the state of one particle cannot be described independently of the other one.

6.2.4 Three Wave-Mixing and Squeezing

BACKGROUND The wave-mixing processes described throughout this thesis in the sections regarding the travelling-wave amplifier were degenerate four wave-mixing with $2\omega_p = \omega_s + \omega_i$. As already mentioned, this is not the only possible nonlinear process, and in general four wave-mixing can include two different pump tones, where $\omega_{p1} + \omega_{p2} = \omega_s + \omega_i$. A special case is three wave-mixing with a DC pump. One can relate to this as four wave-mixing, where the frequency of the second pump tone vanishes ($\omega_{p1} \rightarrow 0$), so that $\omega_{p2} = \omega_s + \omega_i$.

Even though the DC "tone" does not participate in the wave-mixing, it affects the kinetic inductance, when the amplitude of its current is sufficiently high. If so, the DC current is a shortcut: It allows calibrating L_{kin} without exaggerated pump power. In addition, it also removes the pump from the center of the transmission spectrum, avoiding saturation of the parasitic TLS's at the signal frequency (at least until the signal power is very strong and saturates the TLS's at f_s itself, and then amplification is unnecessary anyway). But most remarkably, the signal quadratures can be squeezed with the DC current.

METHOD The kinetic inductance per unit length of our transmission line given an RF pump and a DC pump, both assumed orders of magnitude stronger than the signal and idler, is:

$$L_{kin} \propto \left(\frac{I_{RF}^2 + 2I_{DC}I_{RF}}{I_*^2} \right) \quad (6.3)$$

The Kerr coefficient, on the other hand, is determined also by the wave number of the pump, k_p as:

$$\chi = \left(\frac{I}{I_*} \right)^2 \frac{k_p z}{t} \quad (6.4)$$

where t is time [127–129]. The interaction Hamiltonian describing non-degenerate amplification is $\mathcal{H}_i = -\frac{ik_p\chi}{2}(a_s a_i + a_s^\dagger a_i^\dagger)$ and the resulting (squeezed) quadratures of the voltage are given by [130]:

$$V(X_{1,2}, t) = e^{\pm 2\chi t} V(X_{1,2}, 0); \quad X_{1,2} \propto (a_s \pm a_i^\dagger) \quad (6.5)$$

Also the gain depends on the Kerr coefficient, as shown in Chap. 3, though χ was not explicitly named there⁷⁹.

STATUS So far, squeezed quadratures have been registered accompanied by a limited gain of 5-6 dB compared a control tone without DC-pumping. We have also succeeded in producing (preliminary) squeezed states.

⁷⁹Squeezing supposedly also appears in four wave-mixing processes, but there we neither control nor measure it.

6.2.5 Quantum Computation for Power Grid Control

BACKGROUND The orchestration of an electrical power grid is a complicated business, relying on the synchronization of thousands of transformer units connecting national power plants through high-voltage cables to the consumers⁸⁰. To ensure that as little energy is lost as possible, the grid must be organized with voltage phases accounting for phase velocities and distances. The large number of units in the grid makes the problem challenging and time-consuming for classical computers. Computation time is especially important, when a transformer station fails or a power cable disconnects, and the power distribution must be partly re-organized.

During the simulations of boson sampling, we considered whether a quantum computer, and in particular a boson sampling device could solve the problem stated here.

METHOD Despite several internal discussions and even a longer conversation with an electrical engineer from the Israeli Electrical Corporation, we did not reach a conclusive model to implement. Voltage amplitudes and phases could in principle be impersonated by the populations and relative phases of the modes in the boson sampling device. Alternatively, the probabilities and phases of the quantum states could be applied for the same purpose.

In both cases the question should be defined as an optimization problem, to reach the lowest possible loss.

RELATED RESEARCH Other groups have proposed quantum algorithms to solve this problem, though completely unrelated to boson sampling devices [131, 132]. These algorithms include e.g. neural networks [133], genetic algorithms [134], and adiabatic quantum computations [135]. Yet, as far as we know, no national power grid anywhere in the world is currently relying on quantum computations in their daily operation.

6.3 Thesis Summary

By the beginning of the third decade of the 21st century, SC circuits are both of interest for technological applications and fundamental research.

Through comprehensive simulations, we have shown how boson sampling can be realized in SC circuits to demonstrate a number of quantum phenomena despite decoherence effects. We have also introduced and analyzed the concept of interferometry with the boson sampling device, an operational scheme favoring Fock (quantum) states over coherent (classical) states.

⁸⁰In Israel, a relatively small country, the annual power consumption of around 60 GWh ($= 2.16 \times 10^{14} J$) is produced locally, and generally not imported. A completely different picture is drawn in the EU, where the "European high voltage transmission grid" distributes electricity to all member countries, and even certain non-members.

We have furthermore exploited the HKI superconductor WSi, and used its non-linearity to develop an impedance-matched microstrip travelling wave parametric amplifier, whose amplification exceeds 20 dB over > 2 GHz. These results agree with our numerical simulations. With an almost linear response over six orders of magnitude, and a sub-Kelvin noise temperature our amplifier benefits SC circuit readout protocols, especially with minor suggested improvements, expected to lower the dielectric loss.

Based on the v_{ph} in the amplifier (theoretically and empirically found to be two orders of magnitude slower than the value in typical SC Al waveguides), we have introduced a platform for on-chip microwave photonic experiments, capable of itinerant, routing, and interference dynamics; all these again consistent with simulations. The opportunities with our platform for SC microwave photonics reach beyond what we have shown here to include e.g. additional geometries, homodyne tomography, and multimode interferometry. Specific applications, subject to minor modifications of the devices, are scattershot boson-sampling [136], Hawking radiation [137], and reservoir-computing in neural networks [138].

6.4 Closing Remarks

Quantum optics and superconductivity are both relatively young research disciplines compared to other fields of physics. In the current rise of quantum technologies, dubbed the "second quantum revolution", quantum devices are commercialized, and many start-up companies in Israel and around the world are offering solutions based on quantum mechanics.

6.4.1 A personal viewpoint: The Future of Boson Sampling

The scientific community is not united in the belief in quantum advantage. While some researchers continue to enlarge and advance their circuits, apparently strengthening the argument for quantum advantage [112, 139, 140], other groups consistently aim to show that classical algorithms can reproduce at least some of the results in relatively short run times⁸¹ [17, 141, 142]. Scott Aaronson, who originally proposed to prove quantum advantage (and still refers to the idea as "supremacy") [2], is amongst the computer scientists who calls for⁸²

[...] a genuine dialogue between the 'quantum supremacists' and the classical skeptics: the former doing experiments and releasing all their data, the latter trying to design efficient classical simulations for those experiments, and so on in an iterative process.

⁸¹Certain classical algorithms are claimed to require a few months rather than thousands of years, as stated by the supporters of quantum advantage.

⁸²Quote from Scott Aaronson's blog [Shtetl Optimized](#) in a post from July 4, 2021 under the title "Open thread on new quantum supremacy claims". Retrieved on August 26, 2021.

While fact-based dialogues are usually fruitful for all participants, I disagree with this statement.

As of 2021, quantum physics in all its branches are making the leap from academic research to industrial technology. Quantum computation is part of this transition, and the need for proving quantum advantage is thus quite questionable. Certain scientists might still doubt the results claiming such proofs, and as humans by nature tend to be stubborn, their skepticism might not go away easily. But the second quantum revolution is "on the move" with funding, government support, educational programs, numerous start-up companies, and international competition. Applications, some still at the theoretical stage, others already implemented⁸³, do not await the approval of quantum advantage experiments. The few remaining serious obstacles on the path to efficient quantum computation with indisputable advantage over classical devices, e.g. error-correction [143], will hopefully be solved gradually in the near future. And as classically hard computations will be conducted with quantum computers, the interest in comparing the computation time with the world's strongest classical super-computers will be of low priority. Humanity can benefit much more from quantum computation by e.g. simulating complicated molecules for medical research and drug engineering than from proving quantum advantage to the 'skeptics'. And scientific research should, ideally, serve all of humanity, and not only the scientists.

The justification for research in boson sampling should therefore be based on its practical uses rather than the "proof of concept".

6.4.2 Superconducting Quantum Circuit Operation

When this research started, a typical question on SC quantum circuits was how to export the technology from the academic lab. Dilution refrigerators are expensive and require maintenance and can hardly be preserved by all potential users. But since then, the simple solution has become available: Remote operation of SC quantum systems by users, maintenance on site by engineers. This special situation makes the findings of this thesis most relevant: From the view of the engineer, the design of (inductively) coupled systems and the amplification schemes can greatly contribute to the infrastructure of the circuits. And from the user's point of view, the possible implementation of optics, routing, and nonlinear phenomena strongly widen the horizons of what can be done with SC systems.

⁸³An example of a quantum technology, not yet applicable, is "quantum money": The idea is to make money that cannot be counterfeit based on the no-cloning theorem [123]. But in the related field, banking, the fruits of quantum key distribution has allowed 100%-secured bank transfers.

Bibliography

- [1] Chong-Ki Hong, Zhe-Yu Ou, and Leonard Mandel. Measurement of subpicosecond time intervals between two photons by interference. *Physical review letters*, 59(18):2044, 1987.
- [2] Scott Aaronson and Alex Arkhipov. The computational complexity of linear optics. In *Proceedings of the forty-third annual ACM symposium on Theory of computing*, pages 333–342, 2011.
- [3] Byeong Ho Eom, Peter K Day, Henry G LeDuc, and Jonas Zmuidzinas. A wideband, low-noise superconducting amplifier with high dynamic range. *Nature Physics*, 8(8):623–627, 2012.
- [4] AA Adamyan, SE De Graaf, SE Kubatkin, and AV Danilov. Superconducting microwave parametric amplifier based on a quasi-fractal slow propagation line. *Journal of Applied Physics*, 119(8):083901, 2016.
- [5] TC White, JY Mutus, I-C Hoi, R Barends, B Campbell, Yu Chen, Z Chen, B Chiaro, A Dunsworth, E Jeffrey, et al. Traveling wave parametric amplifier with josephson junctions using minimal resonator phase matching. *Applied Physics Letters*, 106(24):242601, 2015.
- [6] Naftali Kirsh, Elisha Svetitsky, Alexander L Burin, Moshe Schechter, and Nadav Katz. Revealing the nonlinear response of a tunneling two-level system ensemble using coupled modes. *Physical Review Materials*, 1(1):012601, 2017.
- [7] Jianwei Wang, Fabio Sciarrino, Anthony Laing, and Mark G Thompson. Integrated photonic quantum technologies. *Nature Photonics*, 14(5):273–284, 2020.
- [8] Han-Sen Zhong, Hui Wang, Yu-Hao Deng, Ming-Cheng Chen, Li-Chao Peng, Yi-Han Luo, Jian Qin, Dian Wu, Xing Ding, Yi Hu, et al. Quantum computational advantage using photons. *Science*, 370(6523):1460–1463, 2020.
- [9] Alexis Morvan, Mathieu Féchant, Gianluca Aiello, Julien Gabelli, and Jérôme Estève. Bulk properties of honeycomb lattices of superconducting microwave resonators. *arXiv preprint arXiv:2103.09428*, 2021.
- [10] Clinton Bockstiegel, J Gao, MR Vissers, M Sandberg, S Chaudhuri, A Sanders, LR Vale, KD Irwin, and DP Pappas. Development of a broadband nbtin traveling wave parametric amplifier for mkid readout. *Journal of Low Temperature Physics*, 176(3):476–482, 2014.
- [11] Richard P Feynman. Simulating physics with computers. *Int. J. Theor. Phys.*, 21(6/7), 1982.
- [12] Stefano Pirandola, Ulrik L Andersen, Leonardo Banchi, Mario Berta, Darius Bunandar, Roger Colbeck, Dirk Englund, Tobias Gehring, Cosmo Lupo, Carlo Ottaviani, et al. Advances in quantum cryptography. *Advances in Optics and Photonics*, 12(4):1012–1236, 2020.
- [13] Richard Jozsa, Daniel S Abrams, Jonathan P Dowling, and Colin P Williams. Quantum clock synchronization based on shared prior entanglement. *Physical Review Letters*, 85(9):2010, 2000.
- [14] Christian L Degen, F Reinhard, and Paola Cappellaro. Quantum sensing. *Reviews of modern physics*, 89(3):035002, 2017.
- [15] R Di Candia, F Minganti, KV Petrovni, GS Paraoanu, and S Felicetti. Critical parametric quantum sensing. *arXiv preprint arXiv:2107.04503*, 2021.
- [16] Frank Arute, Kunal Arya, Ryan Babbush, Dave Bacon, Joseph C Bardin, Rami Barends, Rupak Biswas, Sergio Boixo, Fernando GSL Brandao, David A Buell, et al. Quantum supremacy using a programmable superconducting processor. *Nature*, 574(7779):505–510, 2019.
- [17] Yosef Rinott, Tomer Shoham, and Gil Kalai. Statistical aspects of the quantum supremacy demonstration. *arXiv preprint arXiv:2008.05177*, 2020.
- [18] David P DiVincenzo. Quantum computation. *Science*, 270(5234):255–261, 1995.
- [19] David G Cory, MD Price, W Maas, Emanuel Knill, Raymond Laflamme, Wojciech H Zurek, Timothy F Havel, and Shyamal S Somaroo. Experimental quantum error correction. *Physical Review Letters*, 81(10):2152, 1998.
- [20] Rainer Blatt and Christian F Roos. Quantum simulations with trapped ions. *Nature Physics*, 8(4):277–284, 2012.
- [21] Daniel Thomas Sank. *Fast, accurate state measurement in superconducting qubits*. PhD thesis, UC Santa Barbara, 2014.
- [22] William F Kindel, MD Schroer, and KW Lehnert. Generation and efficient measurement of single photons from fixed-frequency superconducting qubits. *Physical Review A*, 93(3):033817, 2016.
- [23] Christopher Gerry, Peter Knight, and Peter L Knight. *Introductory quantum optics*. Cambridge university press, 2005.
- [24] Girish S Agarwal. *Quantum optics*. Cambridge University Press, 2012.
- [25] C Grezes, Brian Julsgaard, Y Kubo, M Stern, T Umeda, J Isoya, H Sumiya, H Abe, S Onoda, T Ohshima, et al. Multimode storage and retrieval of microwave fields in a spin ensemble. *Physical Review X*, 4(2):021049, 2014.

- [26] Samuel Goldstein, Simcha Korenblit, Ydan Bendor, Hao You, Michael R Geller, and Nadav Katz. Decoherence and interferometric sensitivity of boson sampling in superconducting resonator networks. *Physical Review B*, 95(2):020502, 2017.
- [27] Saptarshi Chaudhuri, Jiansong Gao, and Kent Irwin. Simulation and analysis of superconducting traveling-wave parametric amplifiers. *IEEE Transactions on Applied Superconductivity*, 25(3):1–5, 2014.
- [28] Leonardo Ranzani, Mustafa Bal, Kin Chung Fong, Guilhem Ribéill, Xian Wu, Junling Long, H-S Ku, Robert P Erickson, David Pappas, and Thomas A Ohki. Kinetic inductance traveling-wave amplifiers for multiplexed qubit readout. *Applied Physics Letters*, 113(24):242602, 2018.
- [29] Jose Aumentado. Superconducting parametric amplifiers: The state of the art in josephson parametric amplifiers. *IEEE Microwave Magazine*, 21(8):45–59, 2020.
- [30] Andrew Addison Houck, DI Schuster, JM Gambetta, JA Schreier, BR Johnson, JM Chow, L Frunzio, J Majer, MH Devoret, SM Girvin, et al. Generating single microwave photons in a circuit. *Nature*, 449(7160):328–331, 2007.
- [31] He-Liang Huang, Dachao Wu, Daojin Fan, and Xiaobo Zhu. Superconducting quantum computing: a review. *Science China Information Sciences*, 63(8):1–32, 2020.
- [32] Jiansong Gao. *The physics of superconducting microwave resonators*. PhD thesis, California Institute of Technology, 2008.
- [33] Michael Tinkham. *Introduction to superconductivity*. Courier Corporation, 2004.
- [34] David M Pozar. *Microwave engineering*. John Wiley & Sons, 2011.
- [35] Robert P Erickson and David P Pappas. Theory of multiwave mixing within the superconducting kinetic-inductance traveling-wave amplifier. *Physical Review B*, 95(10):104506, 2017.
- [36] Zijun Chen, Anthony Megrant, Julian Kelly, Rami Barends, Joerg Bochmann, Yu Chen, Ben Chiaro, Andrew Dunsworth, Evan Jeffrey, JY Mutus, et al. Fabrication and characterization of aluminum airbridges for superconducting microwave circuits. *Applied Physics Letters*, 104(5):052602, 2014.
- [37] Uri Vool and Michel Devoret. Introduction to quantum electromagnetic circuits. *International Journal of Circuit Theory and Applications*, 45(7):897–934, 2017.
- [38] John M Martinis, Rami Barends, and Alexander N Korotkov. Calculation of coupling capacitance in planar electrodes. *arXiv preprint arXiv:1410.3458*, 2014.
- [39] Roman Mankowsky, Alaska Subedi, Michael Först, Simon O Mariager, Matthieu Chollet, HT Lemke, Jeffrey S Robinson, James M Glownia, Michael P Miniti, Alex Frano, et al. Nonlinear lattice dynamics as a basis for enhanced superconductivity in $\text{yba}_2\text{cu}_3\text{o}_6.5$. *Nature*, 516(7529):71–73, 2014.
- [40] Brian David Josephson. Possible new effects in superconductive tunnelling. *Physics letters*, 1(7):251–253, 1962.
- [41] KK Likharev. Superconducting weak links. *Reviews of Modern Physics*, 51(1):101, 1979.
- [42] Vladimir E Manucharyan, Jens Koch, Leonid I Glazman, and Michel H Devoret. Fluxonium: Single cooper-pair circuit free of charge offsets. *Science*, 326(5949):113–116, 2009.
- [43] Michael Metcalfe, E Boaknin, V Manucharyan, R Vijay, I Siddiqi, C Rigetti, L Frunzio, RJ Schoelkopf, and MH Devoret. Measuring the decoherence of a quantronium qubit with the cavity bifurcation amplifier. *Physical Review B*, 76(17):174516, 2007.
- [44] Andrew A Houck, Jens Koch, Michel H Devoret, Steven M Girvin, and Robert J Schoelkopf. Life after charge noise: recent results with transmon qubits. *Quantum Information Processing*, 8(2):105–115, 2009.
- [45] Alexandre Blais, Arne L Grimsmo, SM Girvin, and Andreas Wallraff. Circuit quantum electrodynamics. *arXiv preprint arXiv:2005.12667*, 2020.
- [46] Yasunobu Nakamura, Yu A Pashkin, and Jaw Shen Tsai. Coherent control of macroscopic quantum states in a single-cooper-pair box. *nature*, 398(6730):786–788, 1999.
- [47] AA Houck, JA Schreier, BR Johnson, JM Chow, Jens Koch, JM Gambetta, DI Schuster, L Frunzio, MH Devoret, SM Girvin, et al. Controlling the spontaneous emission of a superconducting transmon qubit. *Physical review letters*, 101(8):080502, 2008.
- [48] Werner Buckel and Reinhold Kleiner. *Superconductivity: fundamentals and applications*. John Wiley & Sons, 2008.
- [49] John Clarke and Alex I Braginski. *The SQUID handbook: Applications of SQUIDs and SQUID systems*. John Wiley & Sons, 2006.
- [50] Daniel A Steck. Quantum and atom optics, 2007.
- [51] Ying Wu and Xiaoxue Yang. Strong-coupling theory of periodically driven two-level systems. *Physical review letters*, 98(1):013601, 2007.
- [52] A Wallraff, DI Schuster, A Blais, L Frunzio, J Majer, MH Devoret, SM Girvin, and RJ Schoelkopf. Approaching unit visibility for control of a superconducting qubit with dispersive readout. *Physical review letters*, 95(6):060501, 2005.
- [53] Zijun Chen. *Metrology of quantum control and measurement in superconducting qubits*. PhD thesis, University of California, Santa Barbara, 2018.
- [54] Rami Barends, Julian Kelly, Anthony Megrant, Daniel Sank, Evan Jeffrey, Yu Chen, Yi Yin, Ben Chiaro, Josh Mutus, Charles Neill, et al. Coherent josephson qubit suitable for scalable quantum integrated circuits. *Physical review letters*, 111(8):080502, 2013.
- [55] H Dieter Zeh. On the interpretation of measurement in quantum theory. *Foundations of Physics*, 1(1):69–76, 1970.
- [56] Carmen Palacios-Berraquero, Leonie Mueck, and Divya M Persaud. Instead of ‘supremacy’ use ‘quantum advantage’. *Nature*, 576(7786):213–214, 2019.

- [57] Bryan T Gard, Keith R Motes, Jonathan P Olson, Peter P Rohde, and Jonathan P Dowling. An introduction to boson-sampling. In *From atomic to mesoscale: The role of quantum coherence in systems of various complexities*, pages 167–192. World Scientific, 2015.
- [58] Marvin Marcus and Henryk Minc. Permanents. *The American Mathematical Monthly*, 72(6):577–591, 1965.
- [59] Herbert John Ryser. *Combinatorial mathematics*, volume 14. American Mathematical Soc., 1963.
- [60] Albert Nijenhuis and Herbert S Wilf. *Combinatorial algorithms: for computers and calculators*. Elsevier, 2014.
- [61] Xuewei Niu, Shenghui Su, and Jianghua Zheng. A new fast computation of a permanent. In *IOP Conference Series: Materials Science and Engineering*, volume 790, page 012057. IOP Publishing, 2020.
- [62] Erich Kaltofen and Gilles Villard. On the complexity of computing determinants. *Computational complexity*, 13(3):91–130, 2005.
- [63] Vincenzo Tamma and Simon Laibacher. Multiboson correlation interferometry with arbitrary single-photon pure states. *Physical review letters*, 114(24):243601, 2015.
- [64] Alex Arkhipov and Greg Kuperberg. The bosonic birthday paradox. *Geometry & Topology Monographs*, 18(1):10–2140, 2012.
- [65] N Spagnolo, P Mataloni, R Ramponi, E Maiorino, DJ Brod, A Crespi, R Osellame, EF Galvao, L Sansoni, C Vitelli, et al. Experimental observation of the bosonic birthday paradox. *Phys. Rev. Lett.*, 111(arXiv: 1305.3188):130503, 2013.
- [66] Marco Bentivegna, Nicolò Spagnolo, Chiara Vitelli, Fulvio Flamini, Niko Viggianiello, Ludovico Latmiral, Paolo Mataloni, Daniel J Brod, Ernesto F Galvão, Andrea Crespi, et al. Experimental scattershot boson sampling. *Science advances*, 1(3):e1400255, 2015.
- [67] Kamil Brádler, Pierre-Luc Dallaire-Demers, Patrick Rebentrost, Daiqin Su, and Christian Weedbrook. Gaussian boson sampling for perfect matchings of arbitrary graphs. *Physical Review A*, 98(3):032310, 2018.
- [68] Craig S Hamilton, Regina Kruse, Linda Sansoni, Sonja Barkhofen, Christine Silberhorn, and Igor Jex. Gaussian boson sampling. *Physical review letters*, 119(17):170501, 2017.
- [69] Sonja Barkhofen, Tim J Bartley, Linda Sansoni, Regina Kruse, Craig S Hamilton, Igor Jex, and Christine Silberhorn. Driven boson sampling. *Physical review letters*, 118(2):020502, 2017.
- [70] Regina Kruse, Craig S Hamilton, Linda Sansoni, Sonja Barkhofen, Christine Silberhorn, and Igor Jex. Detailed study of gaussian boson sampling. *Physical Review A*, 100(3):032326, 2019.
- [71] Joseph W Britton, Brian C Sawyer, and Adam C Keith. C.-c. joseph wang, james k. freericks, hermann uys, michael j. biercuk, and john j. bollinger. Engineered twodimensional ising interactions in a trapped-ion quantum simulator with hundreds of spins. *Nature*, 484(7395):489–492, 2012.
- [72] Florian Schäfer, Takeshi Fukuhara, Seiji Sugawa, Yosuke Takasu, and Yoshiro Takahashi. Tools for quantum simulation with ultracold atoms in optical lattices. *Nature Reviews Physics*, 2(8):411–425, 2020.
- [73] Xiaoling Wu, Xinhui Liang, Yaoqi Tian, Fan Yang, Cheng Chen, Yong-Chun Liu, Meng Khoon Tey, and Li You. A concise review of rydberg atom based quantum computation and quantum simulation. *Chinese Physics B*, 2020.
- [74] Max Hofheinz, EM Weig, M Ansmann, Radoslaw C Bialczak, Erik Lucero, M Neeley, AD O’connell, H Wang, John M Martinis, and AN Cleland. Generation of fock states in a superconducting quantum circuit. *Nature*, 454(7202):310–314, 2008.
- [75] GS Paraoanu. Microwave-induced coupling of superconducting qubits. *Physical Review B*, 74(14):140504, 2006.
- [76] Robert W Boyd. The nonlinear optical susceptibility. *Nonlinear optics*, 3:1–67, 2008.
- [77] Matteo Staffaroni and Eli Yablonovitch. The role of kinetic inductance in metal optics. In *Quantum Electronics and Laser Science Conference*, page QThC1. Optical Society of America, 2011.
- [78] X Zhang, Andreas Engel, Q Wang, Andreas Schilling, Alexey Semenov, Maria Sidorova, H-W Hübers, Ilya Charaev, Konstantin Ilin, and Michael Siegel. Characteristics of superconducting tungsten silicide $w \times s \times 1 - x$ for single photon detection. *Physical Review B*, 94(17):174509, 2016.
- [79] Ralph W Klopfenstein. A transmission line taper of improved design. *Proceedings of the IRE*, 44(1):31–35, 1956.
- [80] Martin Göppel, A Fragner, M Baur, R Bianchetti, Stefan Filipp, Johannes M Fink, Peter J Leek, G Puebla, L Steffen, and Andreas Wallraff. Coplanar waveguide resonators for circuit quantum electrodynamics. *Journal of Applied Physics*, 104(11):113904, 2008.
- [81] AA Adamyan, SE Kubatkin, and AV Danilov. Tunable superconducting microstrip resonators. *Applied Physics Letters*, 108(17):172601, 2016.
- [82] William A Phillips. Two-level states in glasses. *Reports on Progress in Physics*, 50(12):1657, 1987.
- [83] Clemens Müller, Jared H Cole, and Jürgen Lisenfeld. Towards understanding two-level-systems in amorphous solids: insights from quantum circuits. *Reports on Progress in Physics*, 82(12):124501, 2019.
- [84] Alexander L Burin. Dipole gap effects in low energy excitation spectrum of amorphous solids. theory for dielectric relaxation. *Journal of low temperature physics*, 100(3):309–337, 1995.
- [85] Govind P Agrawal. Nonlinear fiber optics. In *Nonlinear Science at the Dawn of the 21st Century*, pages 195–211. Springer, 2000.
- [86] Till D Kühner and H Monien. Phases of the one-dimensional bose-hubbard model. *Physical Review B*, 58(22):R14741, 1998.
- [87] Michael A Nielsen and Isaac Chuang. Quantum computation and quantum information, 2002.

- [88] Jonas Evertsson, Florian Bertram, Fan Zhang, Lisa Rullik, LR Merte, Mikhail Shipilin, Markus Soldemo, Sareh Ahmadi, N Vinogradov, F Carlå, et al. The thickness of native oxides on aluminum alloys and single crystals. *Applied Surface Science*, 349:826–832, 2015.
- [89] Siaho Huang, Benjamin Lienhard, Greg Calusine, Antti Vepsäläinen, Jochen Braumüller, David K Kim, Alexander J Melville, Bethany M Niedzielski, Jonilyn L Yoder, Bharath Kannan, et al. Microwave package design for superconducting quantum processors. *PRX Quantum*, 2(2):020306, 2021.
- [90] Benjamin Lienhard, Jochen Braumüller, Wayne Woods, Danna Rosenberg, Greg Calusine, Steven Weber, Antti Vepsäläinen, Kevin O’Brien, Terry P Orlando, Simon Gustavsson, et al. Microwave packaging for superconducting qubits. In *2019 IEEE MTT-S International Microwave Symposium (IMS)*, pages 275–278. IEEE, 2019.
- [91] Jack H Richmond. Propagation on a ported coaxial cable buried in flat earth. *IEEE transactions on electromagnetic compatibility*, (2):70–76, 1985.
- [92] R Radebaugh and JD Siegwarth. Dilution refrigerator technology. *Cryogenics*, 11(5):368–384, 1971.
- [93] Yoni Prosper Shalibo. *Control and Measurement of Multi-Level States in the Josephson Phase Circuit*. Hebrew University of Jerusalem, 2012.
- [94] John M Martinis, Michel H Devoret, and John Clarke. Experimental tests for the quantum behavior of a macroscopic degree of freedom: The phase difference across a josephson junction. *Physical Review B*, 35(10):4682, 1987.
- [95] Philip Krantz, Morten Kjaergaard, Fei Yan, Terry P Orlando, Simon Gustavsson, and William D Oliver. A quantum engineer’s guide to superconducting qubits. *Applied Physics Reviews*, 6(2):021318, 2019.
- [96] Markus Ansmann. *Benchmarking the superconducting Josephson Phase Qubit: The violation of Bell’s inequality*. PhD thesis, University of California, Santa Barbara, 2009.
- [97] Josephine B Chang, Michael R Vissers, Antonio D Córcoles, Martin Sandberg, Jiansong Gao, David W Abraham, Jerry M Chow, Jay M Gambetta, Mary Beth Rothwell, George A Keefe, et al. Improved superconducting qubit coherence using titanium nitride. *Applied Physics Letters*, 103(1):012602, 2013.
- [98] Aaron Somoroff, Quentin Ficheux, Raymond A Mencia, Haonan Xiong, Roman V Kuzmin, and Vladimir E Manucharyan. Millisecond coherence in a superconducting qubit. *arXiv preprint arXiv:2103.08578*, 2021.
- [99] Alexander PM Place, Lila VH Rodgers, Pranav Mundada, Basil M Smitham, Matthias Fitzpatrick, Zhaoqi Leng, Anjali Premkumar, Jacob Bryon, Andrei Vrajitoarea, Sara Sussman, et al. New material platform for superconducting transmon qubits with coherence times exceeding 0.3 milliseconds. *Nature communications*, 12(1):1–6, 2021.
- [100] Yoni Shalibo, Roy Resh, Ofer Fogel, David Shwa, Radoslaw Bialczak, John M Martinis, and Nadav Katz. Direct wigner tomography of a superconducting anharmonic oscillator. *Physical review letters*, 110(10):100404, 2013.
- [101] Mordechai Segev, Yaron Silberberg, and Demetrios N Christodoulides. Anderson localization of light. *Nature Photonics*, 7(3):197–204, 2013.
- [102] Tal Schwartz, Guy Bartal, Shmuel Fishman, and Mordechai Segev. Transport and anderson localization in disordered two-dimensional photonic lattices. *Nature*, 446(7131):52–55, 2007.
- [103] Ben C Travaglione and Gerald J Milburn. Implementing the quantum random walk. *Physical Review A*, 65(3):032310, 2002.
- [104] Bereneice Sephton, Angela Dudley, Gianluca Ruffato, Filippo Romanato, Lorenzo Marrucci, Miles Padgett, Sandeep Goyal, Filippus Roux, Thomas Konrad, and Andrew Forbes. A versatile quantum walk resonator with bright classical light. *PloS one*, 14(4):e0214891, 2019.
- [105] Mohamed Hatifi, Giuseppe Di Molfetta, Fabrice Debbasch, and Marc Brachet. Quantum walk hydrodynamics. *Scientific reports*, 9(1):1–7, 2019.
- [106] Michael J Hartmann, Fernando GSL Brandao, and Martin B Plenio. Quantum many-body phenomena in coupled cavity arrays. *Laser & Photonics Reviews*, 2(6):527–556, 2008.
- [107] Jean-Michel Raimond, M Brune, and Serge Haroche. Manipulating quantum entanglement with atoms and photons in a cavity. *Reviews of Modern Physics*, 73(3):565, 2001.
- [108] Michael J Hartmann, Fernando GSL Brandao, and Martin B Plenio. Strongly interacting polaritons in coupled arrays of cavities. *Nature Physics*, 2(12):849–855, 2006.
- [109] Dieter Jaksch, Christoph Bruder, Juan Ignacio Cirac, Crispin W Gardiner, and Peter Zoller. Cold bosonic atoms in optical lattices. *Physical Review Letters*, 81(15):3108, 1998.
- [110] Jonas Larson, Bogdan Damski, Giovanna Morigi, and Maciej Lewenstein. Mott-insulator states of ultracold atoms in optical resonators. *Physical Review Letters*, 100(5):050401, 2008.
- [111] Borja Peropadre, Gian Giacomo Guerreschi, Joonsuk Huh, and Alán Aspuru-Guzik. Proposal for microwave boson sampling. *Physical review letters*, 117(14):140505, 2016.
- [112] Christopher S Wang, Jacob C Curtis, Brian J Lester, Yaxing Zhang, Yvonne Y Gao, Jessica Freeze, Victor S Batista, Patrick H Vaccaro, Isaac L Chuang, Luigi Frunzio, et al. Efficient multiphoton sampling of molecular vibronic spectra on a superconducting bosonic processor. *Physical Review X*, 10(2):021060, 2020.
- [113] Dieter Jaksch and Peter Zoller. The cold atom hubbard toolbox. *Annals of physics*, 315(1):52–79, 2005.
- [114] SR Clark and Dieter Jaksch. Signatures of the superfluid to mott-insulator transition in the excitation spectrum of ultracold atoms. *New Journal of Physics*, 8(8):160, 2006.
- [115] Joonsuk Huh, Gian Giacomo Guerreschi, Borja Peropadre, Jarrod R McClean, and Alán Aspuru-Guzik. Boson sampling for molecular vibronic spectra. *Nature Photonics*, 9(9):615–620, 2015.
- [116] Leonardo Banchi, Mark Fingerhuth, Tomas Babej, Christopher Ing, and Juan Miguel Arrazola. Molecular docking with gaussian boson sampling. *Science advances*, 6(23):eaax1950, 2020.

- [117] Benjamin A Mazin, Daniel Sank, Sean McHugh, Erik A Lucero, Andrew Merrill, Jiansong Gao, David Pappas, David Moore, and Jonas Zmuidzinas. Thin film dielectric microstrip kinetic inductance detectors. *Applied Physics Letters*, 96(10):102504, 2010.
- [118] Rolf Landauer. Shock waves in nonlinear transmission lines and their effect on parametric amplification. *IBM Journal of Research and Development*, 4(4):391–401, 1960.
- [119] Chandra M Natarajan, Michael G Tanner, and Robert H Hadfield. Superconducting nanowire single-photon detectors: physics and applications. *Superconductor science and technology*, 25(6):063001, 2012.
- [120] Si-Hui Tan, Baris I Erkmen, Vittorio Giovannetti, Saikat Guha, Seth Lloyd, Lorenzo Maccone, Stefano Pirandola, and Jeffrey H Shapiro. Quantum illumination with gaussian states. *Physical review letters*, 101(25):253601, 2008.
- [121] Shabir Barzanjeh, Saikat Guha, Christian Weedbrook, David Vitali, Jeffrey H Shapiro, and Stefano Pirandola. Microwave quantum illumination. *Physical review letters*, 114(8):080503, 2015.
- [122] Ranjith Nair and Mile Gu. Fundamental limits of quantum illumination. *Optica*, 7(7):771–774, 2020.
- [123] Vladimir Bužek and Mark Hillery. Quantum copying: Beyond the no-cloning theorem. *Physical Review A*, 54(3):1844, 1996.
- [124] Rafi Vered, M Rosenbluh, and A Pe’er. *Two-photon correlations of broadband four wave mixing*. IEEE, 2011.
- [125] Rafi Z Vered, Yaakov Shaked, Yelena Ben-Or, Michael Rosenbluh, and Avi Pe’er. Classical-to-quantum transition with broadband four-wave mixing. *Physical review letters*, 114(6):063902, 2015.
- [126] Luca Fasolo, Angelo Greco, Emanuele Enrico, Fabrizio Illuminati, Rosario Lo Franco, David Vitali, and Patrizia Livreri. Josephson travelling wave parametric amplifiers as non-classical light source for microwave quantum illumination. *arXiv preprint arXiv:2106.00522*, 2021.
- [127] John Kerr. A new relation between electricity and light: dielectric media birefringent (second paper). *Philosophical Magazine*, S. 4, 50(333):446–458, 1875.
- [128] Mike Melnichuk and Lowell T Wood. Direct kerr electro-optic effect in noncentrosymmetric materials. *Physical Review A*, 82(1):013821, 2010.
- [129] Jing Xu, George SD Gordon, Timothy Wilkinson, and Christophe Peucheret. Experimental observation of non-linear mode conversion in few-mode fiber. In *CLEO: Science and Innovations*, pages SM2L–3. Optical Society of America, 2015.
- [130] Daniel F Walls and Gerard J Milburn. *Quantum optics*. Springer Science & Business Media, 2007.
- [131] Akshay Ajagekar and Fengqi You. Quantum computing for energy systems optimization: Challenges and opportunities. *Energy*, 179:76–89, 2019.
- [132] Rozhin Eskandarpour, Pranav Gokhale, Amin Khodaei, Frederic T Chong, Aleksi Passo, and Shay Bahramirad. Quantum computing for enhancing grid security. *IEEE Transactions on Power Systems*, 35(5):4135–4137, 2020.
- [133] Chao Liu, ZY He, and JW Yang. A quantum neural network based fault diagnosis algorithm for power grid. *Power System Technology*, 32(9):56–60, 2008.
- [134] Jia-Chu Lee, Wei-Min Lin, Gwo-Ching Liao, and Ta-Peng Tsao. Quantum genetic algorithm for dynamic economic dispatch with valve-point effects and including wind power system. *International Journal of Electrical Power & Energy Systems*, 33(2):189–197, 2011.
- [135] MW Johnson, P Bunyk, F Maibaum, E Tolkacheva, AJ Berkley, EM Chapple, R Harris, J Johansson, T Lanting, I Perminov, et al. A scalable control system for a superconducting adiabatic quantum optimization processor. *Superconductor Science and Technology*, 23(6):065004, 2010.
- [136] Ludovico Latmiral, Nicolò Spagnolo, and Fabio Sciarrino. Towards quantum supremacy with lossy scattershot boson sampling. *New Journal of Physics*, 18(11):113008, 2016.
- [137] PD Nation, MP Blencowe, AJ Rimberg, and E Buks. Analogue hawking radiation in a dc-squid array transmission line. *Physical review letters*, 103(8):087004, 2009.
- [138] Gerasimos Angelatos, Saeed Khan, and Hakan E Türeci. Reservoir computing approach to quantum state measurement. *arXiv preprint arXiv:2011.09652*, 2020.
- [139] Han-Sen Zhong, Yu-Hao Deng, Jian Qin, Hui Wang, Ming-Cheng Chen, Li-Chao Peng, Yi-Han Luo, Dian Wu, Si-Qiu Gong, Hao Su, et al. Phase-programmable gaussian boson sampling using stimulated squeezed light. *arXiv preprint arXiv:2106.15534*, 2021.
- [140] Dmitri Maslov, Jin-Sung Kim, Sergey Bravyi, Theodore J Yoder, and Sarah Sheldon. Quantum advantage for computations with limited space. *Nature Physics*, pages 1–4, 2021.
- [141] Alex Neville, Chris Sparrow, Raphaël Clifford, Eric Johnston, Patrick M Birchall, Ashley Montanaro, and Anthony Laing. Classical boson sampling algorithms with superior performance to near-term experiments. *Nature Physics*, 13(12):1153–1157, 2017.
- [142] Wojciech Roga and Masahiro Takeoka. Classical simulation of boson sampling with sparse output. *Scientific reports*, 10(1):1–7, 2020.
- [143] Barbara M Terhal, Jonathan Conrad, and Christophe Vuillot. Towards scalable bosonic quantum error correction. *Quantum Science and Technology*, 5(4):043001, 2020.
- [144] GA Miller. On the history of determinants. *The American Mathematical Monthly*, 37(5):216–219, 1930.
- [145] DA Kleinman. Theory of second harmonic generation of light. *Physical Review*, 128(4):1761, 1962.
- [146] Oded Yaakobi, Lazar Friedland, Chris Macklin, and Irfan Siddiqi. Parametric amplification in josephson junction embedded transmission lines. *Physical Review B*, 87(14):144301, 2013.
- [147] SM Anlage, HJ Snortland, and MR Beasley. A current controlled variable delay superconducting transmission line. *IEEE Transactions on Magnetics*, 25(2):1388–1391, 1989.
- [148] Fritz London and Heinz London. The electromagnetic equations of the supraconductor. *Proceedings of the Royal Society of London. Series A-Mathematical and Physical Sciences*, 149(866):71–88, 1935.

Appendices

A: Mathematical Derivations

Gaussian Elimination ("Row Reduction")

Chap. 2 discussed the boson sampling paradigm. In this context we mentioned that it is harder to classically compute a permanent than a determinant. Here we elaborate on this proposition.

Gaussian elimination is useful method for reducing the number of terms in the computation of a determinant. Suppose we are concerned with the determinant of a matrix A :

$$A = \begin{pmatrix} a_{11} & a_{12} & \cdots & a_{1n} \\ \vdots & \vdots & & \vdots \\ b_{q1} & b_{q2} & \cdots & b_{qn} \\ \vdots & \vdots & \ddots & \vdots \\ a_{m1} & a_{m2} & \cdots & a_{mn} \end{pmatrix}$$

We now exploit the fact that the determinant is a linear operation. In other words, we can write

$$|A| = \left| \begin{array}{cccc} a_{11} & a_{12} & \cdots & a_{1n} \\ \vdots & \vdots & & \vdots \\ 0 & b_{q2} - \frac{b_{q1}}{a_{11}} & \cdots & b_{qn} - \frac{b_{q1}}{a_{11}} \\ \vdots & \vdots & \ddots & \vdots \\ a_{m1} & a_{m2} & \cdots & a_{mn} \end{array} \right| + \frac{b_{q1}}{a_{11}} \left| \begin{array}{cccc} a_{11} & a_{12} & \cdots & a_{1n} \\ \vdots & \vdots & & \vdots \\ a_{11} & a_{12} & \cdots & a_{1n} \\ \vdots & \vdots & \ddots & \vdots \\ a_{m1} & a_{m2} & \cdots & a_{mn} \end{array} \right| \quad (\text{A1})$$

We now note that the last term (marked in green) has two identical rows. Generally, when this is the case, we can swap the two rows without changing the matrix. But the determinant is also described by the Leibniz formula [144]:

$$\det(A) = \sum_{\sigma \in S_n} \text{sign}(\sigma) \prod_i^n a_{i,\sigma} \quad (\text{A2})$$

where S_n is the permutations of the matrix elements a . When rows are swapped, the permanent sign switches, and it follows that $\det(A) = -\det(A)$, so $\det(A) = 0$. Unlike the original computational problem of finding the determinant A , the remaining term of Eq. (A1) (marked in purple) includes a zero. This reduces the number of terms in the determinant, and thus the computation time.

Gaussian Elimination is not possible for permanents. The permanent is, similar to the determinant, a linear operation of the matrix, so

$$\text{per}(A) = \text{per} \left(\begin{array}{cccc} a_{11} & a_{12} & \cdots & a_{1n} \\ \vdots & \ddots & & \vdots \\ 0 & b_{q2} - \frac{b_{q1}}{a_{11}} & \cdots & b_{qn} - \frac{b_{q1}}{a_{11}} \\ \vdots & & \ddots & \vdots \\ a_{m1} & a_{m2} & \cdots & a_{mn} \end{array} \right) + \frac{b_{q1}}{a_{11}} \cdot \text{per} \left(\begin{array}{cccc} a_{11} & a_{12} & \cdots & a_{1n} \\ \vdots & \ddots & & \vdots \\ a_{11} & a_{12} & \cdots & a_{1n} \\ \vdots & & \ddots & \vdots \\ a_{m1} & a_{m2} & \cdots & a_{mn} \end{array} \right) \quad (\text{A3})$$

But the sign-function of Eq. (A2) does not appear in the equivalent Leibniz formula for the permanent:

$$\text{per}(A) = \sum_{\sigma \in S_n} \prod_i^n a_{i,\sigma} \quad (\text{A4})$$

and the right-most permanent of Eq. (A4) (in green) remains. The complexity has therefore *not* been reduced after excluding the permanent of the green matrix from $\text{per}(A)$.

Alternatively, one can also show that while $\det(AB) = \det(A)\det(B)$ for two matrices A and B , $\text{per}(AB) \neq \text{per}(A)\text{per}(B)$.

In general, this demonstrates how determinants can be computed faster than permanents.

The Coupled Mode Equations

In Chap. 3 we presented the coupled-mode equations (Eqs. (3.15)), describing the wave-mixing in our microstrip amplifier. We do not derive them rigorously; such a derivation is space-consuming and lies outside the scope of this work (for full derivations, see Ref. [76] or [85]). Instead, we will only briefly outline the origin of the equations and elaborate on the significance of their different terms.

In nonlinear fibre optics, Kleinmann symmetry [145] prescribes that the presence of two electric fields generates the frequency-dependent polarization:

$$P_3(\omega_3) = 4\epsilon_0 d_{eff} E_1(\omega_1) E_2(\omega_2) \quad (\text{A5})$$

with d_{eff} being the effective dipole moment. The polarization adds an extra term in the ordinary wave-equation:

$$\nabla^2 E_n - \frac{\epsilon_r}{c^2} \frac{\partial^2 E_n}{\partial t^2} = \frac{1}{\epsilon_0 c^2} \frac{\partial^2 P_n}{\partial t^2} \quad (\text{A6})$$

This extra term is responsible for the nonlinearity, as we found in Eq. (3.7). In Eq. (A6) c is the vacuum speed of light, ϵ_0 the vacuum permittivity, and ϵ_r the relative permittivity (dielectric constant). Here we deal with three modes at frequencies ω_1 , ω_2 , and ω_3 . We will assume a plane wave at frequency ω_n , i.e.

$$E_n = A_n e^{i(k_n z - \omega_n t)} + \text{c.c.}$$

where A_n is a complex amplitude. With this ansatz, we replace $\nabla^2 \rightarrow \frac{d^2}{dz^2}$. It follows that for E_3 :

$$\left(\frac{d^2 A_3}{dz^2} + 2ik_3 \frac{dA_3}{dz} - k_3^2 A_3 + \frac{\epsilon \omega_3^2 A_3}{c^2} \right) e^{i(k_3 z - \omega_3 t)} + \text{c.c.} = -\frac{4d_{eff}\omega_3^2}{c^2} A_1 A_2 e^{i((k_1 + k_2)z - i\omega_3 t)} + \text{c.c.} \quad (\text{A7})$$

We now use that $k_3^2 = \epsilon \omega_3^2 / c^2$. In general $\epsilon = \epsilon(\omega)$, but we will ignore this frequency dependence for now. Eq. (A7) then becomes

$$\frac{d^2 A_3}{dz^2} + 2ik_3 \frac{dA_3}{dz} = -\frac{4d_{eff}\omega_3^2}{c^2} A_1 A_2 e^{i((k_1 + k_2 - k_3)z - i\omega_3 t)} \quad (\text{A8})$$

Finally, we use the Eq. (3.14) to neglect the first term in Eq. (A8) yielding:

$$\frac{dA_3}{dz} = \frac{2id_{eff}\omega_3^2}{k_3 c^2} A_1 A_2 e^{i\kappa z} \quad (\text{A9})$$

Here we introduced the phase mismatch, $\kappa = k_1 + k_2 - k_3$. Under similar derivations, we can produce equations for the two other modes:

$$\frac{dA_1}{dz} = \frac{2id_{eff}\omega_1^2}{k_1 c^2} A_2^* A_3 e^{-i\kappa z} \quad (\text{A10a})$$

$$\frac{dA_2}{dz} = \frac{2id_{eff}\omega_2^2}{k_2 c^2} A_1^* A_3 e^{-i\kappa z} \quad (\text{A10b})$$

Eqs. (A9),(A10) resemble the coupled-mode equations as presented in Eqs. (3.15) to a large extend, given the material-dependent pre-factor

$$\frac{2d_{eff}\omega_n^2}{k_n c^2} = \frac{k_n \alpha}{2I_*^2}$$

used to define I_* . However, Eqs. (3.15) include more than one term on their right-hand-side. These are other "polarization terms", e.g. as we see for the propagation of the pump in Eq. (3.15a): The first term ($|A_p|^2 A_p$) describes dipole from interference between pump photons only (self-modulation). The second term with the factor $|A_s|^2 A_p$ covers the case of interference between signal and pump photons, the third term between *idler* and pump photons, and the last between all three.

Why is the pump different from the signal and the idler in Eqs. (3.15)? Even before assuming $|A_p| \gg |A_s|, |A_i|$, we notice the asymmetry of the last term, always including the factor $|A_p|$. This follows from the fact that we relate to degenerate four-wave mixing only throughout most of this thesis. The $|A_p|$ on the right-hand-side of all the coupled-mode-equations can therefore be considered the amplitude of the other pump tones at the same frequency, when the first is differentiated at the left-hand-side.

Perturbative Solution to the Coupled Mode Equations

As stated in Chap. 3, the coupled mode equations can be solved analytically under a few approximations. The derivation in this section follows Ref. [5].

We first remember the solution for the pump amplitude from Eq. (3.17):

$$A_p(z) = A_p(0) \exp\left(\frac{ik_p \alpha |A_p(0)|^2}{2I_*^2}\right) \equiv A_p(0) e^{i\phi}$$

This solution is based on a number of approximations as stated in Ch3. With this in hand, only the signal and the idler have to be solved. From Eq. (3.16) we have:

$$\frac{\partial A_s}{\partial z} = \frac{ik_s \alpha}{2I_*^2} \left(2|A_p|^2 A_s + A_i^* A_p^2 e^{-i\kappa z} \right) \quad (\text{A11a})$$

$$\frac{\partial A_i^*}{\partial z} = \frac{ik_i \alpha}{2I_*^2} \left(2|A_p|^2 A_i^* + A_s A_p^2 e^{-i\kappa z} \right) \quad (\text{A11b})$$

where we took the complex conjugate of the second equation. We can now write these equations as a matrix:

$$\begin{pmatrix} \partial_z A_s \\ \partial_z A_i^* \end{pmatrix} = \frac{i\alpha}{2I_*^2} \begin{pmatrix} 2k_s |A_p(0)|^2 & A_p^2 e^{2i\phi - i\kappa z} \\ A_p^2 e^{2i\phi - i\kappa z} & 2k_i |A_p(0)|^2 \end{pmatrix} \begin{pmatrix} A_s \\ A_i^* \end{pmatrix} \quad (\text{A12})$$

Assuming perfect phase-matching, i.e. $\kappa = 2k_p - k_s - k_i = 0$ and that $A_p(0) = |A_p(0)|$, our matrix becomes somewhat more simple:

$$\begin{pmatrix} \partial_z A_s \\ \partial_z A_i^* \end{pmatrix} = \frac{i\alpha |A_p(0)|^2}{2I_*^2} \begin{pmatrix} 2k_s & e^{2i\phi} \\ e^{2i\phi} & 2k_i \end{pmatrix} \begin{pmatrix} A_s \\ A_i^* \end{pmatrix} \quad (\text{A13})$$

but the matrix includes ϕ , and is therefore still a function of z . Defining $\vec{A} = (A_s, A_i^*)$, and by elementary perturbation theory $(\vec{A}(z + dz) \simeq \vec{A}(z) + \partial_z \vec{A}(z) dz)$ we can re-define the problem. Instead of solving the two coupled first-order Eqs. (A13), we can now explicitly write $A_s(z)$:

$$\begin{pmatrix} A_s(z) \\ A_i^*(z) \end{pmatrix} = \begin{pmatrix} A_s(0) \\ A_i^*(0) \end{pmatrix} + \frac{i\alpha |A_p(0)|^2}{2I_*^2} \begin{pmatrix} 2k_s & e^{2i\phi} z \\ e^{2i\phi} & 2k_i \end{pmatrix} \begin{pmatrix} A_s(z) \\ A_i^*(z) \end{pmatrix} \equiv \mathbf{M} \begin{pmatrix} A_s(0) \\ A_i^*(0) \end{pmatrix} \quad (\text{A14})$$

In the linear regime, when $\omega_p \simeq \omega_s$, we also have $k_p \simeq k_s$. The gain defined in Eq. (3.18) then

approximately becomes [3,5,27,146]:

$$G \simeq 1 + \left(\frac{ik_p\alpha|A_p(0)|^2z}{2I_\star^2} \right)^2 = 1 + \phi^2 \quad (\text{A15})$$

We again emphasize the main assumption to reach this result: $\kappa = 2k_p - k_s - k_i = 0$. While this indeed leads to the quadratic gain in Eq. (A15), dispersion engineering can under certain conditions produce exponential gain profiles, i.e. with $G_s \simeq \frac{1}{4}e^{2\phi}$. Since we do not observe this regime experimentally, we refrain from further elaborating on the topic.

Taylor Expansion of the Xmon Hamiltonian

As defined in Eq. (2.27), the Xmon is described by the nonlinear Hamiltonian:

$$\hat{\mathcal{H}}_X = 4E_C\hat{n}^2 - \frac{1}{2}E_J\cos(\hat{\varphi}) \quad (\text{A16})$$

The number operator \hat{n} can be rewritten in terms of the bosonic annihilation operator

$$\hat{c} = \sum_n \sqrt{n+1} |n\rangle \langle n+1|$$

and the zero-point-fluctuation, $n_{zpf} = (E_J/32E_C)^{1/4}$, where we distinguish \hat{c} from the harmonic oscillator's annihilation operator \hat{a} . Applying the analogue to \hat{x} and \hat{p} , we get

$$\hat{n} = in_{zpf}(\hat{c}^\dagger - \hat{c}) = i\left(\frac{E_J}{32E_C}\right)^{1/4}(\hat{c}^\dagger - \hat{c})$$

When in the same way we define

$$\hat{\varphi} = \varphi_{zpf}(\hat{c}^\dagger + \hat{c}) = \left(\frac{2E_C}{E_J}\right)^{1/4}(\hat{c}^\dagger + \hat{c})$$

Since $\varphi_{zpf}^2 E_J = \sqrt{2E_J E_C} = 8n_{zpf}^2 E_C$, we can Taylor expand $\cos\hat{\varphi} = 1 - \hat{\varphi}^2/2^2 + \hat{\varphi}^4/24 + \dots$ to get:

$$\begin{aligned} \mathcal{H}_X &= -4E_J n_{zpf}^2 (\hat{c}^\dagger - \hat{c})^2 - E_J \left[1 - \frac{1}{2}\varphi_{zpf}^2 (\hat{c}^\dagger + \hat{c})^2 + \frac{1}{24}\varphi_{zpf}^4 (\hat{c}^\dagger + \hat{c})^4 - \dots \right] \Rightarrow \\ &\simeq \sqrt{8E_C E_J} \left(\hat{c}^\dagger \hat{c} + \frac{1}{2} \right) - E_J - \frac{E_C}{12} (\hat{c}^\dagger + \hat{c})^4 \end{aligned} \quad (\text{A17})$$

From this description of \mathcal{H}_X , we identify $\omega_{01} = (\sqrt{8E_C E_J} - E_J)/\hbar$, and the anharmonicity, $\omega_{12} - \omega_{01} = E_C/\hbar$. And we emphasize that

$$E_J = E_{0J} \cos \Phi_{ext}$$

i.e. that we can control the potential energy and thus ω_{01} by applying an external magnetic flux.

Nonlinearity of the Kinetic Inductance

The nonlinearity of L_{kin} presented in Eq. (3.5) arises from the nonlinear density of SC charge carriers: the Cooper pairs, i.e. $n_s = n_s(I)$. This is somewhat counter-intuitive. In normal metals $I = nqv$, where n is the charge carrier density, q the charge, and v the velocity. But SC microstrips behave differently.

Here, we follow the derivation of Ref. [147].

Classically, the inductance is defined as $L = V \cdot (\partial_t I)^{-1}$. Using parameters of unit-length ($L \rightarrow \tilde{L}$), we can write the definition in terms of E , the electrical field: $E = \tilde{L} \cdot (\partial_t I)$. The first

London equation [148] then connects the SC current density j_s to E :

$$\frac{\partial j_s}{\partial t} = \frac{n_s q^2 E}{m} \Rightarrow q n_s m \frac{\partial v}{\partial t} = q^2 n^2 E \Rightarrow \frac{\partial p_s}{\partial t} = q E \quad (\text{A18})$$

where p_s is the momentum of the SC charge carriers. Since only the electrical field is considered here, this contributes only to the *kinetic* inductance, so from Eq. (A18), we have:

$$\tilde{L}_k = \frac{1}{q} \left(\frac{\partial I}{\partial t} \right)^{-1} \frac{\partial p_s}{\partial t} = \frac{m}{q} \frac{\partial v_s}{\partial I} \quad (\text{A19})$$

But when v_s increases and charge carriers are in possession of large kinetic energies, the breaking of Cooper pairs becomes energetically favorable. As in a race, only the "toughest" Cooper pairs stay connected; for high currents, n_s is suppressed, but the remaining charge carriers move very fast. The GL theory, phenomenological as it might be, explains this behaviour quantitatively. GL theory is valid close to the critical current or temperature (I_c or T_c), but this is also where the nonlinearity is expected.

From GL, we find that the normalized wave function $f = |\Psi/\Psi_\infty|$, where Ψ_∞ is the wave function without currents or fields, can be described in terms of the normalized velocity, v_s/v_m , where v_m is the maximum achievable velocity [33, 147]:

$$f^2 = 1 - \frac{1}{3} \left(\frac{v_s}{v_m} \right)^2 \quad (\text{A20})$$

With these variables, the current is

$$I = qA|\Psi_\infty|^2 f^2 v^2 \quad (\text{A21})$$

where A is the cross section of the SC material. \tilde{L}_{kin} can now be expressed as

$$\tilde{L}_{kin} = \frac{m}{A q^2 |\Psi_\infty|^2} \left(1 - \frac{v_s^2}{v_m^2} \right)^{-1} \quad (\text{A22})$$

and by substitution of Eq. (A21), this becomes:

$$\tilde{L}_{kin} = \frac{\mu_0 \lambda^2}{A} \left(1 - \frac{v_s^2}{v_m^2} \right)^{-1} \quad (\text{A23})$$

In principle, $v_s \propto I$, and thus $v_m \propto I_c$, but the exact relation depends on the regime (e.g. small bias or the case of instant relaxation). To treat the problem as general as possible, we define the nonlinear coefficient

$$\eta = \left(\frac{v_s}{v_m} \right) / \left(\frac{I}{I_c} \right)$$

Applying the Taylor expansion $(1 - I/I_c)^{-1} \simeq 1 + x^2$, this leads to the result in Eq. (3.5), where $I_* \equiv I_c/\eta$.

B. Fabrication

All fabrication is done on high resistivity ($\rho > 10^5 \Omega \text{cm}$) Si wafers, 50.8 mm (2"), doubled-side polished in the $<100>$ -direction. In certain experiments, when very thin layers ($\lesssim 5 \text{ nm}$) were evaporated, we used single-side polished wafers to avoid confusion. Such a thin WSi layer is nearly transparent, and occasionally we make the mistake to apply resist to the wrong side.

Aluminum resonators

CLEANING Prior to evaporation of Al, the wafer is cleaned in EDC spinning hood (with H_2SO_4 and H_2O_2 in the relation 3:1, a solution known as piranha), and rinsed in water. Next, the wafer is emerged for 1 min in HF to remove native oxid. The wafer is then dry-blown with N_2 . The cleaning step is omitted for technical reasons, when deposition is done by sputtering.

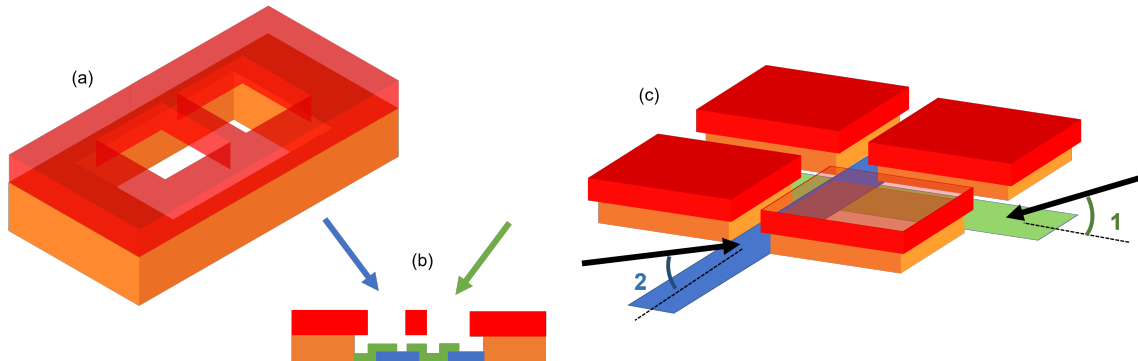


Figure B1: Lithography for junction fabrication according to the two methods described in the main text. Resist/PMMA is shown in red, LOR/cmMA is in orange. Dolan bridge (a) in 3D plot and (b) a cross section. (c) Manhattan style. Arrows indicate directions of evaporation.

DEPOSITION OF Al Option 1: AC magnetron sputtering station at a base pressure of 10^{-7} torr, which rises to 10^{-3} torr under processing with Ar^+ ions in chamber. The growth rate is 2 nm/s. Option 2: E-beam evaporation in the Angstrom Quantum Series evaporator with a rate of 5 Å/s at 10^{-7} torr.

LITHOGRAPHY AZ 1505 positive photoresist is spun at 4000 rpm to a 0.5 μm thick layer, and is soft-baked at 110°C for 90 sec. With a 405 nm laser writer we expose the resist to an energy of 24 mJ/cm² according to the predefined pattern. The wafer is subsequently developed in AZ developer, the ion-version of AZ726 MIF compatible with Al. Finally, the wafer is hard-baked at 120°C.

ETCHING Wet-etch is done in a highly selective Al etchant (that does not attack Si or WSi) at 40°C. Etching rate is 3 nm/s, and is terminated after Si appears (visually inspection of large features). The device is stripped of resist in sonicated acetone, and is sprinkled in iso-propanol before dry-blowing.

Josephson Junctions

In fabrication of the JJ, we worked with two approaches, widely used and described in the scientific literature: The Dolan Bridge and the Manhattan style.

LITHOGRAPHY Both methods for JJ productions involve the preparation of a double-layer resist mask. Whether this is done by electronic lithography or the laser writer (see above), the bottom layer is of a more sensitive resist than the top-layer. Either cMMA (coPolymer MMA 8.5) or LOR 20B (lift-off-resist). Where the top layers are exposed, the bottom layers open more widely. In the case of the Dolan bridge, the LOR under the bridge is completely removed by the developer (Fig. B1(a)). The Manhattan style junctions uses the walls of two orthogonal trenches without "hanging" features.

EVAPORATION The Dolan Bridge is based on shadow evaporation from two angles as shown in Fig. B1(b). The shadow of the bridge results in a gap in the evaporated layer. Without breaking vacuum in the evaporator, O₂ is introduced into the chamber, diffuses into the Al of the first evaporation layer, and creates a thin film (a few nm) of Al₂O₃. The second evaporation closes the gap through the oxide layer.

Manhattan style exploits the walls of the trenches (see Fig. B1(c)) and evaporates from two steep angles, orthogonal to each other. In each evaporation step, Al enters only one trench. Between the two evaporation steps, oxide is introduced as described above (for the Dolan bridge), again creating an Al-oxid-Al junction.

The WSi Amplifier

The microstrip kinetic inductance travelling wave amplifier consists of three nanometric, mutually aligned layers as illustrated in Fig. 1 of the main text.

BASE LAYER The bottom layer is the 11.6 cm long trace itself, whose cross section is $2 \mu\text{m} \times 5 \text{ nm}$ (during the research, other dimensions were tested, but here we present and discuss the results of the final version only), created by DC-magnetron sputtering a WSi target (55%/45%) directly onto the high-resistivity Si substrate. Rate: 12 sec/nm, Level 10%, ramp 10 sec. 5 min conditioning. This first layer is, like the two ones to follow, patterned by optical lithography and defined by selective wet-etch to form large pads at both ends of the trace. The parameters for lithography are as follows: In the clean room, the wafer is cleaned in acetone (few min of sonication), then isopropanol, and dried with N_2 . Then we bake 5 min on a 120°C plate. Spinning of AZ1505 is done with by 400-3-3; 4000-3-33 (these are final RPM, ramping up, and duration times). Softbake is done for 90 sec at the 110°C plate. Optical exposure is done at the 405 nm Laser Writer, with lens 4, 1% filter, d-step 2, 14.4 gain (equivalent to 66 mJ/cm^2). Development at 50 sec in AZ726 is followed by hardbake for 2 min at 120°C plate. Wet-etch is done in tungsten etchant (base hood) at room temperature at a rate of $\sim 3 \text{ nm/sec}$, and PR is removed with acetone, then rinsed in isopropanol, and finally dried with N_2 .

DIELECTRIC The dielectric material for the second layer is, as mentioned in the main text of the thesis, chosen by two properties: 1) Its low loss tangent $\tan \delta$ and 2) its permittivity ϵ_r . Materials with as low $\tan \delta$ as possible were preferred to minimize dielectric losses, and ϵ_r regulates C_l together with the thickness of the base layer. We picked evaporated amorphous Si for this purpose, as its $\tan \delta \sim 2-5 \times 10^{-4}$, while ϵ_r is close to the well-known values of ϵ_r^{Si} , which depend weakly on the morphology. Note that this lithographic step removes Si only from the WSi launchers, where metal in the next step enhances galvanic contact between wire-bonds and WSi pads.

First, LOR 5B is spun by 600-0-2 and 4000-0-30. Softbake continues for 5 min at the 200°C hot plate. We then spin AZ1505 by 600-0-2 and 4000-0-30 and bake 2 min at the 110°C plate. Laser writing with lens 4, filter 1% D-step 3, gain 27. Development is done in AZ726 for 45 sec. This time hardbake is skipped, and in general should always be avoided when preparing liftoff masks (if baked, the resist will stick too well to the substrate and will be hard to remove). Evaporation is done at a rate of 0.5 A/s using a chiller set at -5°C to ensure resist is not heated to excessively to make the liftoff difficult. Liftoff in 80°C NMP for ~ 2 hrs.

GROUND The final layer of metal, by our choice evaporated Al, constitutes the ground, and the third and last lithography step now distinguishes between the all-covering Al and the aforementioned launch pads. Using a parallel (top) ground plate covering most of the chip ensures a common global ground, as opposed to the separated ground electrodes of co-planar wave guides, cut by the trace, and it also protects the trace from scratches during subsequent handling and packaging.

The ground plate can be prepared either by wet-etch or by liftoff. The advantage of liftoff is that the patterning is done on a resist mask before Al is applied. This is notably easier than aligning the pattern to be written on the laser writer through an opaque Al layer of tens of nm.

However, liftoff of narrow Al features has turned out to be challenging, so when possible wet-etch is preferred. That is, initially an Al film is evaporated with sufficient thickness to ensure step coverage on the WSi and aSi layers below. Then spin AZ1505 with 400-3-3 and 4000-3-33. 90 sec at 110°C . Exposure, development, and etch are similar to the Aluminum resonators.

Airbridges

Airbridges are an elegant alternative to the dielectric crossovers shown in e.g. Figs. 2.1(b) and Fig. 2.2(d). Without the dielectric to support the electrically shortening metal, the intermediary material is the air (in experiments: vacuum) with the permittivity $\epsilon_r = 1$. An example is shown in Fig. B2(a), and below, the concept of fabrication is outlined. Unfortunately the yield of this structure was not adequate to be included in more advance circuits, and electrical shortening of large ground plates was instead accomplished by the dielectric crossovers or by wire-bonds (see Fig. B2(b)).

As a project in development, the spinning, exposure, and development parameters of airbridge fabrication are still subject to calibration. However, the general idea is to do what in any other process would be considered a *failed* liftoff process.

First two pads are opened in a photo-resist mask (as described above). These must be sufficiently close to each other ($\sim \mu\text{m}$), so that thanks to the round walls as illustrated in Fig. 4.4(b) we get

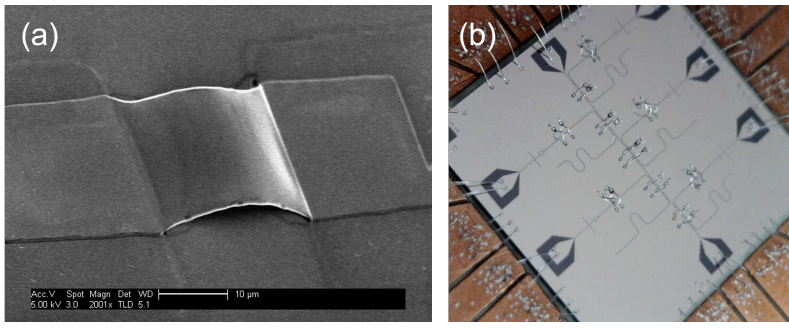


Figure B2: Shortening of groundplanes by "air bridges". (a) SEM photo of a micronic test-bridge (without base wiring) with large pads. (b) USB-camera photo of full-scale $6.2 \times 6.2 \text{ mm}^2$ chip with circuitry and qubits where ground plates, otherwise disconnected by the on-chip waveguides, have been shortened by multiple wire bonds. These bonds also serve the connectivity to the PCB at the edges of the chip.

an arc between the pads. When Al or any alternative material is evaporated, the intention is a good adhesion to the pads, and a strong "bridge" of metal spanning the arc. Resist beneath the arc is removed, and the bridge stands alone. The example of Fig. B2(a) is a test bridge without a transmission line beneath it. This structure also has very large pads to ensure the adhesion to the substrate.

For the fabrication scheme to work, the bridge must be quite thick. In our experiments, we evaporated 300 nm Al, to be compared with typically only 100 nm of the base layer. And as always, cleaning is essential, especially when conducting residues from the fabrication process can be caught in the corners of the bridge (close to the pads).

C. Theory of Coupled Microstrip Waveguides

Crystal model for integrated microwave optics

This section is based on theoretical work done in the fruitful cooperation we had with the Ankerhold group at the University of Ulm. Many of the derivations and figures were prepared by this group's students. I especially thank Björn Kubala and Ciprian Padurariu.

Here, we present a description for the linear behavior of the two coupled travelling waveguides (2CTW structure), extendable to multi-trace or full two-dimensional devices. Voltage and current travelling along the various segments, see Fig. C1(a), can be described as

$$V_\alpha^l(x_\alpha) = t_\alpha^l e^{ik_\alpha x_\alpha} + r_\alpha^l e^{-ik_\alpha x_\alpha} \quad \text{where } \alpha = p, s, c; \quad l = 1, 2, \dots, N \quad (\text{C1})$$

$$Z_\alpha I_\alpha^l(x_\alpha) = t_\alpha^l e^{ik_\alpha x_\alpha} - r_\alpha^l e^{-ik_\alpha x_\alpha} \quad \text{with } k_\alpha = 2\pi f \sqrt{L_\alpha C_\alpha} \quad \text{and} \quad Z_\alpha = \sqrt{L_\alpha / C_\alpha} \quad (\text{C2})$$

The different segments are distinguished by an index l numbering the unit cells and $\alpha = p, s, c$ for primary, secondary and coupler lines. A standard transmission line model yields the parameters for the wave propagation along the segments, where dissipation can also be included. For the 2CTW, we can assume $Z_p = Z_s =: Z_0$, $k_p = k_s =: k_0$, while $x_{p,s} \in [0, L]$ and $x_c \in [0, d]$.

The Kirchoff laws for the voltages on the nodes of the network(s), $v_{p,s}^l$ are:

$$v_p^l = V_p^{l-1}(L) = t_p^{l-1} e^{ik_p L} + r_p^{l-1} e^{-ik_p L} \quad (\text{C3a})$$

$$v_p^{l-1} = V_p^{l-1}(0) = t_p^{l-1} + r_p^{l-1} \quad (\text{C3b})$$

To evaluate the Kirchhoff current equations we rewrite the currents on the nodes variables using Eq. (C3), e.g.

$$\begin{aligned} Z_0 I_p^{l-1}(L) &= t_p^{l-1} e^{ik_0 L} - r_p^{l-1} e^{-ik_0 L} \\ &= v_p^l \frac{e^{ik_0 L} + e^{-ik_0 L}}{e^{ik_0 L} - e^{-ik_0 L}} - v_p^{l-1} \frac{2}{e^{ik_0 L} - e^{-ik_0 L}} = v_p^l \frac{z_0 + \bar{z}_0}{z_0 - \bar{z}_0} - v_p^{l-1} \frac{2}{z_0 - \bar{z}_0} \end{aligned} \quad (\text{C4})$$

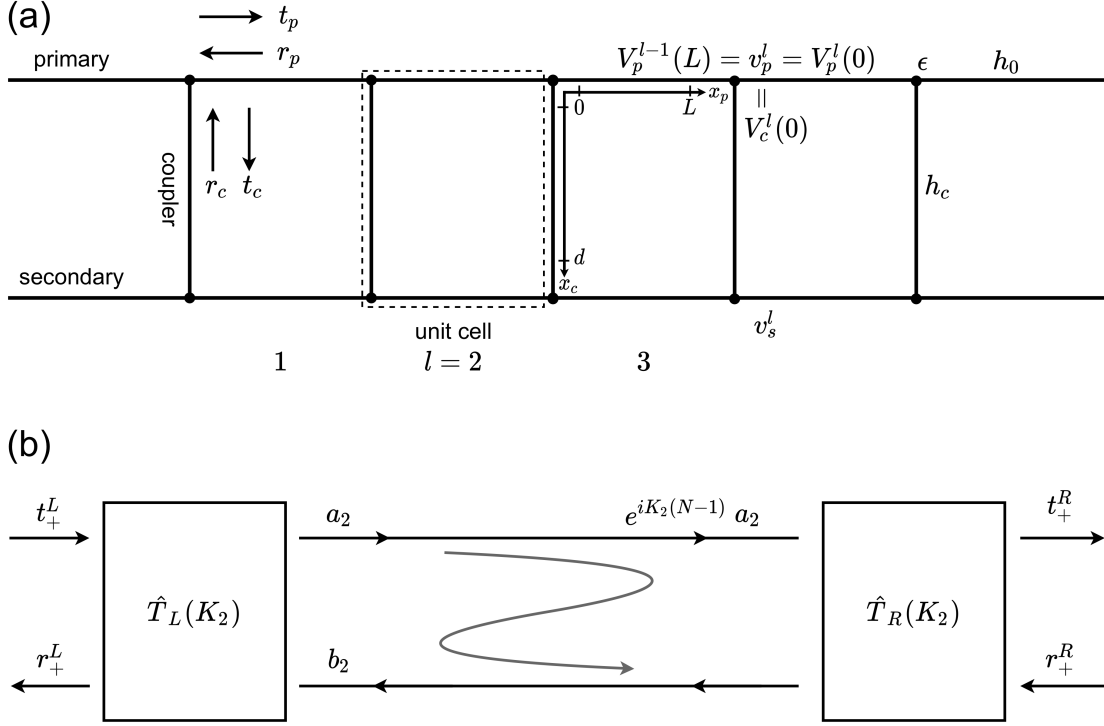


Figure C1: (a) Sketch of the 2CTW with variables as introduced in the text. Using the voltages on the nodes v_α^l as variables, Kirchhoff rules yield a tight-binding model with parameters $\epsilon, h_{0,c}$ as marked on the rightmost unit cell. (b) The Fabry-Perot resonator formed by scatterers describing in/out-coupling and propagation in an eigenmode of the infinite line.

The Kirchhoff current equations state that

$$I_p^{l-1}(L) - I_p^l(0) - I_c^l(0) = 0 \quad \text{current conservation in primary node} \quad (\text{C5a})$$

$$I_s^{l-1}(L) - I_s^l(0) + I_c^l(d) = 0 \quad \text{current conservation in secondary node} \quad (\text{C5b})$$

and when rewritten in terms of the voltage nodes (cf. Eq. (C4)) we get

$$0 = v_p^{l-1} \frac{1}{Z_0} \frac{2z_0}{1-z_0^2} + v_p^l \left(\frac{-2}{Z_0} \frac{1+z_0^2}{1-z_0^2} + \frac{-1}{Z_c} \frac{1+z_c^2}{1-z_c^2} \right) + v_p^{l+1} \frac{1}{Z_0} \frac{2z_0}{1-z_0^2} + v_s^l \frac{1}{Z_c} \frac{2z_c}{1-z_c^2} \quad (\text{C6a})$$

$$0 = v_s^{l-1} \frac{1}{Z_0} \frac{2z_0}{1-z_0^2} + v_s^l \left(\frac{-2}{Z_0} \frac{1+z_0^2}{1-z_0^2} + \frac{-1}{Z_c} \frac{1+z_c^2}{1-z_c^2} \right) + v_s^{l+1} \frac{1}{Z_0} \frac{2z_0}{1-z_0^2} + v_p^l \frac{1}{Z_c} \frac{2z_c}{1-z_c^2} \quad (\text{C6b})$$

For the sole purpose of simulations, such as those shown in Fig. 5.12, Eqs. (C3)-(C6) are enough to solve as suggested in Sec. 4.1.3, and in particular by Eq. (4.12). But Eqs. (C6) suggest a tight-binding picture as known from solid state physics with real parameters

$$\epsilon = i \left(\frac{2}{Z_0} \frac{1+z_0^2}{1-z_0^2} + \frac{1}{Z_c} \frac{1+z_c^2}{1-z_c^2} \right) \quad \text{on-site energy} \quad (\text{C7})$$

$$h_0 = -i \frac{1}{Z_0} \frac{2z_0}{1-z_0^2} \quad \text{in-line hopping} \quad (\text{C8})$$

$$h_c = -i \frac{1}{Z_c} \frac{2z_c}{1-z_c^2} \quad \text{cross-line hopping} \quad (\text{C9})$$

Eigenmodes and Band Structure

The eigenmodes of the 2CTW (assuming it is infinite) are found by the ansatz

$$\begin{pmatrix} v_p^l \\ v_s^l \end{pmatrix} = \begin{pmatrix} p \\ s \end{pmatrix} e^{iKl} \quad ; K \in \mathbb{C} \quad (\text{C10})$$

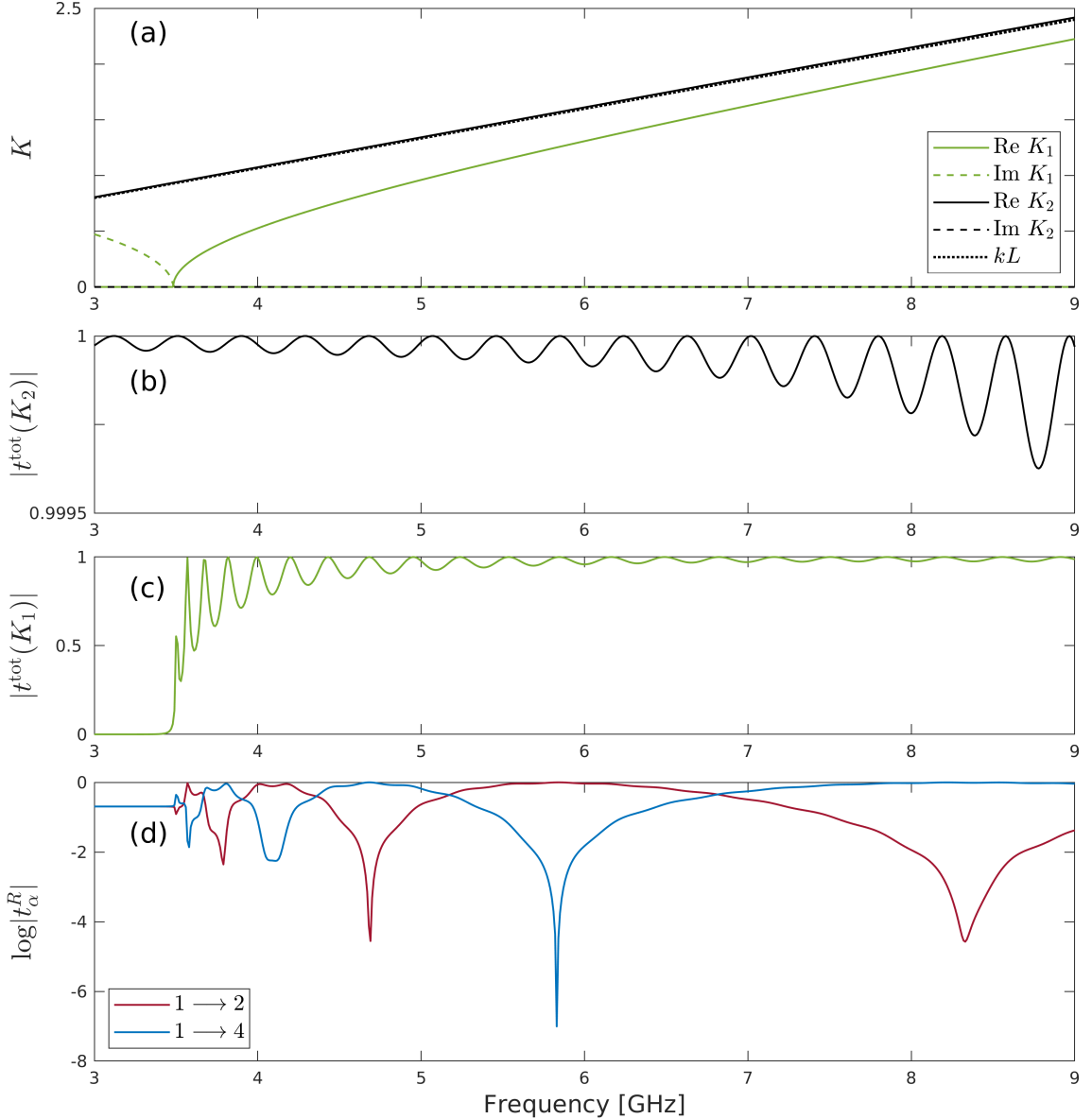


Figure C2: (a) Band structure of the double-line structure. The Bloch-wavevector $K_2 \approx kL$ of the eigenmode symmetric in primary and secondary line is nearly unaffected by the couplers, while the antisymmetric mode has a band gap where $\text{Im } K_1 > 0$. Transmission of symmetric (b) and antisymmetric (c) eigenmode through the Fabry-Perot structure, cf. Eqs. (C18) and (C19). (d) Total transmission for direct ($1 \rightarrow 2$) and cross-transmission ($1 \rightarrow 4$) resulting from constructive and destructive interference of the (anti)symmetric transmissions, see Eq. (C20).

as eigensolutions of

$$\begin{pmatrix} \epsilon + 2h_0 \cos K & h_c \\ h_c & \epsilon + 2h_0 \cos K \end{pmatrix} \begin{pmatrix} p \\ s \end{pmatrix} = 0 \quad \Rightarrow \cos K_{1/2} = -\frac{\epsilon}{2h_0} \pm \sqrt{\frac{h_c^2}{4h_0^2}} \quad (\text{C11})$$

where eigenvectors are symmetric and anti-symmetric modes in the primary and secondary lines' voltages.

Figure C2(a) shows the real and imaginary parts of the eigenvalues $K_{1,2}$ vs. frequency with range and parameters as in Fig. 5.12(a). It corresponds to a dispersion relation $\omega(K)$ for a Bloch-wave. In Fig. C2 we observed a band gap for the asymmetric solution below 3.8 GHz, where the wave solution includes a term with $\text{Im } K_1 > 0$. The symmetric solution with equal voltages at both ends of each coupler is barely affected by the couplers and $K_2 \approx kL$.

In- and Out-coupling to Eigenmodes

The symmetry of the 2CWT with respect to exchanging primary and secondary line is reflected in the symmetric and antisymmetric eigenmodes we found above. If the lines are fed by a symmetric combinations of incoming waves, these will couple to the symmetric eigenmode and result in symmetric outgoing waves. In this modus operandi, the 2CWT decouples into two independent single-channel problems.

We start by solving Eq. (C3) for the left and right-going amplitudes of the unit cell indexed ($l - 1$):

$$t_{\alpha}^{l-1} = \frac{1}{1 - z_0^2} (v_{\alpha}^{l-1} - z_0 v_{\alpha}^l) \quad (\text{C12a})$$

$$r_{\alpha}^{l-1} = \frac{1}{1 - z_0^2} (-z_0^2 v_{\alpha}^{l-1} + z_0 v_{\alpha}^l) \quad , \text{ where } \alpha = p, s \quad (\text{C12b})$$

where the input and output of a line with N nodes is

$$t_{\alpha}^L = t_{\alpha}^0, \quad r_{\alpha}^L = r_{\alpha}^0, \quad t_{\alpha}^R = z_0 t_{\alpha}^N, \quad r_{\alpha}^R = \bar{z}_0 r_{\alpha}^N \quad (\text{C13})$$

With the ansatz for the general solution

$$\begin{pmatrix} v_p^l \\ v_s^l \end{pmatrix} = a_1 e^{iK_1 l} \begin{pmatrix} 1 \\ -1 \end{pmatrix} + b_1 e^{-iK_1 l} \begin{pmatrix} 1 \\ -1 \end{pmatrix} + a_2 e^{iK_2 l} \begin{pmatrix} 1 \\ 1 \end{pmatrix} + b_2 e^{-iK_2 l} \begin{pmatrix} 1 \\ 1 \end{pmatrix} \quad (\text{C14})$$

this results in

$$t_{\alpha}^l (1 - z_0^2) = \quad (\text{C15a})$$

$$\pm a_1 e^{iK_1 l} (1 - z_0 e^{iK_1}) \pm b_1 e^{-iK_1 l} (1 - z_0 e^{-iK_1}) + a_2 e^{iK_2 l} (1 - z_0 e^{iK_2}) + b_2 e^{-iK_2 l} (1 - z_0 e^{-iK_2})$$

$$r_{\alpha}^l \frac{1 - z_0^2}{z_0} = \quad (\text{C15b})$$

$$\pm a_1 e^{iK_1 l} (e^{iK_1} - z_0) \pm b_1 e^{-iK_1 l} (e^{-iK_1} - z_0) + a_2 e^{iK_2 l} (e^{iK_2} - z_0) + b_2 e^{-iK_2 l} (e^{-iK_2} - z_0).$$

We now defined symmetric and antisymmetric combinations:

$$t_{+}^l = \frac{t_p^l + t_s^l}{2} = \frac{1}{1 - z_0^2} [a_2 e^{iK_2 l} (1 - z_0 e^{iK_2}) + b_2 e^{-iK_2 l} (1 - z_0 e^{-iK_2})] \quad (\text{C16a})$$

$$t_{-}^l = \frac{t_p^l - t_s^l}{2} = \frac{1}{1 - z_0^2} [a_1 e^{iK_1 l} (1 - z_0 e^{iK_1}) + b_1 e^{-iK_1 l} (1 - z_0 e^{-iK_1})] \quad (\text{C16b})$$

and equivalent expressions for r_{\pm}^l , so that we indeed arrive at two decoupled single-channel scattering problems.

We can solve e.g. the symmetric problem by eliminating a_2 and b_2 from the four equations. This is done by taking Eq. (C16a) and the corresponding equation for r_{+}^l at $l = 0, N$. Using Eq. (C13) we define the total scattering matrices:

$$\begin{pmatrix} r_{+}^L \\ r_{\pm}^R \end{pmatrix} = \hat{S}^{\text{tot}}(K_{2,1}) \cdot \begin{pmatrix} t_{+}^L \\ r_{\pm}^R \end{pmatrix}. \quad (\text{C17})$$

In this way we find, e.g. the total voltage amplitude

$$t^{\text{tot}}(K) = \frac{(1 - z_0^2) \sin K}{\bar{z}_0 \sin [K(N + 1)] - 2 \sin [KN] + z_0 \sin [K(N - 1)]}, \quad (\text{C18})$$

which is displayed in Figs. C2(b),(c) for the symmetric and antisymmetric single-channel problem.

Fabry-Perot picture

It is instructive to view the single-channel problem as a Fabry-Perot type scattering problem, where in- and out-coupling are actually effective left and right scattering barriers of a resonator. Transfer

matrices are then derived from Eq. (C16) and the corresponding equation for r_{\pm}^l . And Eq. (C18) is recovered as the transmission after multiple reflections

$$t^{\text{tot}}(K) = \tilde{t}_L e^{iK(N-1)} \left(1 + \tilde{r}_R e^{i2K(N-1)} \tilde{r}'_L + \dots \right) \tilde{t}_R = \frac{\tilde{t}_L e^{iK(N-1)} \tilde{t}_R}{1 - \tilde{r}_R e^{i2K(N-1)} \tilde{r}'_L}, \quad (\text{C19})$$

where $\tilde{t}_{L,R}$, $\tilde{r}_{L,R}$, $\tilde{r}'_{L,R}$ are entries of the scattering matrices corresponding to $\hat{T}_{L,R}(K_{1,2})$.

This representation explains the features observed in the total transmissions of the symmetric and antisymmetric single-channel problem shown in Figs. C2(b),(c). In the symmetric case, where the eigenmode wavevector $K_2/L \approx k$ (cf. Fig. C2). In- and out-coupling occur with limited reflections, so that the total transmission $t^{\text{tot}}(K_2) \approx 1$ with tiny Fabry-Perot oscillations is determined by the $e^{i2K_2(N-1)}$ phase factor in the denominator. In the antisymmetric case, below the bandgap (cf. Fig. C2(a)) the total transmission is completely suppressed. Above the bandgap large reflection at the in- and out-coupling barriers lead to anti-resonances, which become reduced as K_1 grows to approach kL . The frequency of oscillations is related to the slope of the $\text{Re } K_1(\omega)$ curve in Fig. C2(a).

Transmission in the 2CTW

From the results above for the total transmission for symmetric and antisymmetric input, we can reconstruct the general scattering matrix. For the case of a single input into the primary line (and all other inputs set to zero) we have,

$$t_{p,s}^R = \frac{t^{\text{tot}}(K_2) \pm t^{\text{tot}}(K_1)}{2} t_p^L. \quad (\text{C20})$$

The results shown in Fig. C2(d) agree with the numerical simulations, which we used for the comparisons to the experimental data (Fig. 5.12)(a). In the bandgap of the antisymmetric solution, where $\text{Im } K_1 > 0$, appreciable transmission only occurs through the symmetric eigenmode with $|t^{\text{tot}}(K_2)| \approx 1$, and thus also $|t_{p,s}^R| \approx 1/2$. Far above the bandgap, both eigenmodes transmit nearly perfectly in a wide frequency range and interfere constructively and destructively (alternately) in the primary and secondary lines. The frequency of this interchange is determined by the difference in $K_1 - K_2$ stemming from the

$$e^{i2K_{1,2}(N-1)}$$

phase factors in the numerators of Eq. (C19). Besides the large-scale structures in Fig. C2(d), this results in coherent swapping of power between the two lines, while the excitation propagates along the structure (not shown), familiar from directed couplers' design in integrated fibre optics.

Just above the bandgap, significant interference only occurs, when the antisymmetric transmission peaks due to a Fabry-Perot resonance. These resonances are closely spaced (as can be seen in Fig. C2(c)), and the result is the rather complex transmission pattern between 3.6 and 4 GHz.

Similar considerations can be employed for 7PTW setups, but beyond the band structure and some symmetry considerations on the eigenmode structure, an intuitive understanding becomes harder with more traces.

D. Hong-Ou-Mandel & The Birthday Paradox

In Sec. 5.1.5 we discussed the bosonic birthday paradox, based on the Hong-Ou-Mandel effect and the birthday problem from probability theory. Here, we explicitly derive the first, and elaborate on the second.

The Hong-Ou-Mandel Effect

Fig. 5.5(a) shows how two photons enter a beam splitter in ports a and b . A two-mode beam splitter is described by the transformation operator:

$$\hat{M} = \frac{1}{\sqrt{2}} \begin{pmatrix} 1 & 1 \\ 1 & -1 \end{pmatrix} \quad (\text{D1})$$

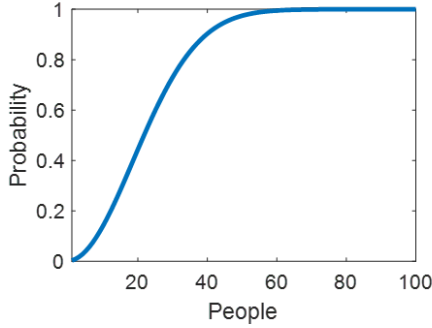


Figure D1: The paradox of the birthday problem is that even in a small group of 23 individuals, there is a 50% probability of finding at least one couple sharing the same birthday. In a group of 70, the probability is already 99.9%.

in the basis of the two modes. If a photon enters in a and is reflected, it exits in c , otherwise in d . If it enters in b and is reflected, it exits in d , otherwise in c .

Injecting a photon into port a is equivalent to applying the creation operator \hat{a}^\dagger on the empty input mode $|0, 0\rangle_{a,b}$. The creation operators \hat{b}^\dagger , \hat{c}^\dagger , and \hat{d}^\dagger should be self-explanatory. From Eq. (D1) we understand that if the beam splitter is equal (50% reflection, 50% transmission), the operation can be summarized as

$$\hat{a}^\dagger \rightarrow \frac{1}{\sqrt{2}}(\hat{c}^\dagger + \hat{d}^\dagger) \quad (\text{D2})$$

for port a . But the minus sign in Eq. (D1) makes all the difference, and for port b :

$$\hat{b}^\dagger \rightarrow \frac{1}{\sqrt{2}}(\hat{c}^\dagger - \hat{d}^\dagger) \quad (\text{D3})$$

The input mode $\hat{a}^\dagger \hat{b}^\dagger |0, 0\rangle$ therefore emerges as

$$\frac{1}{2}(\hat{c}^\dagger + \hat{d}^\dagger)(\hat{c}^\dagger - \hat{d}^\dagger)|0, 0\rangle = \frac{1}{2}(\hat{c}^{\dagger 2} - \hat{d}^{\dagger 2})|0, 0\rangle \quad (\text{D4})$$

Following the accepted conventions of ladder operators for harmonic quantum oscillators $\hat{a}^\dagger |n\rangle = \sqrt{n+1} |n+1\rangle$, so this output equals $\frac{1}{\sqrt{2}}(|2, 0\rangle + |0, 2\rangle)$.

The (Human) Birthday Paradox

Given a group of the N individuals born at random dates, the probability that all individuals are born on different dates is

$$P_0 = \frac{1}{365^N} \binom{365}{1} \cdot \binom{364}{1} \cdots \binom{365-N+1}{1} = \frac{1}{365^N} \frac{365!}{(365-N)!} \quad (\text{D5})$$

where the pre-factor of 365^{-N} is because the order is irrelevant (who is born what day). Each pair of brackets, i.e. each binomial, correspond to the "choice" of a birthday of some person (e.g. for the 3rd person, there are 363 days available, unoccupied). The probability of at least two people sharing their birthday date is naturally $P_1 = 1 - P_0$. In Fig. D1 the $P_1(N)$ is depicted.

The birthday problem is a theoretical paradox of probability theory that contradicts human intuition. A year of days seems a lot to choose between, when "distributing" the birthdays randomly. But we can help our intuition by considering the number of possible pairs in the group: In a crowd of 23, there are $23 \cdot 22 = 506$ possible pairs, candidates of sharing birthdays, making it more plausible - intuitively - to accept the high probability for a common birthday somewhere within the group.